



저작자표시-비영리-변경금지 2.0 대한민국

이용자는 아래의 조건을 따르는 경우에 한하여 자유롭게

- 이 저작물을 복제, 배포, 전송, 전시, 공연 및 방송할 수 있습니다.

다음과 같은 조건을 따라야 합니다:



저작자표시. 귀하는 원저작자를 표시하여야 합니다.



비영리. 귀하는 이 저작물을 영리 목적으로 이용할 수 없습니다.



변경금지. 귀하는 이 저작물을 개작, 변형 또는 가공할 수 없습니다.

- 귀하는, 이 저작물의 재이용이나 배포의 경우, 이 저작물에 적용된 이용허락조건을 명확하게 나타내어야 합니다.
- 저작권자로부터 별도의 허가를 받으면 이러한 조건들은 적용되지 않습니다.

저작권법에 따른 이용자의 권리는 위의 내용에 의하여 영향을 받지 않습니다.

이것은 [이용허락규약\(Legal Code\)](#)을 이해하기 쉽게 요약한 것입니다.

[Disclaimer](#)

**A THESIS  
FOR THE DEGREE OF DOCTOR OF PHILOSOPHY**

**Deep Neural Networks for Estimating the Bladder  
Boundary Using Electrical Impedance Tomography**

**Konki Sravan Kumar**



**Major of Electronic Engineering  
Faculty of Applied Energy System  
GRADUATE SCHOOL  
JEJU NATIONAL UNIVERSITY  
2019. 12**

# Deep Neural Networks for estimating the bladder boundary using Electrical Impedance Tomography

Konki Sravan Kumar

(Supervised by Professor Kyung Youn Kim)

A thesis submitted in partial fulfillment of the requirement for the  
degree of Doctor of Philosophy

2019. 12

The thesis has been examined and approved.

*Woo Young Kim*



Thesis director, Woo Young Kim, Professor, Department of Electronic Engineering,  
Jeju National University

*In Soo Lee*

In Soo Lee, Professor, School of Electronics Engineering,  
Kyungpook National University

*Min Jae Kang*



Min Jae Kang, Professor, Department of Electronic Engineering,  
Jeju National University

*Seokjun Ko*



Seokjun Ko, Professor, Department of Electronic Engineering,  
Jeju National University

*Kyung Youn Kim*



Kyung Youn Kim, Professor, Department of Electronic Engineering,  
Jeju National University

2019.12

Date

Major of Electronic Engineering, Faculty of Applied Energy System  
GRADUATE SCHOOL  
JEJU NATIONAL UNIVERSITY  
Republic of Korea



## **Dedication**

I dedicated this thesis to my parents, Konki Sanyasi Rao  
and Lakshmi for their endless love & support.

## Acknowledgements

The work with this dissertation has been extensive and trying, but in the first place exciting, instructive, and fun. This thesis is the result of three years and six months of my work. It would not have been possible to write this doctoral thesis without the help and support of the kind people around me. It is a pleasant aspect that I have now the opportunity to express my gratitude for all of them.

Foremost, I would like to express my gratitude to my supervisor Kyung Youn Kim for continuous support for my PhD research, for his patience and motivation. His guidance helped me in all the time of my research and writing thesis. I owe him lot of gratitude for having me shown this way of research. I have found Professor Kyung Youn Kim very kind, caring and approachable. His contribution towards my personal life, making sure that my stay in Jeju remains comfortable and memorable, has been enormous and does not require explicit acknowledgement.

This thesis would not have been possible without the help, support and patience of my mentor, Dr. Khambampati Anil Kumar, His deep physical insight and wide knowledge in the field of EIT was always of great assistance. He has taught me basics of EIT and the methodology to carry out my research. His good advice and friendship have been invaluable on both an academic and personal level, for which I am extremely grateful.

I would like to thank Dr. Durga Prasad Challa for his help, support, encouragement and suggestions to improve my career. He has been a real mentor and provided motivation to achieve something big in life. I also wish to thank Dr. Alluri Nagamalleswara rao for his kind, nonstop support and help whenever I face some difficulty in during stay in dorm. I am grateful for time spent with him as a roommate. I would also like to thank the other members of my Ph.D. committee who monitored my research work and took effort in reading and providing me with valuable comments on earlier versions of this thesis: Prof. Min Jae Kang, Prof. SeokJun Ko, Prof. In Soo Lee, and Prof. Woo Young Kim. Also, I wish to offer my humble gratitude to professors of my department, Prof. Yang Hoi Doh, Prof. Kwang Man Lee, and Prof. Sung Taek Ko for their inspiring and encouraging way to guide me to a deeper understanding of knowledge, and their invaluable comments during the course work, I thank you all.

I am fortunate enough to have chance to work with many people directly or indirectly. Dr. Suk In Kang has helped me initially when I joined the lab. You Jung Han has been so kind and helped me in lab. Minho Jeon helped me study and perform the experiments. Sunam Kumar Sharma have been very helpful and supported me in writing thesis. I had a good time with him as a roommate. I would also like to thank Ariungerel Jargal for her help and support in research.

Staying away from home is always challenging and tough. However, I am glad to have friends who always made be believe they are there when it matters and has been part of my happiness and hard ships. I am deeply thankful to I. Prasanthi for her friendship, supporting me in the good as well as the troubling times in my life. I also wish to thank Vivek, Vineet, Sachin, Apuroopa and Latha for giving me so many memories to cherish during my stay in Jeju. I am also grateful for the department of Electronic Engineering at Jeju University for providing me an excellent work environment during my study and I also thank Kyung Pil and Areum for their cheerful assistance in the office work.

I would like to acknowledge the financial support of Korean Government Scholarship Program (KGSP) and National Institute for International Education (NIIED). Also, Graduate school of Jeju University has been grateful to provide academic and technical support for my doctoral studies. I thank Brain Korea 21+ which provided the funds for presenting the research work held in Korea and abroad.

Finally, I will never find words enough to express the gratitude that I owe to my parents, sister, brothers, uncles and others family members. Their tender love and affection has always been the cementing force for building the blocks of my academic career. The all round support rendered by them provided the much needed stimulant to sail through the phases of stress and strain. Also thank to school and college friends.

I would like to thank all those whom I have not mentioned above but helped me in numerous ways to my success.

## Abbreviations and notations

AC	Alternating current
AI	Artificial intelligence
ANN	Artificial neural network
AP	Anterior–posterior
BEM	Boundary element method
CEM	Complete electrode model
DL	Deep Learning
DNN	Deep neural network
EIT	Electrical Impedance Tomography
FDM	Finite difference method
FEM	Finite element method
FVM	Finite volume method
LBP	Linear back projection
ML	Machine learning
mNR	Modified Newton-Raphson
MSE	Mean square error
RBF	Radial basis function
RELU	Rectified linear unit
RMSE	Root mean square error
UI	Urinary incontinence
$\varphi$	Activation function
$\gamma_k$	Boundary coefficients
$\partial\Omega$	Boundary of the object
$J^0$	Conduction current density
$J$	Cost function of the network
$\tilde{\mathbf{I}}$	Current matrix
$\Phi$	EIT objective function
$I_l$	Electrical currents
$\rho(x, y)$	Electrical resistivity distribution
$e_l$	Electrodes
$\hat{\rho}$	Estimated resistivity distribution,
$\omega$	Frequency
$m(t)$	Gradient of exponential weighted moving average
$u(x, y)$	Induced voltage on the electrodes
$X$	Input data of neural network
$\alpha$	Learning rate
$\mathbf{A}$	Magnetic vector potential, Stiffness matrix,
$U_l$	Measured voltage on the $l$ th electrode
$N_e$	Number of FEM elements

$N_m$	Number of independent voltage measurements
$\Omega$	Object to be imaged
$e_k$	Output error
$\xi_r$	Residual error
$J^s$	Source current
$\vartheta(t)$	Square of the gradient of exponential weighted moving average
$\phi_i$	Two-dimensional first-order basis function
$\mathbf{b}$	Voltage matrix
$\mu$	Permeability of the medium
$b$	Bias
$B$	Magnetic induction
$D$	Electric displacement
$Y$	Desired outputs of neural network
$E$	Electric field
$H$	Magnetic field
$J$	Current density
$k$	Number of iterations
$L$	Number of electrodes
$\xi_m$	Measurement error
$\hat{Y}$	Prediction output of neural network
$\theta_{t+1}$	Updating the weights using Adam optimizer
$W$	Weights of layers in network
$\varepsilon$	Permittivity of the medium
$\sigma$	Conductivity of the medium

# Table of Contents

List of Figures .....	vii
List of Tables .....	xi
1 . Introduction.....	1
1.1 Electrical impedance tomography .....	1
1.2 Bladder size estimation. ....	3
1.3 Boundary estimation in EIT .....	4
1.4 Aims and contents of the thesis .....	6
2 . Image Reconstruction in EIT .....	8
2.1 Derivation of EIT governing equation.....	8
2.2 Boundary conditions .....	10
2.3 Complete electrode model (CEM).....	11
2.4 Formulation of finite element method .....	11
2.5 Inverse problem .....	14
2.5.1 Gauss- Newton algorithm for image reconstruction in EIT .....	14
3 . Introduction to Artificial intelligence.....	17
3.1 Machine Learning.....	19
3.1.1 Types of machine learning .....	21
3.2 Neural networks.....	22
3.3 Training of the single layer neural network .....	24
3.4 Training of the multi-layer neural network .....	27
3.5 Radial basis function network for regression applications.....	28
4 . Deep learning .....	31
4.1 Introduction of deep learning .....	31
4.2 Vanishing gradient:.....	32
4.2.1 Rectified linear unit.....	32
4.3 Overfitting .....	33
4.4 Computational load.....	33
4.5 Learning algorithm .....	33
4.5.1 Training of the deep neural network .....	33
4.5.2 Adam optimization algorithm to minimize the cost function in the deep neural network.....	36
4.5.3 Process of the forward propagation in the deep neural network.....	37

4.5.4 Backpropagation algorithm for deep neural network.....	38
5 . Estimating human urinary bladder boundary using a deep learning algorithm.....	39
5.1 Boundary representation of the human urinary bladder.....	40
5.2 Deep neural network architecture to estimate human bladder size, shape, and location.....	42
5.2.1 Designing and training the of the DNN model .....	42
5.2.2 Evaluating the DNN model .....	43
5.3 Results and discussions:.....	44
5.3.1 Numerical studies results.....	44
5.3.2 Experimental studies with Pelvic shaped phantom.....	62
5.4 Discussion .....	83
6 . Conclusions.....	84
Summary.....	86
References .....	87

## List of Figures

Figure 1.1. Schematic diagram of EIT imaging system.....	2
Figure 2.1. Pelvic shaped FEM mesh (a) Structured mesh (b) unstructured mesh.....	12
Figure 3.1. Definitions of Artificial intelligence .....	17
Figure 3.2. Illustration of the interrelation between Artificial Intelligence, Machine Learning, Neural Network, and Deep Learning. ....	19
Figure 3.3. Workflow diagram, which explains the machine learning process.....	20
Figure 3.4. Structure of the artificial neuron. ....	23
Figure 3.5. Structure of the neural network.....	24
Figure 3.6. Structure layer neural network.....	25
Figure 3.7. Training process of the single layer neural network. ....	26
Figure 3.8. Illustration of the training process for the multi-layer neural networks using back propagation algorithm. ....	27
Figure 3.9. Architecture of radial basis function network.....	29
Figure 4.1. Mechanism of deep learning.....	31
Figure 4.2. Illustration of the vanishing gradient problem in the deep neural network model. ....	32
Figure 4.3. Rectified linear unit function. ....	33
Figure 4.4. Illustration of the deep neural network structure. ....	34
Figure 5.1. A schematic diagram of urinary bladder and neighboring tissue boundaries inside the pelvic region. ....	41
Figure 5.2. Training scheme of deep neural network.....	43
Figure 5.3. Schematic view of evaluation of the deep neural network for bladder boundary estimation. ....	44
Figure 5.4. Reconstructed image for a full size bladder in pelvic domain without noise. Asterisk marked line represents pelvic domain boundary, and the red line is true bladder boundary, the dashed line is initial guess of mNR, Magenta line is with mNR method, blue line is with RBF method, and cyan line is using DNN method.....	46
Figure 5.5. Reconstructed image for a medium size bladder in pelvic domain without noise.....	47
Figure 5.6. Reconstructed image for a small size bladder in pelvic domain without noise. Asterisk marked line represents pelvic domain boundary, and the red line is true bladder boundary, dashed line is initial guess of mNR, Magenta line is with mNR method, blue line is with RBF method, and cyan line is using DNN method.....	48

Figure 5.7. Reconstructed image for a full size bladder in pelvic domain bladder case with 2% relative noise. Asterisk marked line represents pelvic domain boundary, and the red line is true bladder boundary, the dashed line is initial guess of mNR, Magenta line is with mNR method, blue line is with RBF method, and cyan line is using DNN method.....50

Figure 5.8. Reconstructed image for a medium size bladder in pelvic domain bladder case with 2% relative noise. Asterisk marked line represents pelvic domain boundary, and the red line is true bladder boundary, the dashed line is initial guess of mNR, Magenta line is with mNR method, blue line is with RBF method, and cyan line is using DNN method.....51

Figure 5.9. Reconstructed image for a small size bladder in pelvic domain bladder case with 2% relative noise. Asterisk marked line represents pelvic domain boundary, and the red line is true bladder boundary, the dashed line is initial guess of mNR, Magenta line is with mNR method, blue line is with RBF method, and cyan line is using DNN method.....52

Figure 5.10. Reconstructed image for full size bladder with neighboring tissue case. Asterisk marked line represents pelvic domain boundary, and the red line is true bladder boundary and neighboring tissues, the dashed line is initial guess of mNR, Magenta line is with mNR method, blue line is with RBF method, and cyan line is using DNN method. ....55

Figure 5.11. Reconstructed image for medium size bladder with neighboring tissue. Asterisk marked line represents pelvic domain boundary, and the red line is true bladder boundary and neighboring tissues, the dashed line is initial guess of mNR, Magenta line is with mNR method, blue line is with RBF method, and cyan line is using DNN method. ....56

Figure 5.12. Reconstructed image for small size bladder with neighboring tissue. Asterisk marked line represents pelvic domain boundary, and the red line is true bladder boundary and neighboring tissues, the dashed line is initial guess of mNR, Magenta line is with mNR method, blue line is with RBF method, and cyan line is using DNN method.....57

Figure 5.13. Reconstructed image for full size bladder with neighboring tissue of 2% noise case. Asterisk marked line represents pelvic domain boundary, and the red line is true bladder boundary and adjacent tissues, the dashed line is initial guess of mNR, Magenta line is with mNR method, blue line is with RBF method, and cyan line is using DNN method. ....59

Figure 5.14. Reconstructed image for medium size bladder with neighboring tissue of 2% noise case. Asterisk marked line represents pelvic domain boundary, and the red line is true bladder boundary and neighboring tissues, the dashed line is initial guess of mNR, Magenta line is with mNR method, blue line is with RBF method, and cyan is using DNN method. ....60

Figure 5.15. Reconstructed image for small size bladder with neighboring tissue of 2% noise case. Asterisk marked line represents pelvic domain boundary, and the red line is true bladder boundary and neighboring tissues, the dashed line is initial guess of mNR, Magenta line is with mNR method, blue line is with RBF method, and cyan line is using DNN method. ....61

Figure 5.16. EIT experimental system used for visualization of bladder boundary (a) experimental setup (b) pelvic shaped phantom used for experiments. ....63

Figure 5.17. EIT experimental system of pelvic domain with full size bladder case. ....	64
Figure 5.18. EIT experimental system of pelvic domain with medium size bladder case. ....	65
Figure 5.19. EIT experimental system of pelvic domain with small size bladder case. ....	65
Figure 5.20. Bladder boundary estimation results for a full size bladder experimental case. Asterisk marked line represents pelvic domain boundary, the red line is true bladder boundary and neighboring tissues, dashed line is initial guess of mNR, Magenta line is with mNR method, blue line is with RBF method, and cyan line is using DNN method. ....	66
Figure 5.21. Bladder boundary estimation results for medium size bladder experimental case. Asterisk marked line represents pelvic domain boundary, the red line is true bladder boundary and neighboring tissues, the dashed line is initial guess of mNR, Magenta line is with mNR method, blue line is with RBF method, and cyan line is using DNN method. ....	67
Figure 5.22. Bladder boundary estimation results for small size bladder experimental case. Asterisk marked line represents pelvic domain boundary, the red line is true bladder boundary and neighboring tissues, the dashed line is initial guess of mNR, Magenta line is with mNR method, blue line is with RBF method, and cyan line is using DNN method. ....	68
Figure 5.23. Comparison of the simulated and experimental voltage measurements for full size bladder inside the pelvic domain (case 1). ....	70
Figure 5.24. Comparison of the simulated and experimental voltage measurements for medium size bladder inside the pelvic domain (case 2). ....	71
Figure 5.25. Comparison of the simulated and experimental voltage measurements for small size bladder inside the pelvic domain (case 3). ....	72
Figure 5.26. EIT experimental system of pelvic domain with full size bladder (surrounded by three neighboring tissue shaped targets) case. ....	74
Figure 5.27. EIT experimental system of pelvic domain with medium size bladder (surrounded by three neighboring tissue shaped targets) case. ....	75
Figure 5.28. EIT experimental system of pelvic domain with small size bladder (surrounded by three neighboring tissue shaped targets) case. ....	76
Figure 5.29. Bladder boundary estimation results for full size bladder (surrounded by three neighboring tissue shaped targets) experimental case. Asterisk marked line represents pelvic domain boundary, the red line is true bladder boundary and neighboring tissues, the dashed line is initial guess of mNR, Magenta line is with mNR method, blue line is with RBF method, and cyan line is using DNN method. ....	77
Figure 5.30. Bladder boundary estimation results for medium size bladder (surrounded by three neighboring tissue shaped targets) experimental case. Asterisk marked line represents pelvic domain boundary, the red line is true bladder boundary and neighboring tissues, the dashed line is initial guess of mNR, Magenta line is with mNR method, blue line is with RBF method, and cyan line is using DNN method. ....	78

Figure 5.31. Bladder boundary estimation results for small size bladder (surrounded by three neighboring tissue shaped targets) experimental case. Asterisk marked line represents pelvic domain boundary, and the red line is true bladder boundary and neighboring tissues, the dashed line is initial guess of mNR, Magenta line is with mNR method, blue line is with RBF method, and cyan is using DNN method.....79

Figure 5.32. Comparison of the simulated and experimental voltage measurements for full size bladder (case 1).....80

Figure 5.33. Comparison of the simulated and experimental voltage measurements for medium size bladder (case 2).....81

Figure 5.34. Comparison of the simulated and experimental voltage measurements for small size bladder (case 3).....82

## List of Tables

Table 5.1. RMSE for estimated bladder boundary coefficients for three simulation cases without noise. ....	49
Table 5.2. True and estimated area of bladder boundary for three simulation test cases. ....	49
Table 5.3. RMSE for estimated bladder boundary coefficients for three simulation cases with 2% relative noise. ....	53
Table 5.4. True and estimated area of bladder boundary for three simulation test cases with 2% relative noise. ....	53
Table 5.5. RMSE for estimated bladder boundary coefficients for three simulation test cases ....	58
Table 5.6. True and estimated area of bladder boundary for three simulation test cases ....	58
Table 5.7. RMSE for estimated bladder boundary coefficients for three simulation test cases with 2% relative noise. ....	61
Table 5.8. True and estimated area of bladder boundary for three simulation test cases with 2% relative noise. ....	62
Table 5.9. RMSE for estimated bladder boundary coefficients of three experimental cases using mNR, RBF and DNN. ....	69
Table 5.10. True and estimated area of bladder boundary for three experimental cases using mNR, RBF and DNN. ....	69
Table 5.11. RMSE of voltage measurements for three experimental cases ....	72
Table 5.12. RMSE for estimated bladder boundary coefficients of three experimental cases using mNR, RBF and DNN. ....	82
Table 5.13. True and estimated area of bladder boundary for three experimental cases using mNR, RBF and DNN. ....	83
Table 5.14. RMSE of voltage measurements for three experimental cases. ....	83

# 1 . Introduction

## 1.1 Electrical impedance tomography

The term “tomography” derived from the Greek word, “tomos” means slice and “graphe” means to draw. It is an imaging technique for displaying a cross sectional view of the human body or any solid domain. Electrical Impedance Tomography (EIT) is a noninvasive imaging technology that aims to reconstruct the cross sectional image of internal conductivity distribution of electrically conducting objects such as human body or any domain. In the working principle of EIT, an array of electrodes are attached on the surface of the human body or object domain to inject an alternating current (AC) and measure the induced voltages on the electrodes, and the corresponding electrical conductivity information is computed according to ohm’s law. The working principle of EIT is illustrated in figure 1.1. EIT provides various advantages such as portable, radiation free, cheap, non-invasive, and capable of continuous monitoring.

EIT imaging has been employed in various fields. Initially, the EIT imaging technique was used in the field of geology in 100 years ago. In geophysics, EIT was applied to visualize the inner structure of geophysics objects such as nature of the rock, porosity of the soil, exploring mineral resources, geological mapping, fractures and ground water contents (Lesparre N, Adler A *et al.* 2006, Spies *et al.* 1995). For the first time, Henderson and Webster produced work on impedance imaging for human tissue in 1978. They have designed an impedance camera to visualize the electrical impedance of the human thorax (Webster *et al.* 1978). Later, EIT has been used in numerous clinical applications such as detection of breast cancer cells (Muller *et al.* 1999, Osterman *et al.* 2000), brain tumor imaging (Benabid *et al.* 1977), gastrointestinal function (Smallwood *et al.* 1992), thoracic, lung and investigation of various physiological phenomena, such as pulmonary perfusion, cardiac function and respiratory functions (Kim *et al.* 2006, Cheney *et al.* 1999, Harris 1991, Brown 1994). In the field of process industry, EIT imaging has been successfully applied to a wide range of applications, such as monitoring the multi-phase flow in a pipe, mixing in pipes (Dickin *et al.* 1996, Pinheiro *et al.* 1997) and sedimentation. Industrial process tomography has been used for estimating air bubbles in pipe flows (Plaskowski *et al.* 1995). Apart from the above applications, EIT was also applied in imaging of fabric pressure mapping (Knight *et al.* 1990).

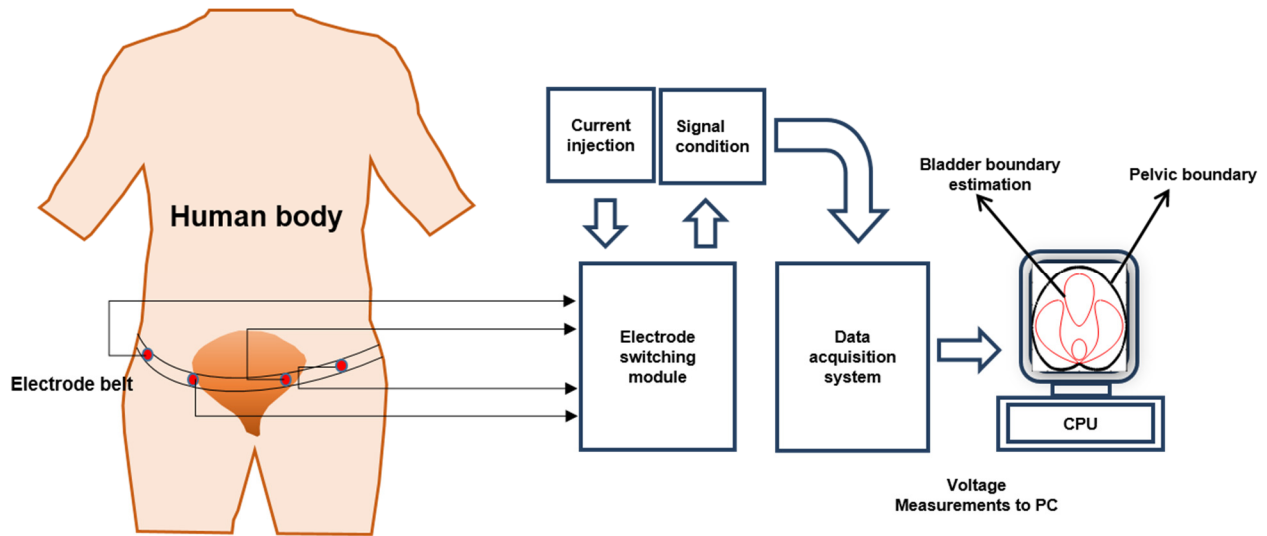


**Figure 1.1. Schematic diagram of EIT imaging system**

The EIT reconstruction problem for image reconstruction includes the forward and inverse problem. The forward problem (FP) consists of calculating boundary voltage measurements on the electrodes according to known internal conductivity distribution of domain and injected AC currents. The analytical solution of the Laplace equation for complex irregular geometries is complicated. Therefore, numerical methods are applied to solve the Laplace equation. There are several methods to address the EIT forward problem. Few of the approaches, including finite difference method (FDM) and finite volume method (FVM), require regular and straightforward grids.

Nevertheless, the disadvantage of these approaches is required regularity of the discretization. Wildly used methods which do not need any regularity of the discretization are Finite element method (FEM), Boundary element method (BEM), meshless method. When a number of mesh elements increases, the FEM solution will become a real solution of the partial differential equation (Jain *et al.* 1997). The alternative approach used for solving the Laplace equation in the interior of the volume with appropriate boundary conditions is the boundary element method (Cartwright *et al.* 2001). However, calculation for BEM requires boundary integral. There is another new approach that does not need any complex integration is meshless method (Khambampati *et al.* 2019).

On the contrary, the inverse problem in EIT is known as the reconstruction of the image. It is to estimate the internal resistivity distribution using measured voltages and applied currents on the surface of the object. The inverse problem in EIT is ill-posed problem and highly non-linear. That is, a slight variation in the voltage measurements results in a significant variation in resistivity distribution. Therefore, to overcome the effect of ill-posedness, regularization methods have been applied in EIT reconstruction. Spatial resolution in EIT is low due to ill-posedness. However, EIT has a high temporal resolution, so it offers better reconstruction performance for the sharp transition between the background and target.

### **1.2 Bladder size estimation.**

Bladder size estimation is a significant clinical parameter for patients who are suffering from urinary incontinence (UI), which is known as involuntary leakage of urine due to neurological disorders (Phelan and Franks 2001, Anderson 2004). Continuous and accurate bladder size estimation could help to provide better treatment of the patient. However, continuous manual inspection of patient bladder fullness is inconvenient and requires personal nursing (Jeong Son *et al.* 2014 and Landau 1983). Significant efforts have been made to overcome these problems over the past few years. Intermittent catheterization is a traditional method to empty the bladder by inserting the catheter, but it is an invasive method and causes the risk of urinary tract infection (Warren 1997 and Hentzen 2018). Computed tomography is one of the widely used medical imaging technology, which provides accurate bladder volume measurements, though it exposes radiation (Chun 2017). Ultrasound imaging technique offers exact measurements of bladder volume (Coombes *et al.* 1994 and Meiburger *et al.* 2018). A wearable ultrasound device has been developed for continuous monitoring of urinary bladder (Niestoruk *et al.* 2012). However, this equipment is expensive, and must be operated by professionals. Despite the advantages of conventional methods, these methods are not suitable for continuous monitoring of bladder, exposes to radiation, and devices requires professionals to operate.

Electrical impedance methods have been applied to monitor and estimate the size of the urinary bladder in the last few years. The physiological concept of this method depends on the relation between the electrical impedance measurements and bladder volume, which means variations in urinary bladder volume could cause the corresponding changes in electrical impedance (kim *et al.* 1998). The authors have performed experiments (four electrode method) by

injecting (60Hz, 1mA) AC currents through the one pair of silver-silver chloride electrodes on the surface of the pelvic region while induced voltages are measured on the other pair of electrodes. The relation between the injected currents and induced voltages reflects the electrical impedance measurements according to ohm's law (Edic *et al.* 1995). Similarly, shida *et al.* (2006) have used four electrode method and performed experiments on healthy subjects to measure the electrical impedance during urinary accumulation. The results demonstrated that sharp rise occurs in electrical impedance measurements for every urination. Schlebusch *et al.* (2013) carried out experiments on effect of arrangement of electrodes on the electrical impedance tomography for estimating the bladder volume. Authors have used global impedance and singular value decomposition methods. Another preliminary study was performed to determine the bladder volume using EIT. They have done experiments on four porcine bladders and six healthy volunteers. The results of this study described that the correlation between the average conductivity index and urinary bladder volume is linear (Rihui *et al.* 2016). Jianhuo *et al.* (2009) developed a new bladder volume monitor. The authors carried out an experimental study on urinary bladders of the eight male dogs. The bladder was filled with a saline solution, and a permanent magnet stitched onto the anterior bladder wall and a magnetic field sensor fixed onto the lower abdominal external wall in eight male dogs. Experimental results revealed that this monitoring device has the advantage of less power consumption and circuit is very simple.

Although several studies concluded that the correlation between the urinary bladder volume and electrical impedance measurements might not be valid in real time situations. Furthermore, the shape of the bladder is not clear due to poor spatial resolution of images obtained with EIT. Therefore, the boundary estimation approach in EIT may help to improve the urinary bladder shape and size estimation.

### **1.3 Boundary estimation in EIT**

As we discussed in section 1.1, estimating the internal resistivity distribution using EIT is an ill-posed problem and highly non-linear. EIT image has a lower spatial resolution due to ill-posedness and it makes difficult to reconstruct the boundaries of regions inside the object domain. If the internal resistivity distribution values of the object can be known a priori, then the inverse problem in EIT becomes estimating the boundary, size, position of the regions inside the object. The

approach to estimate region boundaries rather than internal resistivity distributions is defined as boundary estimation in EIT.

EIT boundary estimation approaches have been used in several fields of application. Furthermore, EIT was successfully applied in the process industry applications such as phase boundary estimation in two phase flow (Han and Prosperetti 1999). In the clinical applications of EIT, boundary estimation of the organ is a crucial clinical parameter to diagnosis human health. Besides, we often show interest in the boundary estimation of the organ rather than the inner conductivity distribution of the human body. Several researchers worked on organ boundary estimation problems in EIT. Vauhkonen *et al.* (1998) proposed a method to track fast human organ boundaries. An oppositional biogeography based optimization method was used to estimate boundaries of heart and lung inside the human body. The boundaries of the heart and lungs are approximated as a Fourier series coefficients and the conductivities of body organs are assumed to be known a priori (Kolehmainen *et al.* 2001, Rashid *et al.* 2010). And also authors have attempted to estimate the boundaries using modified Newton Raphson method. However, it showed severe convergence problems though a very closed initial guess was used.

Similarly, the expectation maximization algorithm was applied to estimate the dynamic boundaries of the lungs and considered the boundary of the heart to be known (Khambampati *et al.* 2010). Khambampati *et al.* (2016) proposed a boundary element method for estimating cardiac ejection fraction using electrical impedance tomography. Kim *et al.* (2010) presented a suboptimal fading extended Kalman filter for estimating electric conductivity changes inside the heart as well as lung during one cardiac cycle.

The field of artificial neural network (ANN) has become popular over the last few years in solving image reconstruction problems in EIT. Artificial neural networks algorithms have been applied to image reconstruction in EIT since they represent an effective method to approximate the complex and non-linear calculations. Several neural network methods have been used to solve the inverse problem. A neural network algorithm was employed for image reconstruction in electrical resistance tomography (Zhang *et al.* 2009). They have developed a 3-layer feed forward neural network algorithm and trained simulation model with 104 boundary voltage measurements as input, 1728 mesh elements as output. Results displayed that the NN algorithm can solve nonlinear problems and have better reconstruction performance than the standard methods. Jianwei

Li *et al.* (2012) proposed a radial basis function (RBF) neural network used for image reconstruction in ECT. The simulation results of this method are more accurate than the back-projection method. Another study was introduced based on artificial neural networks for estimating the cylindrical region boundaries in industrial flow structure (Hela et al. 2016). Results show that the estimation performance of ANN is 140 times faster than the linear back projection (LBP) algorithm.

The performance of the inverse algorithms for estimation of organ boundaries using EIT is often sub-optimal. Several factors contribute to poor performance including high sensitivity of EIT to the measurement noise, the rounding-off errors, the inherent ill-posed nature of the problem. Moreover, the performance of many of these boundary estimation techniques heavily depend on the selection of initial guess as well as the accurate computation of a Jacobian matrix and failed in estimating the complex shape boundaries. Therefore, all these methods often fail to provide significant results in clinical environments. Considering these facts, the most critical aspect of introducing the inverse algorithm is the improvement of the accuracy of region boundaries for a complex shape. A novel, the efficient inverse algorithm is therefore required to solve the above mentioned challenges.

#### **1.4 Aims and contents of the thesis**

The present thesis describes a deep neural network approach to estimate urinary bladder boundary inside the pelvic domain using EIT. The urinary bladder and neighboring tissue boundaries inside the pelvic region are approximated by the truncated Fourier series approach. Since the electrical conductivity values of background tissue, bladder, and neighboring tissues inside the pelvic domain are known a priori. Two deep neural network models are designed to the estimate bladder boundary. Firstly, a 5-layer deep neural network (DNN) model is intended to estimate the boundary of a bladder shaped target inside the pelvic domain. The model is trained with pairs of the boundary voltage measurements of pelvic area as input data and the corresponding Fourier coefficients of internal bladder boundary as output data. Whereas the second 5-layer DNN model is designed to estimate boundary of bladder shaped targets surrounded by three other neighboring tissues inside the pelvic domain. A statistical analysis of the estimated urinary bladder coefficients using DNN algorithm is performed and compared with modified Newton-Raphson and RBF-NN. The proposed DNN algorithm is simple to implement, accurate and fast estimation. Furthermore,

DNN technique does not require any initial guess and Jacobian matrix computations. However, deep neural network requires large amount data for training and testing the model.

This thesis contains five chapters. Chapter 1 gives a brief introduction of electrical impedance tomography, working principle, and its applications. It also presents the importance of urinary bladder size estimation, a literature survey of boundary estimation in EIT, and an overview of the DNN algorithm.

Chapter 2 explains image reconstruction in EIT, data collection methods, formulation of finite element method, and implementation of the inverse solver.

In chapter 3, the introduction of artificial intelligence, machine learning, and neural networks described. It also explains how to train the single and multi-layer neural network, its limitations, and the neural network for regression problems.

Chapter 4 introduces deep learning, implementation of deep neural networks, and its improvements such as vanishing gradient, overfitting, and computational load.

In chapter 5, boundary approximation of urinary bladder, estimating bladder boundary using the deep neural network is explained. Multiple numerical simulations performed using the pelvic shaped mesh. Experimental studies are carried out with pelvic phantom, the estimation performance of deep neural networks evaluated with simulation and experimental studies. Finally, reconstructed results of DNN compared to the modified newton Raphson method and radial basis function network, then analyzed.

Finally, chapter 6 presents the conclusion and future work of the thesis.

## 2 . Image Reconstruction in EIT

### 2.1 Derivation of EIT governing equation

The EIT reconstruction procedure for boundary estimation is composed of the forward and inverse problem. The forward problem is to calculate boundary voltage measurements on the electrodes according to known internal conductivity distribution of domain and injected AC currents. On the contrary, inverse problem in EIT known as the reconstruction of the image. It is to estimate the internal resistivity distribution using measured voltages and applied currents on the surface of the object. In order to reconstruct the image of urinary bladder inside pelvic domain, a small magnitude of electrical currents  $I_l$  ( $l=1,2,\dots,L$ ) is injected through the skin electrodes  $e_l$  ( $l=1,2,\dots,L$ ) placed on the surface  $\partial\Omega$  of the pelvic domain having electrical resistivity distribution  $\rho(x, y)$  in  $\Omega$ . The electrical potential  $u(x, y)$  in  $\Omega$  on the electrodes is described by Maxwell equation of electromagnetism (Isaacson *et al.* 1990, Malmivuo *et al.* 1995, Nunez *et al.* 1981). Considered that  $\mathbf{E}$  be an electric field,  $\mathbf{B}$  magnetic induction,  $\mathbf{H}$  used for a magnetic field,  $\mathbf{J}$  used for denoting the current density and  $\mathbf{D}$  denoted as the electric displacement, then the electromagnetic field in a pelvic domain  $\Omega \in \mathfrak{R}^2$  can be defined as

$$\text{From Faraday's Law} \quad \nabla \times \mathbf{E} = -\frac{\partial \mathbf{B}}{\partial t} \quad (2.1)$$

$$\text{From Coulomb's Law} \quad \nabla \times \mathbf{H} = \mathbf{J} + \frac{\partial \mathbf{D}}{\partial t}, \quad (2.2)$$

If the pelvic domain  $\Omega$  is assumed to consist of a linear and isotropic medium, then the following

$$\mathbf{D} = \varepsilon \mathbf{E} \quad (2.3)$$

$$\mathbf{J} = \sigma \mathbf{E} \quad (2.4)$$

$$\mathbf{B} = \mu \mathbf{H} \quad (2.5)$$

where  $\varepsilon$  is the permittivity,  $\mu$  is the permeability, and  $\sigma$  is conductivity of the medium. If the injected currents are assumed to be time harmonic with frequency  $\omega$ , then we get following

$$\mathbf{E} = \tilde{\mathbf{E}} e^{i\omega t} \quad (2.6)$$

$$B = \tilde{B}e^{i\omega t}. \quad (2.7)$$

From the equation (2.1) and (2.2),

$$\begin{aligned} \nabla \times E &= -\frac{\partial B}{\partial t} = -\frac{\partial(\tilde{B}e^{i\omega t})}{\partial t} \\ &= -i\omega\tilde{B}e^{i\omega t} - \frac{e^{i\omega t}\partial(\tilde{B})}{\partial t} = -i\omega\mu H - \frac{e^{i\omega t}\partial(\tilde{B})}{\partial t} \\ \nabla \times H &= J + \frac{\partial D}{\partial t} = J + \frac{\partial(\epsilon E)}{\partial t} = J + \frac{\epsilon\partial(\tilde{E}e^{i\omega t})}{\partial t} \\ &= J + i\omega\epsilon\tilde{E}e^{i\omega t} + \frac{\epsilon e^{i\omega t}\partial(\tilde{E})}{\partial t} = J + i\omega\epsilon E + \frac{\epsilon e^{i\omega t}\partial(\tilde{E})}{\partial t}. \end{aligned}$$

If the conduction current density in a conductive medium is  $J^0$  ( $J^0 = \sigma E$ ) then the total current is  $J$  ( $J = J^s + J^0$ ), and source current ( $J^s$ ). we get the following time harmonic Maxwell equations (Somersalo et al. 1992, Doerstling 1995, Ola et al. 1993)

$$\nabla \times E = -i\omega\mu H \quad (2.8)$$

$$\nabla \times H = (\sigma + i\omega\epsilon)E + J^s. \quad (2.9)$$

The electric field  $E$  can be

$$E = -\nabla u - \frac{\partial A}{\partial t}, \quad (2.10)$$

where  $A$  magnetic vector potential and  $u$  is scalar electric potential.

In EIT, source current ( $J^s$ ) is zero at frequency  $\omega$ . We assume the static conditions  $i\omega\epsilon E$  can be neglected (Vauhkonen 1997; Barber and Brown, 1984; Baker 1989) and then the electric potential can be

$$E = -\nabla u \quad (2.11)$$

$$\nabla \times H = \sigma E + J^s. \quad (2.12)$$

Then, we get

$$\nabla \cdot (\nabla \sigma u) = 0, \quad (2.13)$$

where  $u = u(x, y)$ , for  $x, y \in \Omega$ . The above equation (2.13) represents the EIT governing equation. It can be solved using the proper boundary conditions.

## 2.2 Boundary conditions

On the pelvic domain boundary  $\partial\Omega$ , the current source  $J_s$  is not zero in EIT. Then the boundary as

$$\nabla \cdot \sigma E = -\nabla \cdot J_s. \quad (2.14)$$

Integrating both sides the above equation over the volume  $v$ ,

$$\int_v \nabla \cdot \sigma E dv = -\int_v \nabla \cdot J_s dv. \quad (2.15)$$

Using the divergence theorem, we get

$$\int_S \sigma E \cdot \mathbf{n} dS = -\int_S J_s \cdot \mathbf{n} dS, \quad (2.16)$$

where  $S$  is the surface of  $v$ , and  $\mathbf{n}$  is the unit-normal vector. Since  $J_s = 0$  inside the object and  $E = 0$  outside the object, the equation (2.16) gets the form

$$-\sigma E \cdot \mathbf{n}|_{inside} = -J_s \cdot \mathbf{n}|_{outside}. \quad (2.17)$$

The Neumann-type boundary condition is obtained using the equation (2.11) and (2.17)

$$\sigma \frac{\partial u}{\partial \mathbf{n}} = -J_s \cdot \mathbf{n} \equiv j_n, \quad (2.18)$$

where  $j_n$  is the negative normal component of the injected current density ( $J_s$ ).

### 2.3 Complete electrode model (CEM)

The complete electrode model (CEM) considers both the shunting effect as well as the contact impedance between the skin electrodes and the surface of the pelvic domain. The CEM is widely used in EIT due to realistic nature and accurate. This model consists of the following boundary conditions

$$u + z_l \sigma \frac{\partial u}{\partial \mathbf{n}} = U_l, \quad (x, y) \in e_l, \quad l = 1, 2, \dots, L \quad (2.19)$$

$$\int_{e_l} \sigma \frac{\partial u}{\partial \mathbf{n}} dS = I_l, \quad (x, y) \in e_l, \quad l = 1, 2, \dots, L \quad (2.20)$$

$$\sigma \frac{\partial u}{\partial \mathbf{n}} = 0, \quad (x, y) \in \partial\Omega \setminus \bigcup_{l=1}^L e_l \quad (2.21)$$

where  $U_l$  is the measured voltage on the  $l$  th electrode,  $L$  is the number of skin electrodes,  $z_l$  is the contact impedance between the  $l$  th electrode and the surface of a pelvic domain, and  $I_l$  is the injected current into the  $l$  th electrode. In addition to the electrode model, the following Kirchhoff's laws on the measured voltages and injected currents are required to guarantee the existence and uniqueness of the solution (Somersalo *et al.* 1992).

$$\sum_{l=1}^L I_l = 0 \quad \text{And} \quad \sum_{l=1}^L U_l = 0. \quad (2.22)$$

### 2.4 Formulation of finite element method

The forward problem of EIT is the process of calculating boundary voltage measurements on the electrodes according to known internal conductivity distribution of domain and injected AC currents. The analytical solution of the Laplace equation for complex irregular geometries is typical, and therefore numerical methods are applied to solve the Laplace equation. There are several methods to address the EIT forward problem. Few of the approaches have been developed, including finite difference method (FDM) and finite volume method (FVM) require regular and straightforward grids. Nevertheless, the disadvantage of these approaches is requires the regularity of discretization. Wildly used methods that do not need any regularity of the discretization are Finite element method (FEM), Boundary element method (BEM), meshless method, etc. When

number of mesh elements increases, FEM solution will become a real solution of the partial differential equation (Jain *et al.* 1997). Another approach used for solving Laplace equation in the interior of the volume with appropriate boundary conditions is the boundary element method (Cartwright *et al.* 2001). In this thesis study, 2-D FEM is adopted to solve the forward problem of EIT.

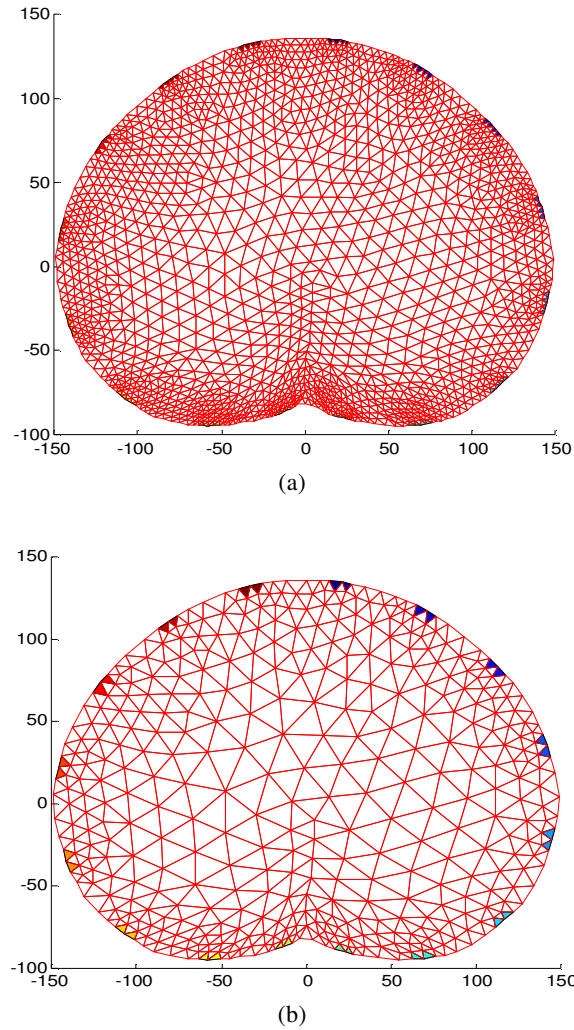


**Figure 2.1. Pelvic shaped FEM mesh (a) Structured mesh (b) unstructured mesh**

In FEM forward solver, the object (pelvic shaped domain)  $\Omega$  is discretized into small triangular elements, as shown in figure 2.1. The vertices of the triangle elements are called the nodes  $N^k$ . The darker triangular elements the skin electrodes attached to the circumference of the pelvic

region. We considered that electrical conductivity within each triangular element is uniform. The potential distribution  $u$  within the object is described as

$$u \approx u^h(x, y) = \sum_{i=1}^{N_k} \alpha_i \phi_i(x, y), \quad (2.23)$$

And the electrical voltage on skin electrodes are approximated as

$$U^h = \sum_{j=1}^{L-1} \beta_j \mathbf{n}_j, \quad (2.24)$$

where

$\phi_i$  = two-dimensional first-order basis function,

$\mathbf{n}_1 = (1, -1, 0, \dots, 0)^T$  and

$\mathbf{n}_2 = (1, 0, -1, 0, \dots, 0)^T \in \mathfrak{R}^{L \times 1}$

$\phi_i$ ,  $\mathbf{n}_1$  and  $\mathbf{n}_2$  are the bases for the measurements.  $\alpha_i$  and  $\beta_i$  are the coefficients to be determined. The finite element formulation gives the following system of linear equations

$$\mathbf{A}\mathbf{b} = \tilde{\mathbf{I}}, \quad (2.25)$$

where

$$\mathbf{A} = \begin{pmatrix} \mathbf{B} & \mathbf{C} \\ \mathbf{C}^T & \mathbf{D} \end{pmatrix} \in \mathbb{R}^{(N_k+L-1) \times (N_k+L-1)}, \quad (2.26)$$

$$\mathbf{b} = \begin{pmatrix} \boldsymbol{\alpha} \\ \boldsymbol{\beta} \end{pmatrix} \in \mathbb{R}^{N_k+L-1}, \quad (2.27)$$

$$\tilde{\mathbf{I}} = \begin{pmatrix} \mathbf{0} \\ \sum_{l=1}^L I_l \mathbf{M}(l, j) \end{pmatrix} = \begin{pmatrix} \mathbf{0} \\ \mathbf{M}^T \mathbf{I} \end{pmatrix} = \begin{pmatrix} \mathbf{0} \\ \boldsymbol{\zeta} \end{pmatrix} \in \mathbb{R}^{N_k+L-1}, \quad (2.28)$$

$$\boldsymbol{\alpha} = (\alpha_1, \alpha_2, \dots, \alpha_N)^T \in \mathfrak{R}^{N_k},$$

$$\boldsymbol{\beta} = (\beta_1, \beta_2, \dots, \beta_{L-1})^T \in \mathfrak{R}^{L-1},$$

$$\mathbf{0} \in \mathfrak{R}^{N_k}, \text{ and}$$

$$\boldsymbol{\zeta} = (I_1 - I_2, I_1 - I_3, \dots, I_1 - I_L)^T \in \mathfrak{R}^{L-1}.$$

and the stiffness matrix  $\mathbf{A}$  is of the form

$$\mathbf{B}(i, j) = \int_{\Omega} \sigma \nabla \varphi_i \cdot \nabla \varphi_j d\Omega + \sum_{\ell=1}^L \frac{1}{z_{\ell}} \int_{e_{\ell}} \varphi_i \varphi_j dS, \quad i, j = 1, 2, \dots, N_k, \quad (2.29)$$

$$\mathbf{C}(i, j) = -\frac{1}{z_1} \int_{e_1} \varphi_i dS + \frac{1}{z_{j+1}} \int_{e_{j+1}} \varphi_i dS, \quad i = 1, 2, \dots, N_k, \quad j = 1, 2, \dots, L-1 \quad (2.30)$$

$$\mathbf{D}(i, j) = \begin{cases} \frac{|e_1|}{z_1} & i \neq j \\ \frac{|e_1|}{z_1} + \frac{|e_{j+1}|}{z_{j+1}} & i = j \end{cases}, \quad i, j = 1, 2, \dots, L-1, \quad (2.31)$$

where  $|e_j|$  is the area of the electrode  $j$ . Also, in equation (2.25),  $\mathbf{0} \in \mathbb{R}^{N_n}$   $I = [I_1, I_2, \dots, I_L]^T \in \mathbb{R}^L$  and  $\boldsymbol{\zeta} = [I_1 - I_2, I_1 - I_3, \dots, I_1 - I_L]^T \in \mathbb{R}^{L-1}$  and  $I$  is a current pattern. Hence, the approximate solutions  $u^h$  and  $U^h$  for the forward problem are obtained by solving  $\mathbf{b} = \mathbf{A}^{-1} \tilde{\mathbf{I}}$ . That is, the last  $L-1$  coefficients in  $\mathbf{b}$  give the referenced voltages on the electrodes.

## 2.5 Inverse problem

Inverse problem is to estimate the internal resistivity distribution using measured voltages and applied currents on the surface of the object. The inverse problem in EIT is ill-posed and highly non-linear. That is, a slight variation in the voltage measurements results in a significant impact in resistivity distribution.

### 2.5.1 Gauss- Newton algorithm for image reconstruction in EIT

The relation between the boundary voltage  $U$  and resistivity distribution  $\rho$  of pelvic domain is nonlinear, and then the measured voltages  $\tilde{U}$  can be written as

$$\tilde{U} = U(\rho) + \xi_m, \quad (2.32)$$

where  $\xi_m$  measurement error  $\xi_m \in \mathbb{R}^{N_m}$  and  $\rho \in \mathbb{R}^{N_e}$ .  $N_m$  is the number of independent voltage data and  $N_e$  is the number of FEM elements. If the estimated resistivity distribution is  $\hat{\rho}$ , the measured voltages using the residual errors  $\xi_r \in \mathbb{R}^{N_m}$  can be written as

$$\tilde{U} = U(\hat{\rho}) + \xi_r. \quad (2.33)$$

In an inverse problem, determining the internal resistivity distribution of the pelvic domain is approximated as the least square problem. The objective function to obtain the optimal estimation of resistivity distribution  $\hat{\rho}$  is as follows

$$\begin{aligned} \Phi = \Phi(\hat{\rho}) &= \frac{1}{2} \|\xi_r\|^2 = \frac{1}{2} \xi_r^T \xi_r \\ &= \frac{1}{2} [\tilde{U} - U(\hat{\rho})]^T [\tilde{U} - U(\hat{\rho})]. \end{aligned} \quad (2.34)$$

Let be  $\hat{\rho} = \rho_c + \Delta\rho$ , where  $\rho_c$  is the estimated current resistivity distribution and  $\Delta\rho$  is a sufficiently small value. Linearizing  $U(\hat{\rho})$  at  $\rho_c$  using a first-order Taylor series expansion,

$$U(\hat{\rho}) \approx U(\rho_c) + J\Delta\rho, \quad (2.35)$$

where,  $J \equiv J(\rho_c) \equiv \frac{\partial U(\rho_c)}{\partial \rho_c} \in \mathbb{R}^{N_m \times N_e}$  is the Jacobian matrix. The measurement residual error is represented as

$$\begin{aligned} \xi_r \equiv \Delta U \equiv \tilde{U} - U(\hat{\rho}) &\approx \tilde{U} - U(\rho_c) - J\Delta\rho \\ &= \Delta U_c - J\Delta\rho, \end{aligned} \quad (2.36)$$

Let, the  $J^T J$  known as Hessian matrix is positive definite, then the Hessian matrix  $J^T J$  can be inverted to get the solution for the optimal estimate as

$$\Delta\rho = (J^T J)^{-1} J^T \Delta U_c. \quad (2.37)$$

The Gauss-Newton algorithm is derived from the  $\hat{\rho} = \rho_c + \Delta\rho$  and  $\Delta U_c \equiv \tilde{U} - U(\rho_c)$ ,

$$\hat{\rho} = \rho_c + (J^T J)^{-1} J^T (\tilde{U} - U(\rho_c)). \quad (2.38)$$

Let us use an iterative index  $i$  in equation (2.38)

$$\hat{\rho}_{i+1} = \hat{\rho}_i + (J_i^T J_i)^{-1} J_i^T (\tilde{U} - U(\hat{\rho}_i)). \quad (2.39)$$

The Hessian matrix  $(J_i^T J_i)$  is highly ill-posed. Therefore, the regularization techniques have to be applied to obtain stable inverse solution and offer a meaningful solution. The Jacobian matrix in the inverse problem can be calculated by using the standard method (Webster 1987; Vauhkonen 1997).

In this thesis, the main objective is to estimate the urinary bladder size, shape, and position. Therefore, if the internal resistivity distribution values of the pelvic can be known a priori, then the inverse problem in EIT becomes estimating the urinary bladder boundary inside the pelvic domain. Recall the equation (2.34). Then the cost function to estimate the bladder boundary coefficients  $\gamma_k$  (approximated as Fourier coefficients) inside the pelvic region can be expressed as follows

$$\Phi(\gamma_k) = \frac{1}{2} [\tilde{U} - U(\gamma_k)]^T [\tilde{U} - U(\gamma_k)]. \quad (2.40)$$

Where  $U(\gamma_k) \in \mathfrak{R}^{LK \times 1}$  are the voltages on the boundary electrodes based on given bladder boundary coefficients  $\gamma_k$ ,  $\tilde{U} \in \mathfrak{R}^{LK \times 1}$  are the measured voltages,  $k$  defines several iterations, and  $LK$  represents the number of measurements at each iteration.

### 3 . Introduction to Artificial intelligence

Artificial intelligence (AI) is the theory and development of an intelligent machine that has an independent ability to reason, listen, and think like a human. Another definition of AI is “the science and engineering of making intelligent machines” and John McCarthy coined the term AI in the Dartmouth conference (1956).

The McCarthy definition of Artificial intelligence represents a computer machine that behaves like a human. There are two types of thoughts. The first one is computer machine that acts like a human, but humans always do not behave intelligently even though humans are pretty intelligent. The second type of thought processing is AI's concern with intelligence, which is the ideal behavior and rational behavior. Again, there are two kinds of actions that human does. The first one is thinking in intelligence and the second approach is acting in intelligence. So, based on all this criterion we can see four different kinds of definition of intelligent machines. Thus, thought processing verses behaviors and performance like human verses ideal performance. The definitions of artificial intelligence are classified into four categories as shown in Figure 3.1.

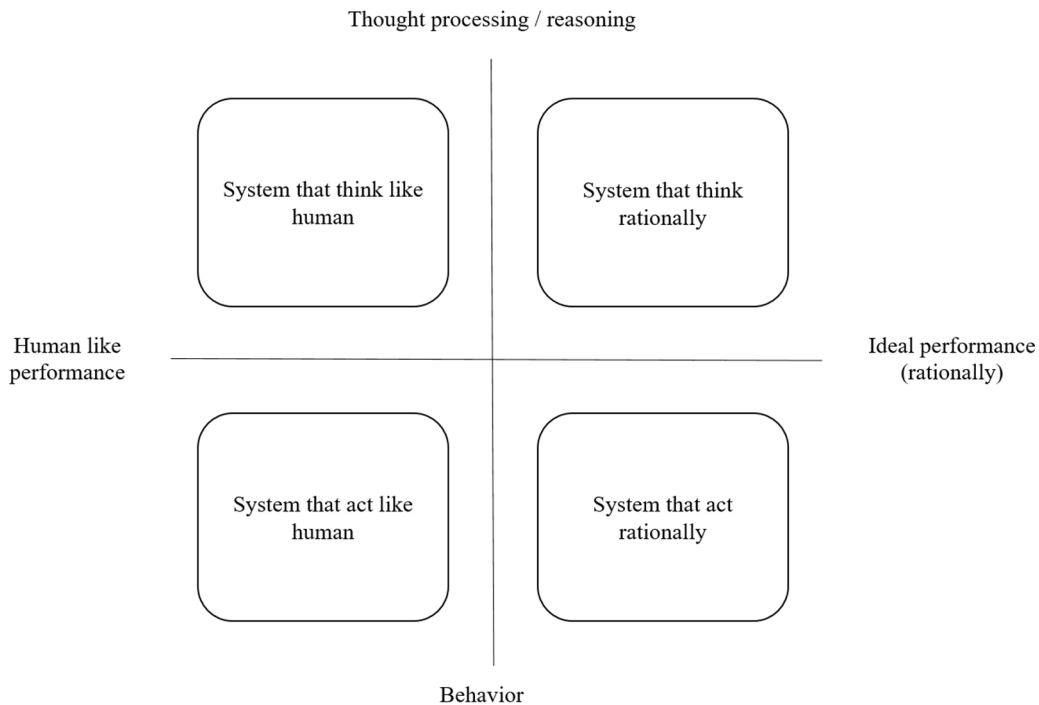
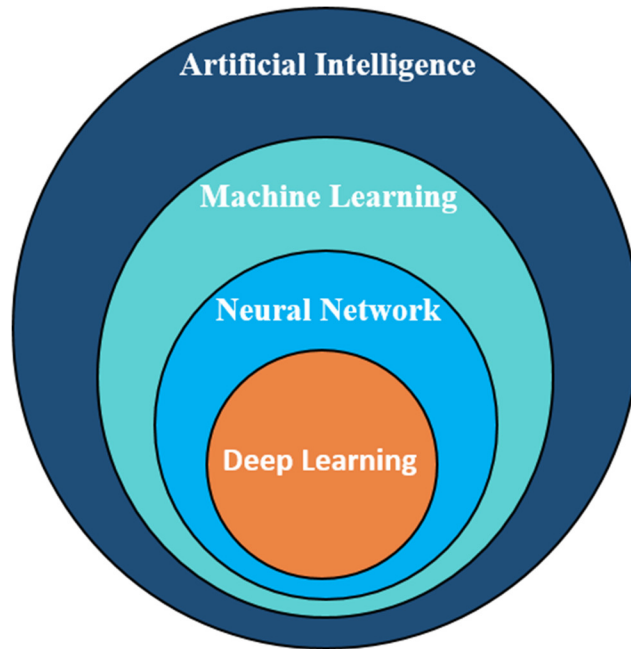


Figure 3.1. Definitions of Artificial intelligence

The definitions on the top and bottom are concerned with thought processing or reasoning and behavior. On the left and right side of definitions measure the favorable outcome based on fidelity to humans like performance and ideal performance. Therefore, there are few systems that think like a human. The main goal of this system is to design a system that feels like a human brain and a determined theory of how the human mind works. The theory should allow the definition of computational models. Second, the systems think rationally. Aristotle (384 BC- 322 BC) arranged “the right thinking” into systematic code, and rational thoughts worked based on logic. The objective of third approach is to build a system that acts like a human. For example, a turning test approach was proposed by Alan Turning in 1950 to come up with acceptable definition of artificial intelligence. It defined the behavior of intelligent systems that has ability to reach the human level performance in cognitive assignments. In the turning test, there will be a closed room that may contain either a computer or human and interrogator outside of the room. The interrogator has a text channel conversation with human being or computer. The interrogator has to identify it is talking with a human being or a computer. The capabilities required for a system in this approach are natural language process, learning, and reasoning. The final approach focuses on rational agents to achieve the best expected outcome by using previous information. Rational agents require perceptron, machine learning, natural language process, and reasoning.

Artificial intelligence is powerful because it draws from combination of disciplines such as Philosophy, Mathematics, Statistics, Economics, Neuroscience, Psychology / Neuroscience, Computer Engineering, Control Theory, and Linguistics that deal same tasks as AI. In general, the interrelation between Artificial intelligence, Machine learning (ML), Neural network (NN), and Deep Learning (DL) is given as “Machine Learning is a particular kind of Artificial Intelligence whereas Deep Learning and Neural Network are kinds of Machine Learning” as shown in figure 3.2.



**Figure 3.2. Illustration of the interrelation between Artificial Intelligence, Machine Learning, Neural Network, and Deep Learning.**

### **3.1 Machine Learning**

Machine learning is a branch of artificial intelligence, which focus on the study and design of algorithms that permit computer to develop a model from the empirical data of different examples such as images, documents, video, audio, etc. The definition of Machine learning was explained by Tom Mitchell in 1998 as follows “Machine Learning is the development of algorithms that automatically learns from experience E, improve their performance measure P at some task in T. A well-defined machine learning task is followed by  $\langle P, T, E \rangle$ . Here, the task T contains classification, regression, categorization/clustering, prediction, problem solving /planning/control. Machine learning is concerned about designing a model from the data. The process of machine learning is shown in figure 3.3, which consists of a few steps as given below.

- Data collection and preparation
- Model selection
- Model processing/ Training
- Evaluation of trained model
- Tuning hyper parameters
- Prediction

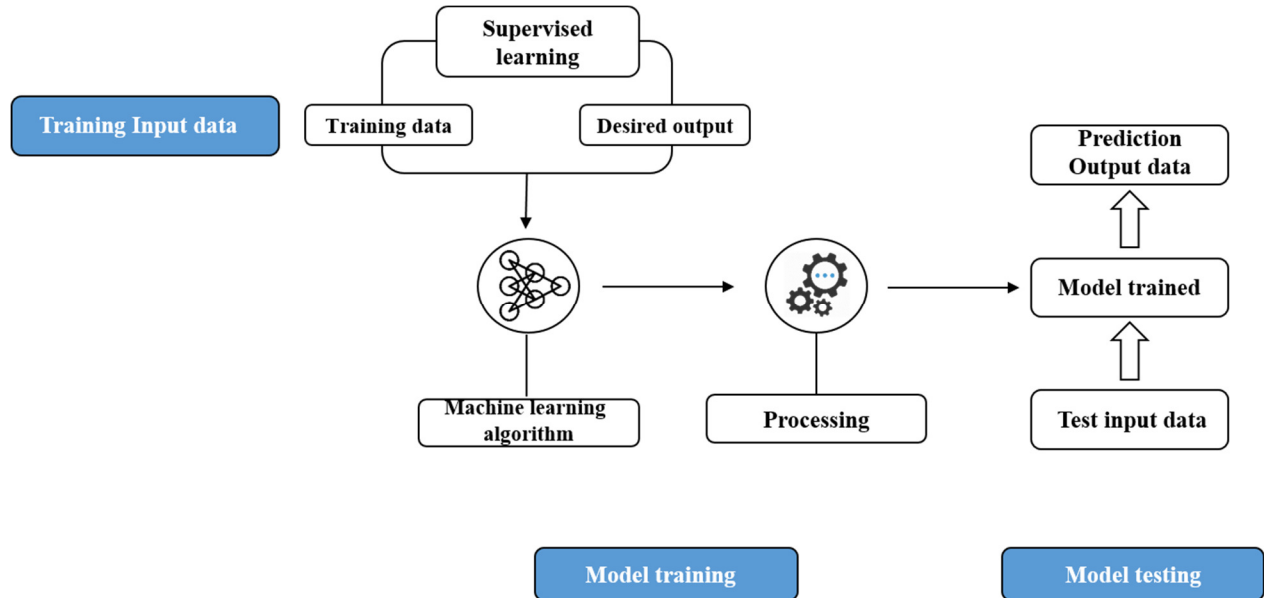


**Figure 3.3. Workflow diagram, which explains the machine learning process.**

Now, let us look deep into the steps of the machine learning process one by one. The first step is data collection and data preparation, which is a significant step among all because the quantity and quality of gathered data would determine how accurate our machine learning model can be. After collecting the data, now it is time to prepare the gathered data. We need to divide our dataset into two groups. First group, 80% of the dataset used in training the machine learning model. Whereas the second group, 20% of the dataset is used to validate our trained machine learning model performance.

The second step of the machine learning process is model selection. They are a large number of machine learning models created for text based data, image data; some are for numerical data, etc. Here the foremost step of the machine learning process is model training. In this step, we will first use group of the data to train our machine learning model and make model that has ability to predict accurately.

Fourth step is an evaluation of our trained model. It is time to check how our machine learning model performs against the unseen data. After evaluation of the trained model, we need to tune hyperparameters if our machine learning model requires further improvement. The tuning process

is evaluated by changing hyperparameters such as epoch, learning rate. Here, the learning rate is a significant factor in tuning. It defines how fast our model reaches good accuracy.

Now the final step in machine learning workflow is a prediction. It means we get the correct answer to our questions.

### 3.1.1 Types of machine learning

Several machine learning approaches have been developed to perform a particular task and solve the problems in various fields. Machine learning approaches are broadly categorized into four types based on the training procedure. The following are the main categorization of the ML approaches (Stuart Russell *et al.* 2010 and Phil kim, 2017).

- Supervised learning
- Unsupervised learning
- Semi supervised learning
- Reinforcement learning

At the beginning of the ML research, researchers started to solve the problems with supervised learning approach. That was the prediction of the house prices. Afterwards, the unsupervised learning approach is developed where the system can learn on its own. Researchers have discovered further a new method known as reinforcement learning. It used in the situation where the system can learn from the mistakes and react to an environment.

#### 3.1.1.1 Supervised learning approach

The process of the supervised learning approach is that a machine learns things similar to a human learns things. In this technique, the machine learning algorithm uses data of input and labeled/ desired output for training. Then the trained model generates a function that maps input data ( $X$ ) to corresponding labeled/desired outputs ( $Y$ ) and makes prediction output ( $Y^{\wedge}$ ) on the new test input data ( $X_{test}$ ). The resultant mapping function from the ML model and prediction output demonstrate as

$$Y = \varphi(X) \tag{3.1}$$

$$Y^{\wedge} = \varphi(X_{test}) \tag{3.2}$$

Two main applications of supervised learning are regression and classification.

#### **3.1.1.1.1 Regression**

In this application, the supervised learning algorithm is used to estimate the continuous values. Typical example problem, if you have data on house prices and corresponding features of the home like size or location. And we want a machine learning model that predicts the prices of a house based on the given the characteristics of the house, known as a regression problem.

#### **3.1.1.1.2 Classification**

Supervised learning algorithms are used to predict the class of labels. An example of this problem we consider handwriting images as input and class of label (numbers 0 to 9) as output. The classification problem is predicting the classes in which the hand writing image belongs.

#### **3.1.1.2 Unsupervised learning approach**

In this approach, the machine learning algorithm uses only input data without any desired output for the training process. Applications of unsupervised learning are clustering and density estimation. Estimating the group in the training data is nothing but clustering. Summarizing the distribution in the training data is density estimation.

#### **3.1.1.3 Semi supervised learning approach**

Training data of semi supervised learning contains few of the labeled data and a lot of unlabeled data.

#### **3.1.1.4 Reinforcement learning approach**

In this approach, the system learns from its mistakes and interacts with an environment. We offer a reward function to the learning agent or machine and let it estimate best solution to get the tremendous rewards. The application of this approach is playing a game where the machine chooses a random move, and the machine received an award if it is right to move otherwise received a punishment. Gradually machine will start to learn the right moves, and finally it would figure out the best solution. The accuracy of the machine game would be better with the experience of more games.

### **3.2 Neural networks**

A neural network is one of the machine learning algorithms which was inspired by the human neuron or nerve cells, and it was first designed by McCulloch & Pitts (1943). The human brain

composed of 100 billion neurons, communicates through electrical signals and chemical signals. The nerve cells are connected by the electrochemical junctions, which are known as synapses (located at the dendrites). Each nerve cell makes a lot of connections with neighboring nerve cells and continuously receives incoming signals, which finally reaches the cell body. If the incoming electrical signals are more significant than the threshold level, then the nerve cells will produce a voltage impulse, will be transmitted to another nerve cell through an axon. Artificial neurons are known as nodes. Neural networks formed by the thousands of simulated neurons/nodes. Synapses are represented by the weights in the artificial neural network. The input of the neuron is equal to the sum of the weighted outputs from the other neurons shown in figure 3.4. Each input ( $X_1$  or  $X_2$ ) multiplied by the weight ( $W_1$  or  $W_2$ ). The output of the neuron can be possible to estimate as

$$Y = \varphi(W_1 * X_1 + W_2 * X_2 + b) \quad (3.3)$$

where  $X_1$ ,  $X_2$  are represented as inputs,  $W_1$ ,  $W_2$  are as weight, and  $b$  is bias. The function  $\varphi$  denoted as activation function, which provides non-linearity nature into the output ( $Y$ ) of the neuron. The activation function plays a vital role in the network because data is nonlinear in the real world. Therefore, neurons in the network have to learn this non-linearity nature, and recently several activation functions developed. Popular activations are sigmoid function, tanh, and RELU (rectified linear unit) activation function.

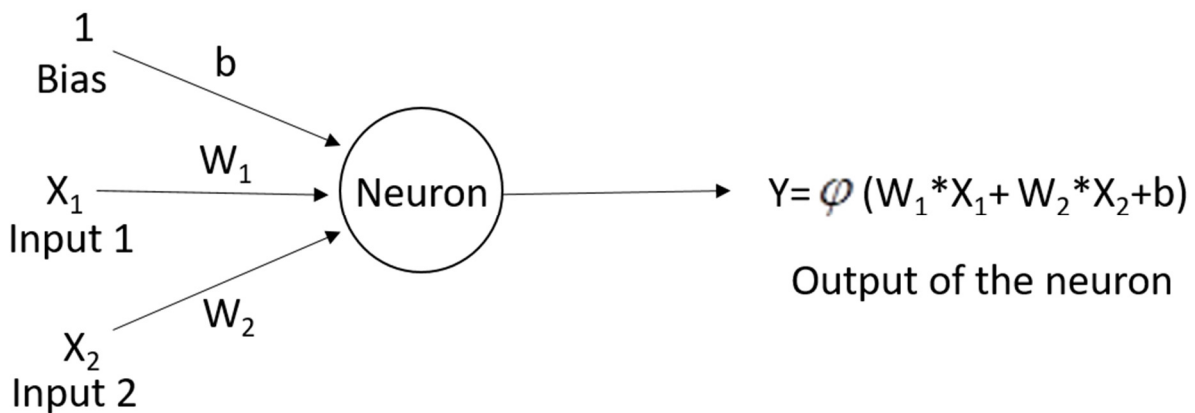


**Figure 3.4. Structure of the artificial neuron.**

An artificial neural network consists of three layers, as shown in figure 3.5. The first one is the input layer, second hidden layer and last one is output layer.

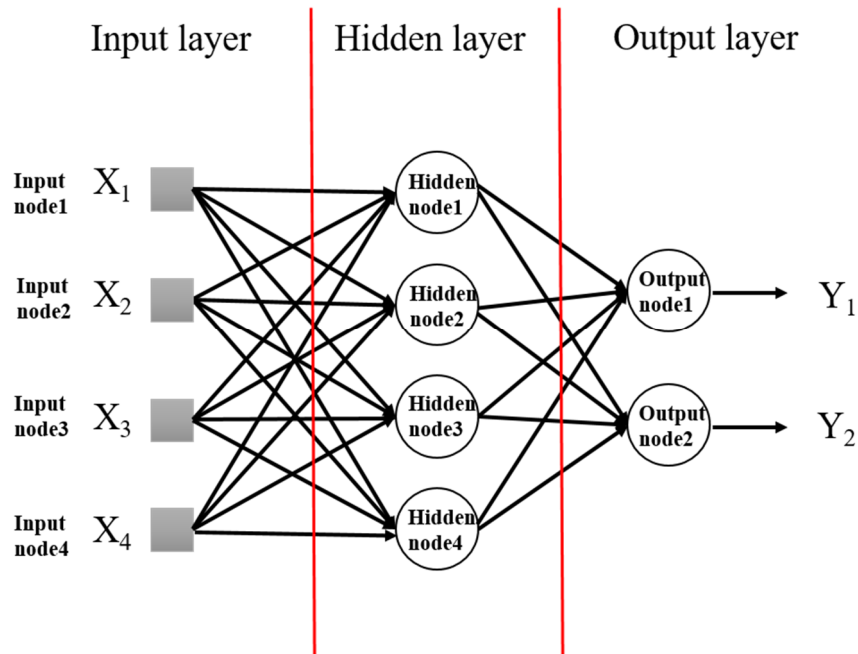


**Figure 3.5. Structure of the neural network.**

In the input layer, neurons provide raw data to the network. The hidden layer is the middle layer between the input and output layers. Each neuron in the hidden layer receives data from the nodes in the input layer, applies the activation function, and transmits to the neurons in output layer. The output layer is the final layer in the artificial neural network. The activity of the output layer is to receive data from the hidden layer nodes and produce an output as predicted result of your algorithm.

### **3.3 Training of the single layer neural network**

The artificial neural network keeps data in the form of weights. Therefore, to train the artificial neural network with training data, the weights of the network should be modified according to the training data. The process of updating weights and bias as per training data is known as learning rule. To train the single layer neural network, we employ delta rule. Widrow and Hoff (1960) proposed and developed the delta rule and the single layer neural network, as shown in figure 3.6.

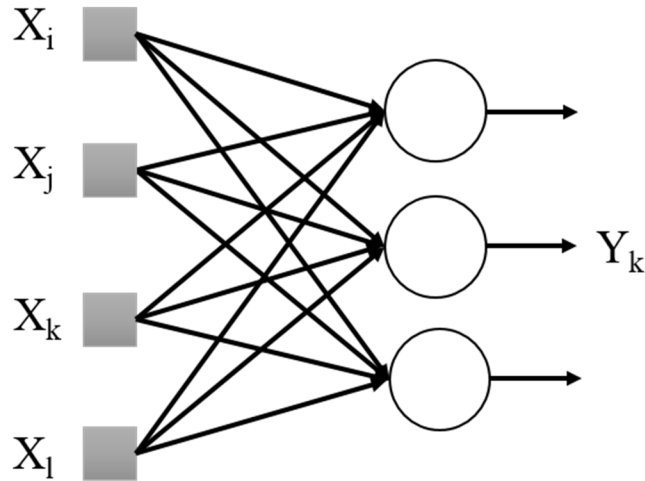


**Figure 3.6. Structure layer neural network.**

Delta rule states that updating the weight of neurons is equal to the multiplication of error and the input of the neuron. Another way to demonstrate the delta rule is that if the input neuron is a factor to the error of output neuron, the weight of the neuron is updated in proportion to the input of the neuron and output error. Then error can be written as

$$e_k = d_k - y_k \quad (3.4)$$

Updating the weights according to delta rule is represents as

$$w_{kj} \leftarrow w_{kj} + \alpha e_k x_j \quad (3.5)$$

where  $e_k$  represents the error of the output neuron  $k$ ,  $x_j$  is output from the input neuron  $j$ , the learning rate  $\alpha$  is ( $0 < \alpha \leq 1$ ), and  $w_{kj}$  is the weight value between the output neuron  $k$  and input neuron  $j$ . Training process of the single layer neural network using the delta rule is shown in figure 3.7.

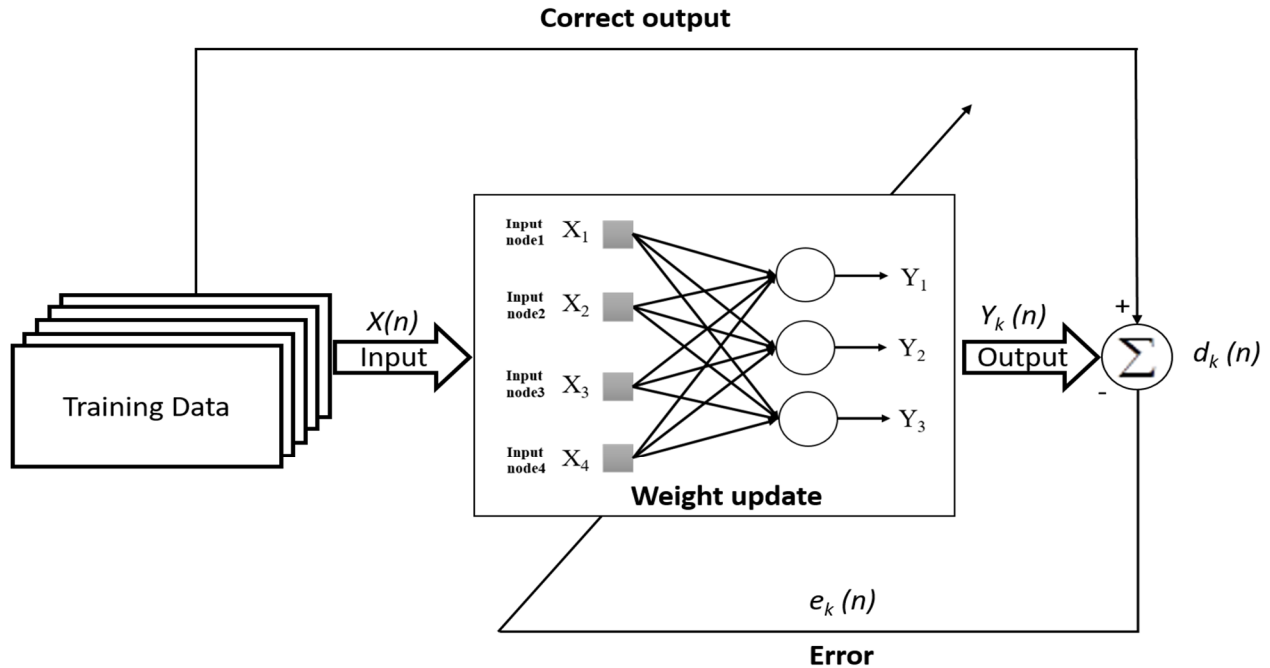


**Figure 3.7. Training process of the single layer neural network.**

**The steps for the training process of the single layer neural network using delta rule is as follows:**

Step1: Initialize the weights of the neurons with the small random number values

Step2: Compute the output error, which is the difference between the desired output and the actual output.

$$e_k = d_k - y_k$$

Step3: Update the weights and bias of the nodes according to the delta rule.

$$w_{kj} \leftarrow w_{kj} + \alpha e_k x_j$$

Step 4: Do the steps 2-3 until the output error reaches acceptable value.

### 3.4 Training of the multi-layer neural network

The multi-layer neural network is developed to mitigate the limitations of the single layer neural network. However, it has taken 30 years to upgrade the single layer with the addition of the hidden layer. A proper training method is more important to train the multi-layer neural network. As we discussed in the last section, delta rule is not an efficient technique to train the multi-layer neural network as the error is not determined in the hidden layer. According to the delta rule, output error is the difference between desired output and the actual output of the neural network. However, in case of the multi-layer neural network, the desired output of hidden neurons is not produced by the training data. Hence error cannot be determined in the hidden layer using delta rule.

The back propagation algorithm was developed by David Rumelhart, Geoffrey Hinton, and Ronald Williams in 1986, to train the multi-layer neural network. In this method, the computation of the output error starts from the output of the neural network and then calculate back up to the first hidden layer in the multi-layer neural network, as explained in figure 3.8

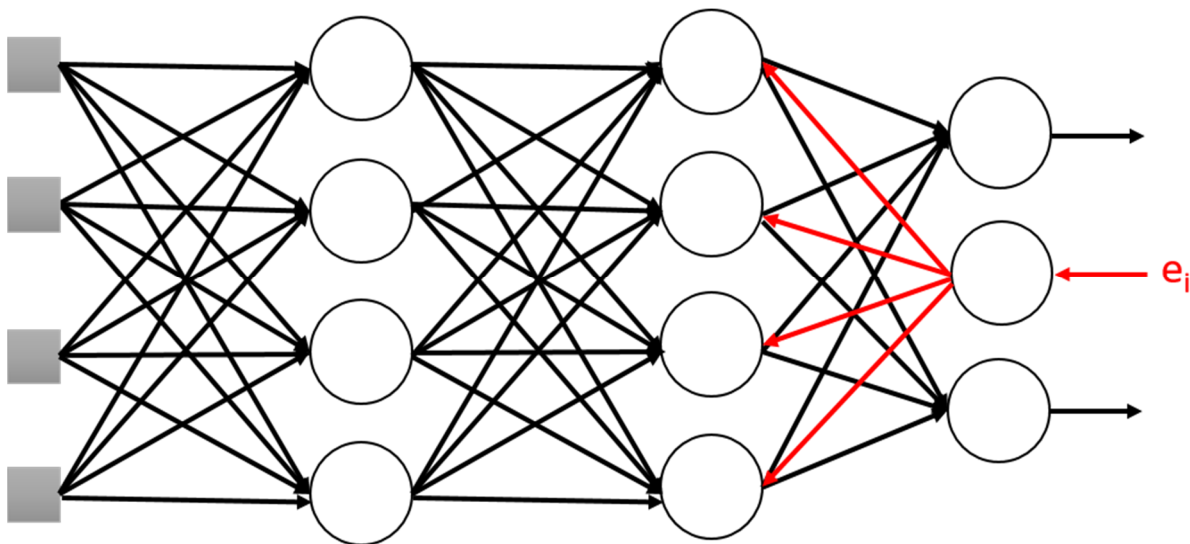


**Figure 3.8. Illustration of the training process for the multi-layer neural networks using back propagation algorithm.**

The steps for the training process of the multi-layer neural network using back-propagation are as follows:

Step1: Initialize the weights of the neurons with the small random number values.

Step2: Compute the neural network output error from the training input data, which is the difference between the desired output and the actual output. And obtain the delta  $\delta$  of the output neuron as follows.

$$e_k = d_k - y_k \quad (3.6)$$

$$\delta = \varphi'(v)e \quad (3.7)$$

Step3: compute the delta to each output node from the backward as follows

$$e^{(k)} = W^T \delta \quad (3.8)$$

$$\delta^{(k)} = \varphi'(v^{(k)})e^{(k)} \quad (3.9)$$

Step4: Perform the step3 until it reaches to the first hidden layer of the network.

Step5: Update the weights and bias in the multilayer neural network according to the learning rule as follows

$$w_{kj} \longleftarrow w_{kj} + \alpha e_k x_j \quad (3.10)$$

Step6: Perform the step 2-5 for each data in the training set.

Step7: Perform the step 2-6 until the model is ready to make estimations with new test data.

### 3.5 Radial basis function network for regression applications.

The radial basis function network algorithm is developed by Moody and Darken in 1989. It is one kind of supervised neural network which is fed forward and a 2-layer artificial neural network. RBF network contains an input layer, hidden layer, and output layer as shown in figure 3.9. The activity of the input layer is to send the input data to the hidden layer. Neurons in the hidden layer provide the set of the bell shaped radial basis function, and it performs a nonlinear mapping from the input data to high dimensionality. The output layer of the network carries out the linear summation of hidden function.

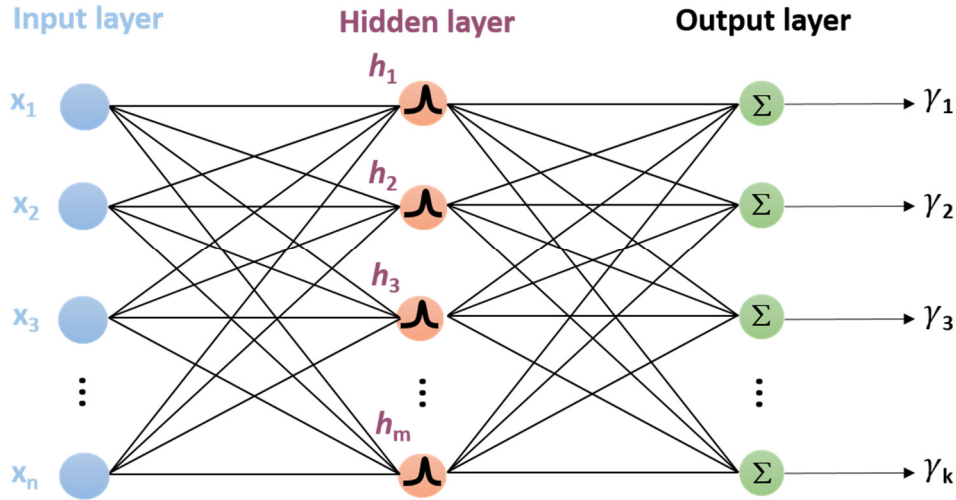


**Figure 3.9. Architecture of radial basis function network.**

Where input of the network is  $x = (x_1, x_2, \dots, x_n)$ , the output is  $\gamma = (\gamma_1, \gamma_2, \dots, \gamma_k)$ , The output of the network according to the radial basis function is expressed as

$$\gamma(x) = \sum_{i=1}^m w_i h_i + b \quad (3.11)$$

Where  $w_i$  represents weights,  $b$  is bias,  $m$  indicates no of the bases and selects the Gaussian function as radial basis function then the  $h_i$  can be written as follows

$$h_i(x, c_i) = \exp\left(\frac{-\|x - c_i\|^2}{2\sigma_i^2}\right) \quad (3.12)$$

Where  $c_i$  represents centers,  $\sigma$  is the width.

In this thesis, the training process of radial basis function network composed of choosing the center, width of the RBF neurons, and updating the widths of the output layer. Therefore, to calculate the centers  $c_i$  and width, we have chosen the k- mean clustering algorithm. Adjust the widths of the output layer using gradient descent (least mean square) method. Then cost function can be written as

$$C = \sum_{j=1}^n (y^{(j)} - \gamma(x^{(j)}))^2 \quad (3.13)$$

We can derive the updating rule for weights and bias of the output layer that can be expressed as

$$w_i \longleftarrow w_i + \eta \sum_{j=1}^n (y^{(j)} - \gamma(x^{(j)}))^2 \quad (3.14)$$

Finally, we implemented the RBF neural network model for regression.

## 4 . Deep learning

### 4.1 Introduction of deep learning

Deep learning is a class of the machine learning algorithm which uses deep neural network architecture. As we discussed in chapter 3, deep neural network is composed of neural network with more than two hidden layers. The mechanism of deep learning is illustrated in figure 4.1.

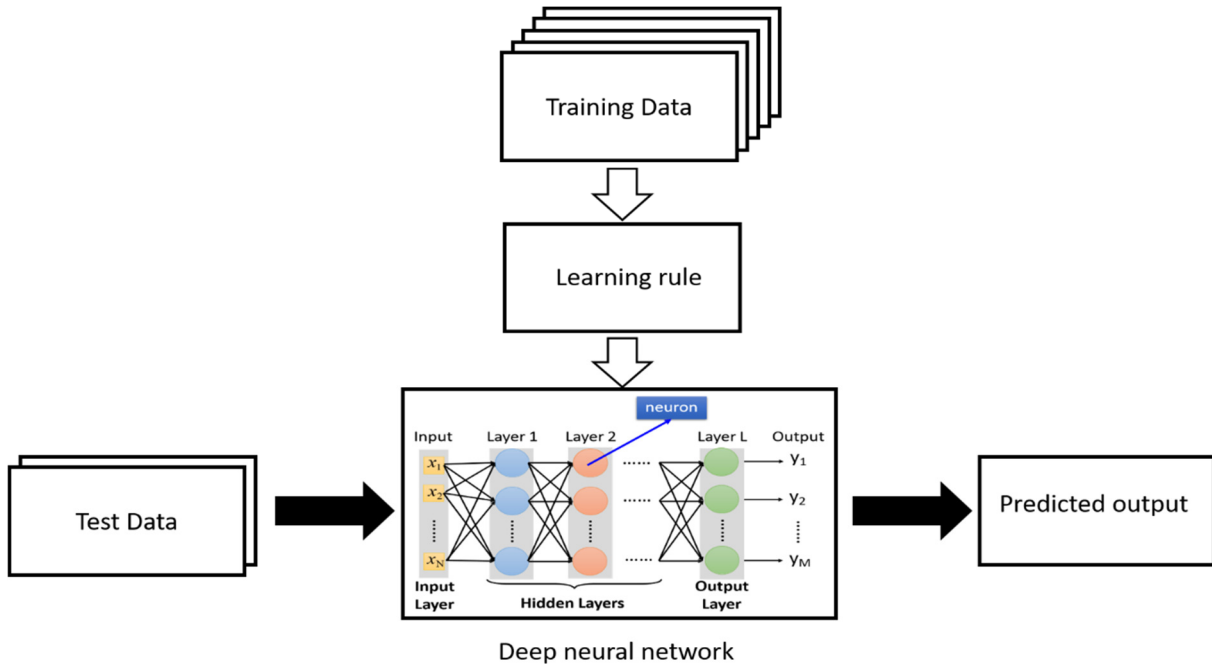


**Figure 4.1. Mechanism of deep learning.**

It has taken 30 years to upgrade the single layer to multi-layer neural network. Training problem of multi-layer neural network is overcome with back propagation algorithm. However, the performance of multilayer neural network was very poor on practical problem though including more number of hidden layers. After a lots of experiments and attempts to improve the performance, many of the researchers have admitted that neural network gives poor performance. Finally, multilayer neural net was faded away over the 20 years until the deep learning was developed. Deep learning could improve the performance of the multi-layer neural network. In the training stage of deep neural network, backpropagation algorithm has encountered a few complications as follows

## 4.2 Vanishing gradient:

Vanishing gradient is a major difficulty to train the deep neural network due to poor performance of the model and lengthy training procedure. It occurs when we employ gradient based optimization methods to train a deep neural network model, that is gradients of error tends to get smaller and fail to reach the neurons in the earlier layers. Therefore, it takes long time to train the earlier layer and not properly trained in the deep learning network as shown in the figure 4.2. Performance accuracy of the network will degrade due to long training process time. Sigmoid and Tanh activation functions in the neural network causes vanishing gradient problems. RELU activation function in training process of deep learning can overcome vanishing gradient problem and improve the performance accuracy of the deep neural network.

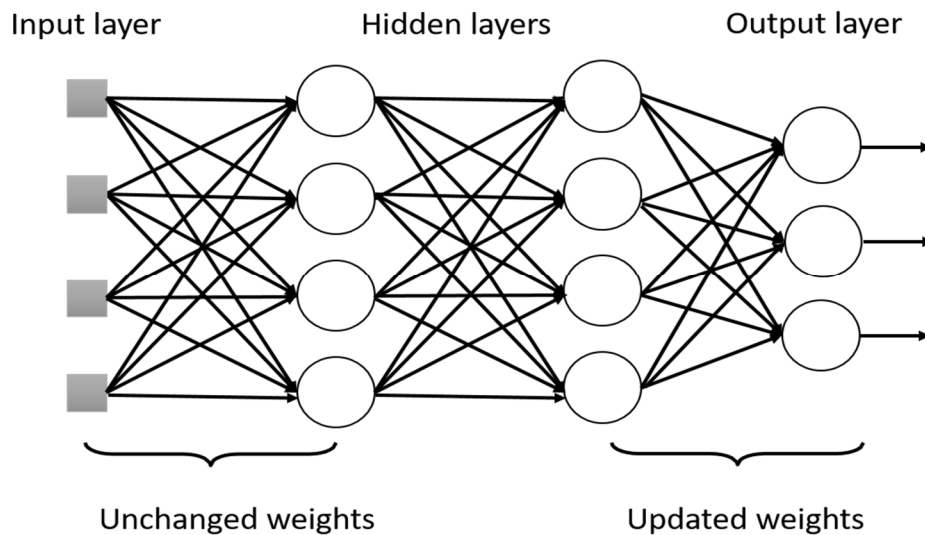


**Figure 4.2. Illustration of the vanishing gradient problem in the deep neural network model.**

### 4.2.1 Rectified linear unit

Rectified linear unit is the activation function that is widely used in the training of the deep neural network model. It is defined as the function that returns 0 for any negative input values and provides  $x$  for any positive  $x$  input value, shown in figure 4.4. Rectified linear unit function can be expressed as follows,

$$\varphi(x) = \begin{cases} x, & x > 0 \\ 0, & x \leq 0 \end{cases} \quad (4.1)$$

$$\varphi(x) = \max(0, x)$$

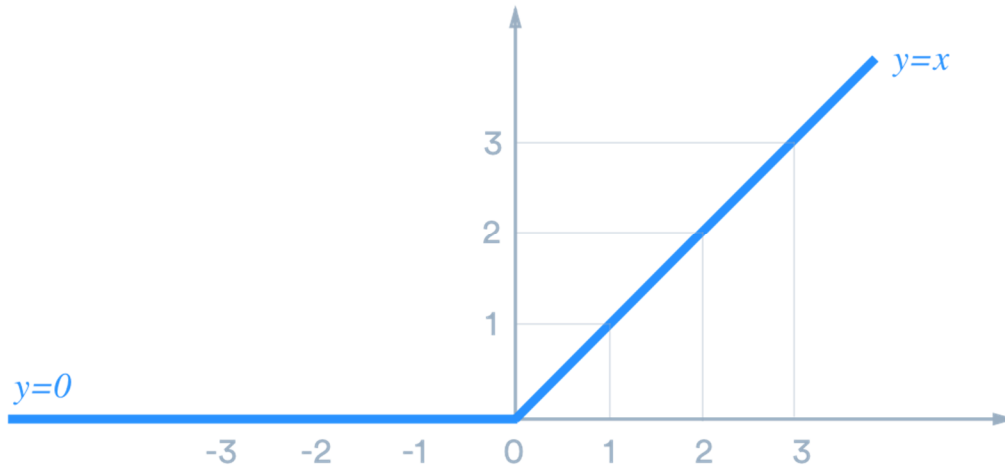


**Figure 4.3. Rectified linear unit function.**

It learns faster and also offers better transmitting the error than the Sigmoid and Tanh activation functions.

### **4.3 Overfitting**

Overfitting problem is a modeling error which occurs when a network that maps training data too close. The complex deep neural network models are more vulnerable to overfitting problem. Various methods have been developed to prevent overfitting problem in deep neural network, such as regularizations (L1 and L2) and drop out. Regularization methods reduce the overfitting problem by adding additional term in the cost function. Another popular method to prevent overfitting is drop out, which trains only few of the randomly selected neurons in the network rather than every neuron in the network. The adequate drop out value is approximately 0.5.

### **4.4 Computational load**

The time required for training the deep neural network is longer due to more computations in network. The computational problem has been solved by using high performance hardware systems, such as GPU. And also with batch normalization algorithms.

### **4.5 Learning algorithm**

#### **4.5.1 Training of the deep neural network**

Deep neural network structure consists of the input layer, more than two hidden layers and output layer as shown in figure 4.5. In this thesis, we constructed deep neural network with three hidden layers. Input layer in the network represents as input vector  $V$ . nodes in the hidden layer 1, 2, and

3 represents activation neurons  $W$  or  $\theta$ . Final layer is output layer that represents predicted output values.

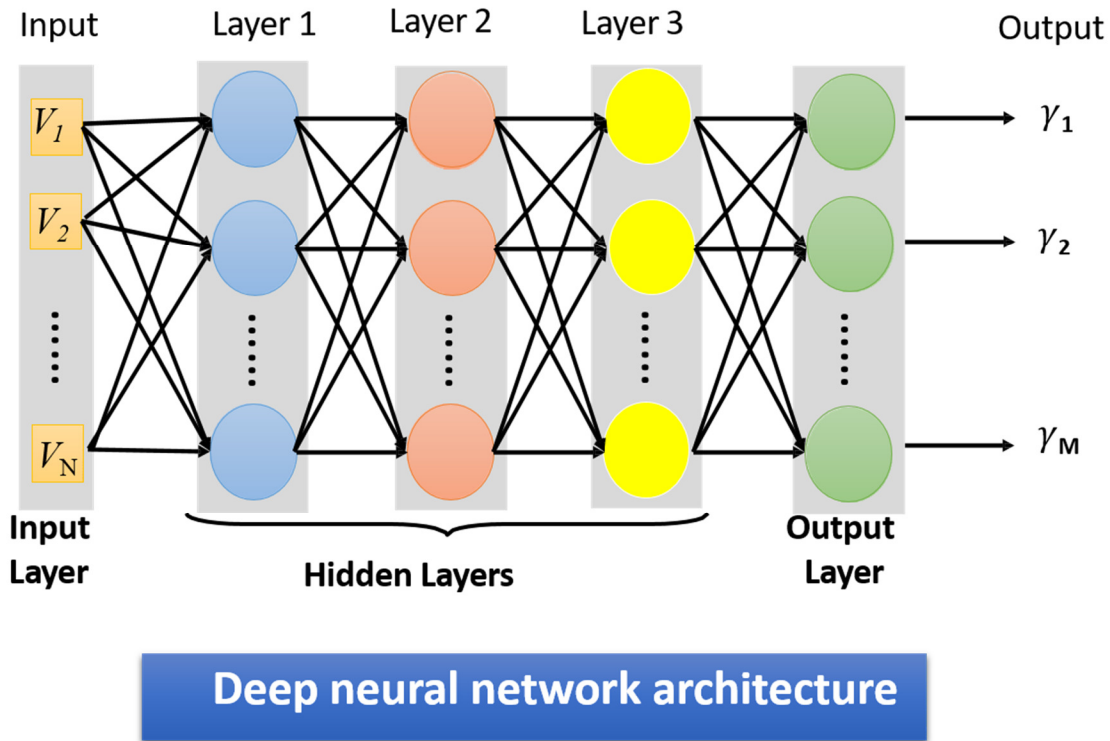


**Figure 4.4. Illustration of the deep neural network structure.**

Every neuron in the layer is connected with each neuron from the next layer. Each connection in the network represents some value of weight. Input value of the nodes in the input layer is multiplied with weight values and send some values to the nodes in the first hidden layer. Nodes in the hidden layer represent the activation function. The weights in the network are denoted as  $W$ . If neural network has “a” number of neurons in layer  $i$  and “b” number of neurons in layer  $i+1$ , then size of the weight matrix is expressed as  $b \times (a+1)$  shown in equation (4.2).

$$W = \begin{pmatrix} w_{11} & \cdots & w_{1n} \\ \vdots & \ddots & \vdots \\ w_{m1} & \cdots & w_{mn} \end{pmatrix} \quad (4.2)$$

Next, we have to calculate the activated neurons for the hidden layer. Input vector value (V) of the nodes in the input layer are multiplied with weight values (W) is (V\*W) and then employ the activation function g can be written as,

$$a_1^{(2)} = g(w_{10}^{(1)}v_0 + w_{11}^{(1)}v_1 + w_{12}^{(1)}v_2 + w_{13}^{(1)}v_3) \quad (4.3)$$

Hidden layer values are multiplied with weight values in the next layer then the hypothesis function can be written as

$$h(v) = a_1^{(3)} = g(w_{10}^{(2)}v_0^{(2)} + w_{11}^{(2)}v_1^{(2)} + w_{12}^{(2)}v_2^{(2)} + w_{13}^{(2)}v_3^{(2)}) \quad (4.4)$$

if deep neural network consists of L layers with n nodes and L-1 layer with m nodes then the activation nodes can be express as follows.

$$a_n^L = [\sigma(\sum_m w_{nm}^L [\dots [\sigma(\sum_j w_{kj}^2 [\sigma(\sum_i w_{ji}^1 v_i + b_j^1)] + b_k^2)] \dots ]_m + b_n^N)]_n \quad (4.5)$$

Activation function: Activation function of the deep neural network defines if a given node is “activated” or not based on the weighted sum. Let us define this weighted sum value as z. In this thesis, we employed Rectified linear unit (RELU). RELU is the activation function that is widely used in the training of the deep neural network model. It is defined as the function that returns 0 for any negative input values and provides x for any positive x input value. RELU of the weighted sum “z” can be expressed as

$$\varphi(z) = \begin{cases} z, & z > 0 \\ 0, & z \leq 0 \end{cases} \quad (4.6)$$

$$\varphi(z) = \max(0, z)$$

Bias node: Bias value of permit to shift the activation function by adding the small constant to input node for accurate mapping of data.

### Understanding the Cost Function in the deep neural network:

Cost function is defined as sum of the error between the estimated output value and the desired output value in the deep neural network model. It is used to estimate how bad the deep neural network model is in terms of its ability to predict the mapping between the input and output. The objective of a deep neural network is to estimate the weights of the nodes in the network which

minimizes the value of the cost function as expressed in equation (4.4). In thesis, we employed the Adam optimization algorithm to minimize the cost function.

$$J = \frac{1}{m} \sum_{i=1}^m \text{cost}(h(v^{(i)}), y^{(i)}) \quad (4.7)$$

Square error of cost function can be written as follows,

$$J = \frac{1}{2m} \sum_{i=1}^m (h(v^{(i)}) - y^{(i)})^2 \quad (4.8)$$

where,  $h(v^{(i)})$  is the predicted output from the deep neural network and  $y^{(i)}$  represented as desired output.

#### 4.5.2 Adam optimization algorithm to minimize the cost function in the deep neural network

Adam is an adaptive learning rate optimization algorithm and it is used to update weights of the deep neural network based on the epoch of the training. The word Adam is originated from adaptive moment estimation. Adam optimization algorithm was developed by Diederik Kingma and Jimmy Ba in 2015 (Kingma and Ba, 2015). Adam is a combination of the adaptive gradient descent algorithm and the RMS prop (Root Mean Square Propagation) algorithm.

Let the cost function  $J(\theta)$  and  $g_t = \nabla_{\theta} J_t(\theta)$  represent the gradient, that is vector of the partial derivatives of the  $J_t$  with respect to the parameter  $\theta$ . It computes exponential weighted moving average of the gradient  $m(t)$  and squared of the gradient is  $\vartheta(t)$ . It consists of two decay parameters  $\beta_1, \beta_2 \in [0,1)$  that control the decay rates of calculated moving averages.

The moving average estimates the first moment and the second raw moment of the gradient. However, these moving averages are initialized with zero, bias-corrected estimates are  $\hat{m}(t)$  and  $\hat{\vartheta}(t)$ , presents as follows

$$m(t) = \beta_1 m_{t-1} + (1 - \beta_1) g_t \quad (4.9)$$

$$\vartheta(t) = \beta_2 \vartheta_{t-1} + (1 - \beta_2) g_t^2 \quad (4.10)$$

$$\hat{m}(t) = \frac{m(t)}{1 - \beta_1^t} \quad (4.11)$$

$$\hat{v}(t) = \frac{v(t)}{1 - \beta_2^t} \quad (4.12)$$

Updated rule of the Adam optimization algorithm can be written as follows,

$$\theta_{t+1} = \theta_t - \frac{\eta}{\sqrt{\hat{v}_t} + \epsilon} \hat{m}(t) \quad (4.13)$$

### Pseudo-code of the Adam optimization algorithm

Initialize the step size

$\beta_1, \beta_2 \in [0, 1)$ : Exponential decay rates for the moments estimates

$J(\theta)$  objective function with respect to the  $\theta$

Initialize the initial parameter vector  $\theta$

Initialize the first movement vector  $m_0 \leftarrow 0$

Initialize the second movement vector  $v_0 \leftarrow 0$

Initialize the time step  $t \leftarrow 0$

While  $\theta$  not converged do

$t \leftarrow t + 1$

Get the gradient of the objective function  $g_t \leftarrow \nabla_{\theta} J_t(\theta_{t-1})$

Update biased first moment estimate  $m(t) \leftarrow \beta_1 m_{t-1} + (1 - \beta_1) g_t$

Update biased second raw moment estimate  $v(t) \leftarrow \beta_2 v_{t-1} + (1 - \beta_2) g_t^2$

Compute bias corrected first moment estimate  $\hat{m}(t) \leftarrow \frac{m(t)}{1 - \beta_1^t}$

Compute bias corrected second raw moment estimate  $\hat{v}(t) \leftarrow \frac{v(t)}{1 - \beta_2^t}$

Update parameters  $\theta_{t+1} \leftarrow \theta_t - \frac{\eta}{\sqrt{\hat{v}_t} + \epsilon} \hat{m}(t)$

End while

Return  $\theta$  (Resulting parameter)

### 4.5.3 Process of the forward propagation in the deep neural network

Forward propagation calculates the neural network output value based on a given input value, it is used to compute the objective function. We get hypothesis function from the equation (4.4)

$$h(v) = a_1^3 = g(w_{10}^{(2)} v_0^{(2)} + w_{11}^{(2)} v_1^{(2)} + w_{12}^{(2)} v_2^{(2)} + w_{13}^{(2)} v_3^{(2)})$$

Compute the cost function value for the given input variable as follows

$$v = a^{(1)} \quad (4.14)$$

$$z^{(j+1)} = w^{(j)} a^{(j)} \quad (4.15)$$

$$a^{(j+1)} = \sigma(z^{(j+1)}) \quad (4.16)$$

$$h(v) = a^{(L)} = \sigma(z^{(L)}) \quad (4.17)$$

#### 4.5.4 Backpropagation algorithm for deep neural network

In order to minimize the objective function  $J(\theta)$  by updating the optimal values of weights  $\theta$ . Backpropagation method is used for calculating the partial derivative of the objective function  $J(\theta)$ . Partial derivative value is then used in Adam optimization algorithm for computing the weights in deep neural network that minimize the cost function  $J(\theta)$ . Adam update equation for weights  $\theta$  is represented as

$$\theta_{t+1} = \theta_t - \frac{\eta}{\sqrt{\hat{\vartheta}_t} + \varepsilon} \hat{m}(t)$$

Step for implementing the back propagation algorithm is as follows,

- Consider  $a^{(1)} = v$  for all the training samples in data set
- Perform forward propagation and compute  $a^{(i)}$  for the other layers  $i = 2 \dots L$
- From desired output, calculate the delta value for the last layer  $\delta(L) = (h(v^{(L)}) - y^{(L)})$
- Calculate the  $\delta(i)$  values backwards for each layer
- Calculate derivative values  $\Delta(i) = ((a^{(i)})^T * \delta(i+1))$  for each layer, which represent the derivative of cost function  $J(\theta)$  with respect to  $\theta(i)$  for layer  $i$ .

## **5 . Estimating human urinary bladder boundary using a deep learning algorithm**

Bladder size estimation is essential for patients who are suffering from urinary incontinence (UI), which is known as involuntary leakage of urine due to neurological disorders (Phelan and Franks 2001, Anderson 2004). Continuous and accurate bladder size estimation could help to provide better treatment of the patient. Several bladder monitoring methods were developed to estimate the size of the bladder, which provides accurate bladder volume measurements. Despite the advantages of conventional methods such as CT and ultrasound, these methods are not suitable for the continuous monitoring of bladder, due to radiation exposure and requires professionals to operate devices.

Electrical impedance methods have been applied to monitor and estimate the size of the urinary bladder in the last few years. The physiological concept of this method depends on the relation between the electrical impedance measurements and bladder volume, that means variations in bladder urinary volume could cause the corresponding variations in electrical impedance (kim *et al.* 1998). Although, several studies described that correlation between the urinary bladder volume and electrical impedance measurements may not be valid in real time situations. Moreover, the shape of the bladder in reconstructed image is not clear due to poor spatial resolution. Therefore, boundary estimation approach in EIT may help to improve the urinary bladder shape and size estimation.

EIT image has very poor spatial resolution due to ill-posedness. Thus, the poor spatial resolution of EIT makes it difficult to reconstruct the boundaries of regions inside the object. If the internal resistivity distribution values of the object can be known a priori then the inverse problem in EIT becomes estimating the boundary, size, position of the regions inside the object. The approach to estimate region boundaries rather than internal resistivity distributions is known as boundary estimation in EIT. Moreover, in the field of medical imaging methods for bladder monitoring, estimating urinary bladder shape, location, and size are essential clinical parameters rather than estimating conductivity distribution of human bladder. But it is complicated to reconstruct the bladder shape and size due to poor spatial resolution in EIT reconstruction, therefore lessening the effectiveness of its anatomical significance. The human pelvic contains a few neighboring tissues such as the urinary bladder, Sacrum, Rectum, Gluteus Maximus muscle, and Medius muscle

enclosed by background tissue. If the electrical conductivity values of background tissue and neighboring tissues of the bladder in the pelvic domain are known a priori, then the estimation of human bladder size and boundary inside the pelvic region will be unknowns of the inverse problem. Moreover, the performance of these conventional methods highly depend on choosing the initial guess, accurate computation of Jacobian and often fail to provide significant results in clinical environment.

This study presents a deep neural network algorithm to estimate the size, shape, and location of the urinary bladder inside the human body. The boundaries of the urinary bladder, neighboring tissues such as Rectum, Gluteus Maximus muscle, and Medius muscle are approximated by truncated Fourier series. The electrical conductivity values of background tissue, bladder, and neighboring tissues inside the pelvic domain are known a priori. A deep neural network to estimate urinary bladder boundary inside the pelvic domain using electrical impedance tomography is proposed. The proposed algorithm is evaluated by performing the numerical simulation and pelvic shape phantom experiments.

### 5.1 Boundary representation of the human urinary bladder

This section involves the urinary bladder and neighboring tissue boundary shape parameterization. The region boundaries inside the pelvic region are approximate by the truncated Fourier series approach. Since the electrical conductivity values of background tissue, bladder, and neighboring tissues inside the pelvic domain are known a priori, the coefficients that represent the boundary are estimated instead. The forward solver is then changed correspondingly as a set of Fourier coefficients representing the boundary shape of bladder and neighboring tissues.

Let us assume a pelvic domain  $\Omega \in \mathbb{R}^2$  with  $\tilde{N} + 1$  bladder and neighboring tissue boundaries  $A_m$  schematically illustrated in figure 5.1.

$$\Omega = \bigcup_{m=0}^{\tilde{N}} A_m. \quad (5.1)$$

The boundary of the pelvic region  $A_0$  is  $\partial\Omega$  whereas the urinary bladder and neighboring tissues regions  $A_m (m=1, \dots, \tilde{N})$  with boundary  $C_m \in \Omega (m=1, \dots, \tilde{N})$ . The characteristic function of tissue

regions  $A_m$  is  $\chi_m(r)$ , the electrical conductivity inside the pelvic region is assumed as constant and written as follow

$$\sigma = \sum_{m=0}^{\tilde{N}} \sigma_m \chi_m(r). \quad (5.2)$$

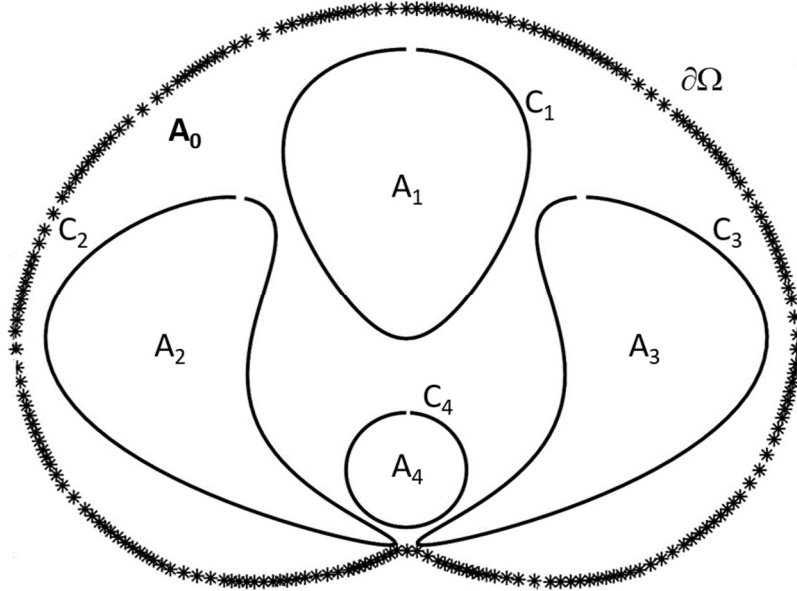


**Figure 5.1. A schematic diagram of urinary bladder and neighboring tissue boundaries inside the pelvic region.**

Boundaries  $C_m$  inside the pelvic region are sufficiently smooth and they can be expressed as Fourier series coefficients (Kolehmainen *et al.* 2001).

$$C_m(s) = \begin{pmatrix} x_m(s) \\ y_m(s) \end{pmatrix} = \sum_{n=1}^{N_\phi} \begin{pmatrix} \gamma_n^{x_k} \theta_n^x(s) \\ \gamma_n^{y_k} \theta_n^y(s) \end{pmatrix}, m = 1, 2, \dots, \tilde{N} \quad (5.3)$$

The tissue boundaries are denoted as  $K$ ,  $N_\phi$  number of basis functions,  $\theta_n^x(s)$  and  $\theta_n^y(s)$  are the periodic basis functions of the form

$$\begin{aligned}
\theta_n^\alpha &= 1, & n &= 1 \\
\theta_n^\alpha &= \sin(2\pi \frac{n}{2} s), & n &= 2, 4, 6, \dots, N_\phi - 1 \\
\theta_n^\alpha &= \cos(2\pi \frac{n-1}{2} s), & n &= 3, 5, 7, \dots, N_\phi
\end{aligned} \tag{5.4}$$

The curve parameter is expressed as  $s \in [0, 1]$  and  $\alpha$  indicate x or y. The tissue boundaries  $C_m$  can be expressed as  $\Phi$  shape coefficients, that is,

$$\Phi = (\gamma_1^{x_1}, \dots, \gamma_{N_\phi}^{x_1}, \gamma_1^{y_1}, \dots, \gamma_{N_\phi}^{y_1}, \dots, \gamma_1^{x_M}, \dots, \gamma_{N_\phi}^{x_M}, \gamma_1^{y_M}, \dots, \gamma_{N_\phi}^{y_M})^T \tag{5.5}$$

where,  $\Phi \in \mathfrak{R}^{2\tilde{N}N_\phi}$ . Now deep neural network algorithm is employed as an inverse solver to estimate the Fourier coefficient of bladder boundary inside the pelvic domain with injected alternating currents and measure the induced voltages on the skin electrodes.

## 5.2 Deep neural network architecture to estimate human bladder size, shape, and location.

As mentioned earlier, deep learning is a class of the machine learning algorithm which uses deep neural network architecture. Deep neural network is composed of network with more than two hidden layers. The working principle of the deep neural network model for estimating urinary bladder in the EIT consists of the two parts. First part involves the designing and training the of the DNN model. Another part is to evaluate the trained DNN model with unseen test data.

### 5.2.1 Designing and training the of the DNN model

In this thesis, we have designed a 5-layer deep neural network for image reconstruction of urinary bladder in EIT, which are one input layer, 3 hidden layers and output layer as illustrate in figure 5.2. Number of nodes in the input layer, 3 hidden layers and output layer are 128, 64, 32, 16, 8, respectively. Before the training phase of the network, we generated the training data set using simulations of pelvic shaped finite element mesh with bladder shaped target. The training data set contains boundary voltage measurements from simulations of different size, shape, location of urinary bladder inside the pelvic domain and corresponding Fourier coefficients which approximates the boundary, location of the bladder. Then we trained the DNN with the 500 pairs  $\{(V^k, \gamma^k) : k = 1, \dots, K\}$  of the boundary voltage measurements  $V = (V_1, V_2, V_3, \dots, V_N)$  of pelvic

domain as input data and the corresponding Fourier coefficients  $\gamma = (\gamma_1, \gamma_2, \gamma_3, \dots, \gamma_M)$  of internal bladder boundary as output data.

Where  $V_N$  is boundary voltage of  $N$  ( $N=128$ ) independent measurements that are fed to input layer of 128 neurons and the corresponding Fourier coefficients values  $\gamma_M$  ( $M=8$ ) to output layer of 8 neurons. We have employed Adam optimization algorithm, which is used to update weights of the deep neural network based on the epoch of the training. The number of training epochs was considered as 500, the batch size was 8 and learning rate to be 0.001. The deep neural network was designed and trained using the TensorFlow Deep learning software library.

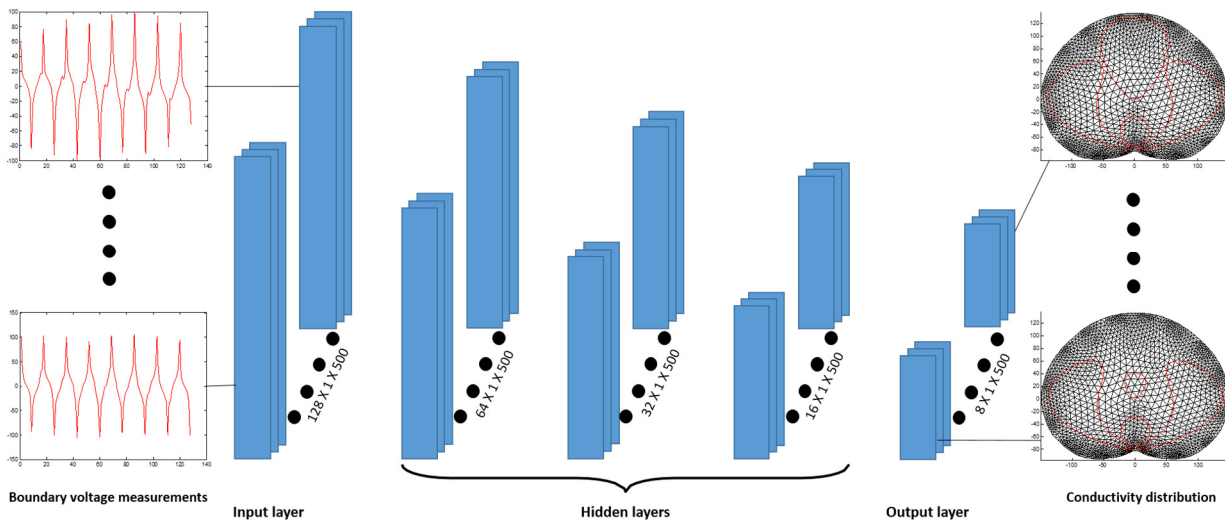


**Figure 5.2. Training scheme of deep neural network.**

### 5.2.2 Evaluating the DNN model

In order to test the trained DNN model, we have performed simulations and phantom experiments. The simulations for 3 cases of different size, location of the bladder inside the pelvic domain were considered. The boundary voltage measurements of test cases were used to obtain the boundary estimation of the urinary bladder. In the experimental study, we have designed pelvic shaped phantom with bladder shaped target and other neighboring tissue shaped targets. Similar to

simulations, 3 cases of different size, location of the bladder shaped target placed in the pelvic phantom were considered, as shown in figure 5.3.

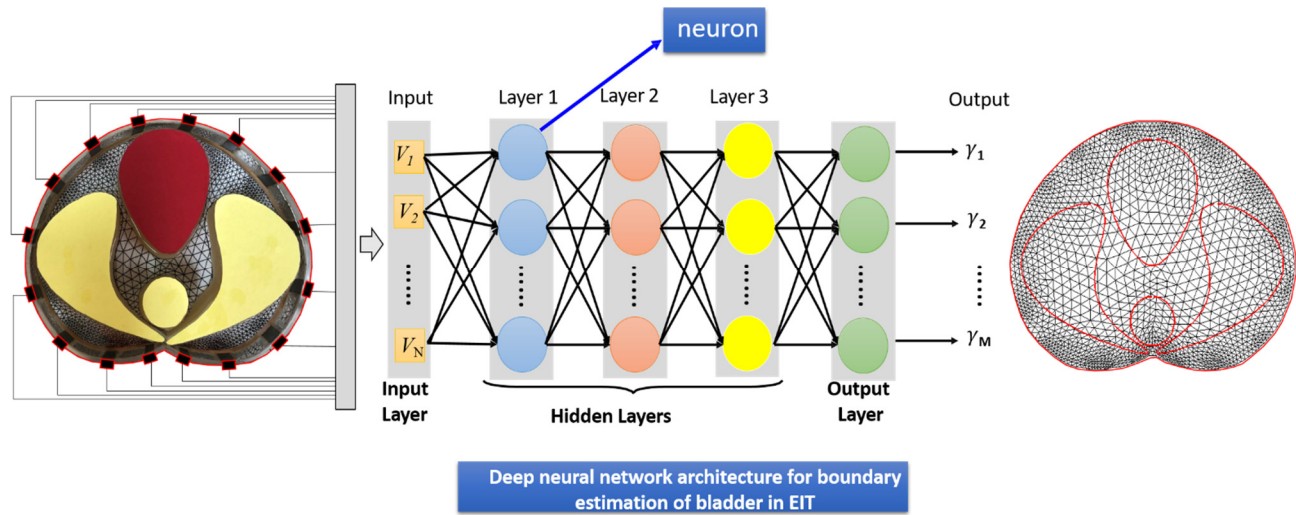


**Figure 5.3. Schematic view of evaluation of the deep neural network for bladder boundary estimation.**

## 5.3 Results and discussions:

### 5.3.1 Numerical studies results

This section demonstrates detailed explanations of numerical simulation results for the deep neural network algorithm to estimate the bladder size, shape, and location inside the pelvic region. Two deep neural network models are designed to investigate numerical simulation studies. The first DNN model was designed to estimate the boundary of bladder shaped target without neighboring tissues inside the pelvic domain. DNN model is trained with 500 simulation cases of bladder shape target of different shape, size, and location inside the pelvic region. Whereas second DNN model was designed to estimate the boundary of bladder shaped target surrounded by three other neighboring tissues, such are Rectum, Gluteus Maximus muscle, and Medius muscle placed inside the pelvic domain.

#### 5.3.1.1 Numerical results for bladder shaped single target inside the pelvic domain

In order to generate the simulation data for training the DNN model, the pelvic shape FEM mesh was designed based on dimension of the pelvic CT scan image data. As per the axial view of pelvic

CT scan image, the lateral dimension is 13 cm, and anterior–posterior (AP) dimension is about 15 cm. To solve the forward problem of bladder EIT, finite element mesh of 3220 triangular elements and 1714 nodes used. Eight Fourier coefficients are required to approximate bladder shaped target inside the pelvic shaped mesh. The electrical conductivities of back ground tissue and bladder are taken as 0.0025 S/cm and 0.02 S/cm, respectively. The contact impedance between the skin electrodes and the pelvic domain is assumed as  $0.005 \Omega \text{ cm}^2$ . In this study, we have injected electrical currents of 1 mA magnitude through the 16 skin electrodes using an opposite injection approach. To train the model, we perform the training of the five-layer DNN with the 500 pairs of the boundary voltage measurements of pelvic domain as input data and the corresponding Fourier coefficients of internal bladder boundary as output data. One training data means one set of 128 independent boundary voltage measurements are fed to input layer of 128 neurons and the corresponding 8 Fourier coefficients values to output layer of 8 neurons. The number of training epochs was considered 500, and the batch size was eight and training rate of 0.001 is used in the training stage of the model.

In the testing stage of the trained model, three simulation bladder cases were used to estimate the boundary, size, and location of the bladder through the trained DNN model. Therefore, three sets of 128 boundary voltage measurements are generated as a new unknown test simulation cases. The first test case represents fully filled bladder in the pelvic domain. This test case imitates the situation in which a person feels that bladder is completely filled (full bladder) with urine, so that the boundary of the bladder expands towards upper top of the pelvic region. The next case represents half-filled (medium size) bladder, and final case was almost empty bladder (small size), as shown in figures (5.4~5.6). Comparison of the bladder boundary estimation results for all three bladder test cases using the mNR, RBF and DNN are shown in figure (5.4~5.6). In the RBF method, the number of RBF neurons was taken as 10. The initial guess used in mNR is shown in figure (5.4), and the regularization parameter is chosen as 0.01. We noticed that DNN algorithm gives better bladder boundary estimation when compared to mNR and RBF. The performance results of three methods depict that the mNR method has poor performance even though using very close initial guess.

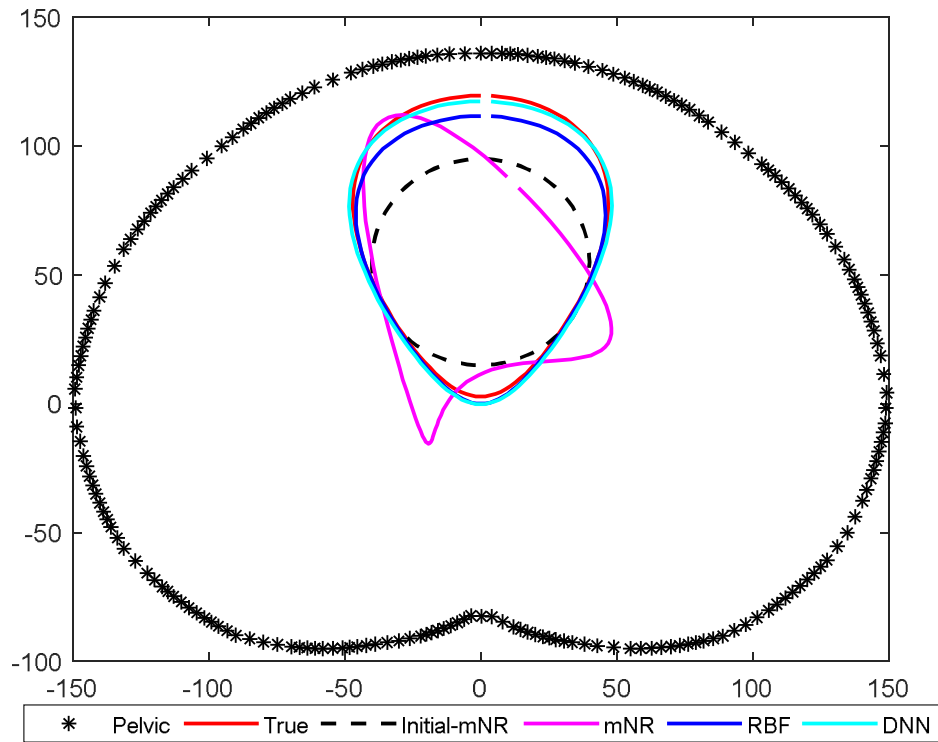


**Figure 5.4. Reconstructed image for a full size bladder in pelvic domain without noise. Asterisk marked line represents pelvic domain boundary, and the red line is true bladder boundary, the dashed line is initial guess of mNR, Magenta line is with mNR method, blue line is with RBF method, and cyan line is using DNN method.**

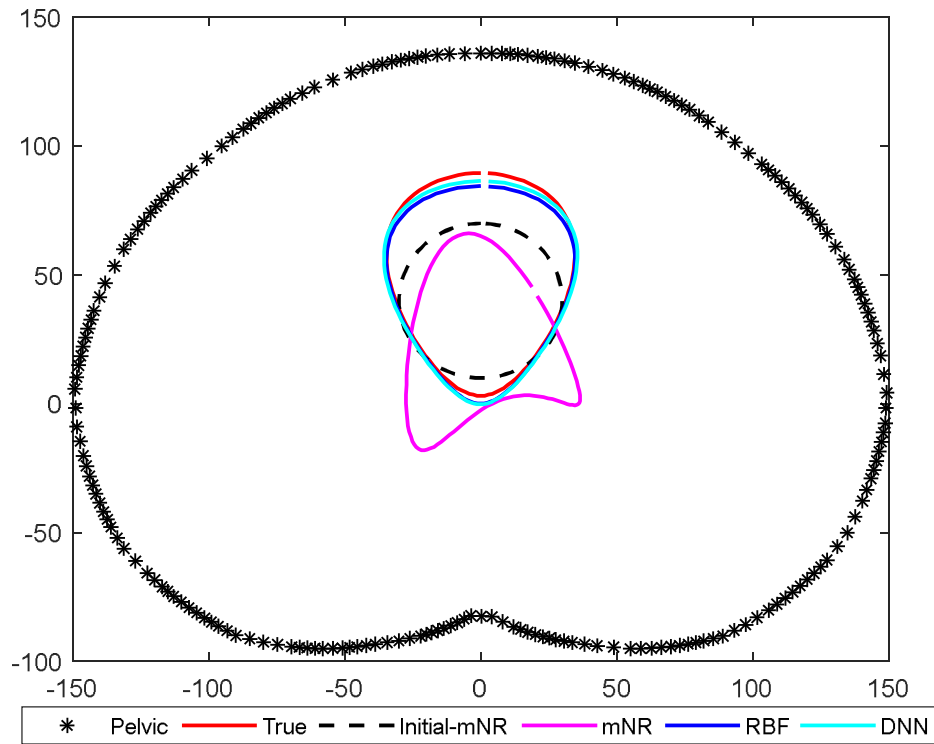


**Figure 5.5. Reconstructed image for a medium size bladder in pelvic domain without noise. Asterisk marked line represents pelvic domain boundary, and the red line is true bladder boundary, the dashed line is initial guess of mNR, Magenta line is with mNR method, blue line is with RBF method, and cyan line is using DNN method.**

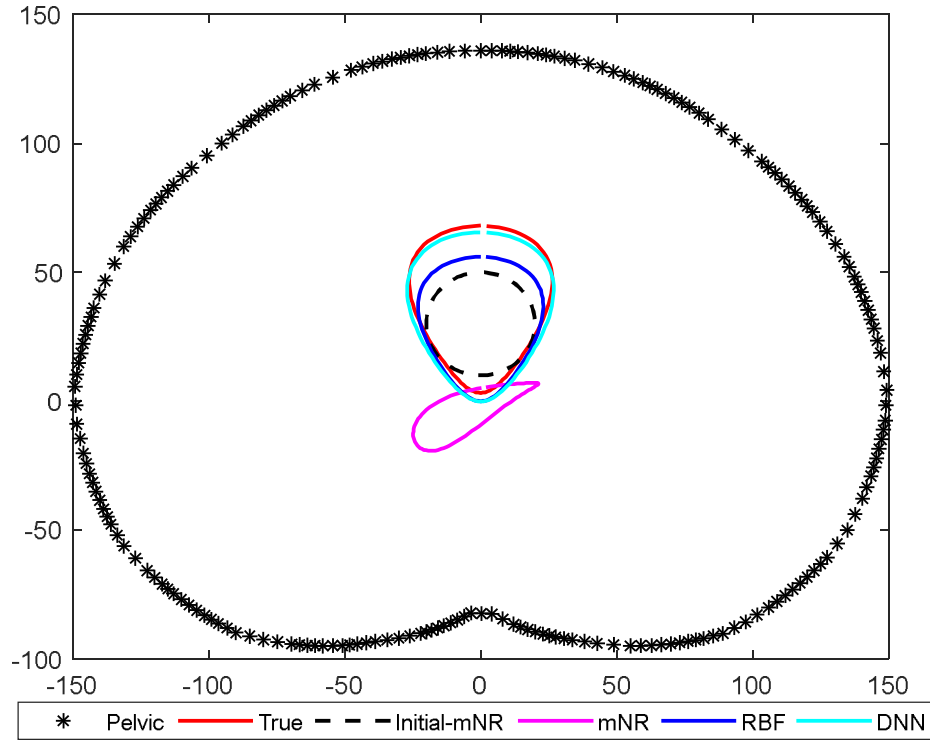


**Figure 5.6. Reconstructed image for a small size bladder in pelvic domain without noise. Asterisk marked line represents pelvic domain boundary, and the red line is true bladder boundary, dashed line is initial guess of mNR, Magenta line is with mNR method, blue line is with RBF method, and cyan line is using DNN method.**

To evaluate the accuracy of three inverse algorithms, multiple statistical parameters were computed, such as RMSE for estimated bladder boundary coefficients, and estimated area. The RMSE for estimated bladder boundary coefficients is written below

$$RMSE_{\gamma} = \sqrt{\frac{(\hat{\gamma} - \gamma_{true})^T (\hat{\gamma} - \gamma_{true})}{\gamma_{true}^T \gamma_{true}}}$$

where  $\hat{\gamma}$  is estimated Fourier coefficients of the bladder and  $\gamma_{true}$  is true Fourier coefficients of bladder boundary. RMSE for estimated Fourier coefficient values and estimated area values are shown in the table (5.1~5.2). Especially, the performance of the algorithm concerning the Fourier coefficients accounting for the size and the location of the bladder should be analyzed very

carefully. From table 5.1 and 5.2, DNN algorithm demonstrates low RMSE for estimated boundary coefficients values and better estimated area compared to mNR and RBF neural network algorithm.

**Table 5.1. RMSE for estimated bladder boundary coefficients for three simulation cases without noise.**

Algorithm	Full size bladder case	Medium size bladder	Small size bladder
mNR	0.5291	0.5469	0.5095
RBF	0.0672	0.2535	0.0980
DNN	0.0271	0.0432	0.0571

**Table 5.2. True and estimated area of bladder boundary for three simulation test cases.**

Algorithm	Full size bladder case	Medium size bladder	Small size bladder
True area	81.6432	44.9209	24.7676
mNR	69.1668	34.9840	19.7517
RBF	74.8035	26.5919	22.7730
DNN	83.7192	45.4919	25.4986

The noise robustness of the proposed algorithm is evaluated by adding 2% of relative noise to the boundary voltage measurements to accounts for numerical error and instrument noise. Comparison of the reconstructed bladder boundary estimation results for all three bladder test cases with 2% relative noise from the mNR, RBF, and DNN algorithms is displayed in figures (5.7~5.9). The below figures (5.7 ~5.9) depicts that the estimated results by the DNN has higher accuracy compared to mNR and RBF algorithms. It also displayed that the size and shape of the bladder are estimated with good accuracy even though boundary voltage measurements are contaminated with 2% of noise.

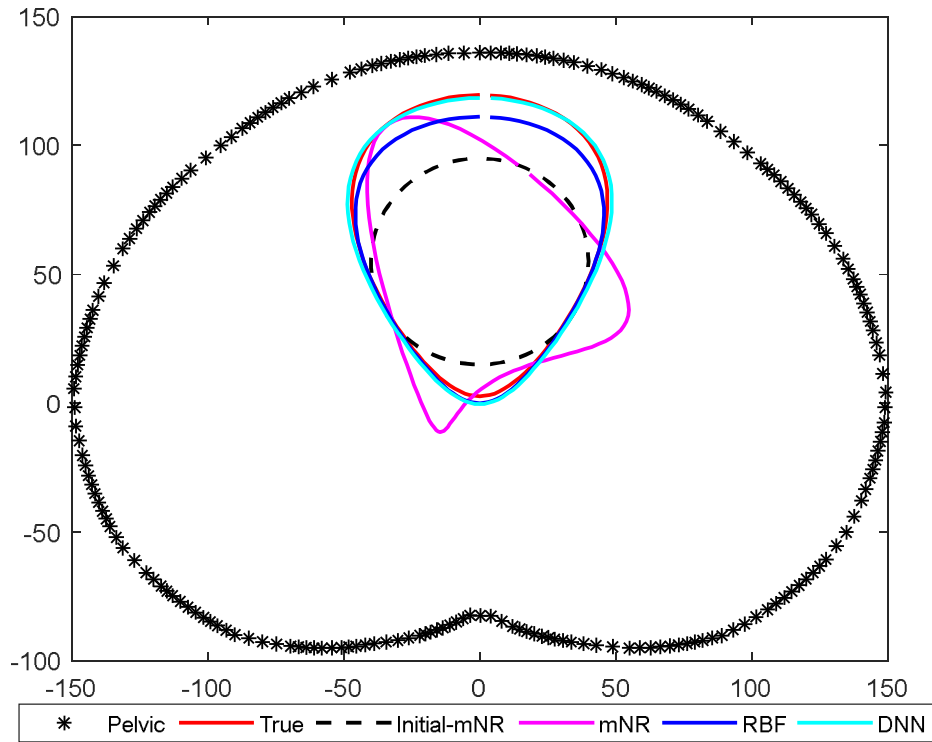


**Figure 5.7. Reconstructed image for a full size bladder in pelvic domain bladder case with 2% relative noise. Asterisk marked line represents pelvic domain boundary, and the red line is true bladder boundary, the dashed line is initial guess of mNR, Magenta line is with mNR method, blue line is with RBF method, and cyan line is using DNN method.**

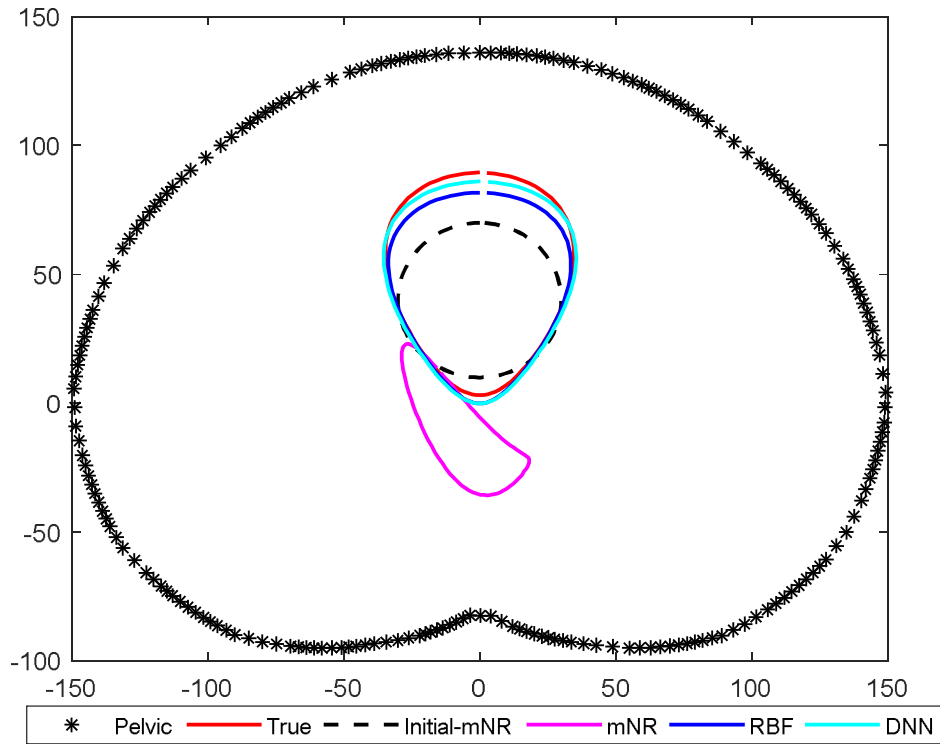


**Figure 5.8.** Reconstructed image for a medium size bladder in pelvic domain bladder case with 2% relative noise. Asterisk marked line represents pelvic domain boundary, and the red line is true bladder boundary, the dashed line is initial guess of mNR, Magenta line is with mNR method, blue line is with RBF method, and cyan line is using DNN method.

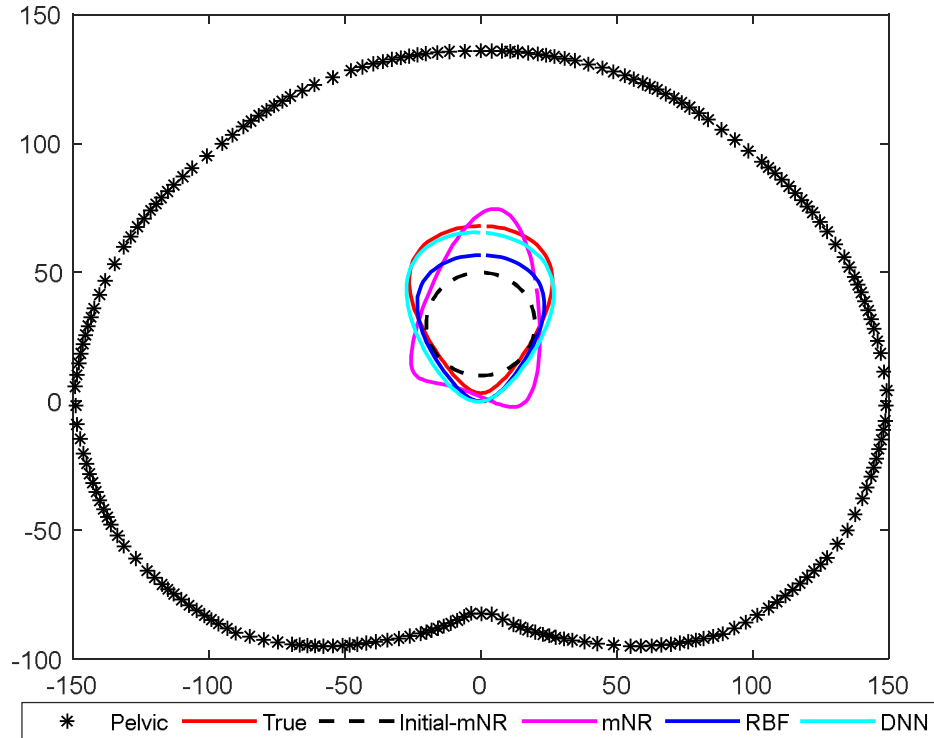


**Figure 5.9. Reconstructed image for a small size bladder in pelvic domain bladder case with 2% relative noise. Asterisk marked line represents pelvic domain boundary, and the red line is true bladder boundary, the dashed line is initial guess of mNR, Magenta line is with mNR method, blue line is with RBF method, and cyan line is using DNN method.**

We have computed the RMSE for estimated bladder boundary coefficients and estimated area of the bladder by using the three algorithms. Table 5.3 and 5.4 shows the corresponding RMSE for bladder boundary coefficients and the estimated area for simulation models for 2% noise case. The results in table 5.3, 5.4 prove that the estimated results obtained by the proposed DNN algorithm have the smallest RMSE for bladder boundary coefficients and estimated area values are closed to true values, which clearly illustrate the boundary estimation of bladder in DNN reconstruction image is more accurate.

**Table 5.3. RMSE for estimated bladder boundary coefficients for three simulation cases with 2% relative noise.**

Algorithm	Full size bladder case	Medium size bladder	Small size bladder
mNR	0.4876	0.5099	0.5982
RBF	0.0672	0.2532	0.0980
DNN	0.0272	0.0383	0.0864

**Table 5.4. True and estimated area of bladder boundary for three simulation test cases with 2% relative noise.**

Algorithm	Full size bladder case	Medium size bladder	Small size bladder
True area	81.6432	44.9209	24.7676
mNR	68.2662	35.5276	18.8382
RBF	74.8035	26.6140	22.7573
DNN	84.6380	46.5979	23.2047

### **5.3.1.2 Numerical results for bladder shaped target surrounded by three neighboring tissues inside the pelvic domain.**

In this section, the DNN model was designed to estimate the boundary of bladder shaped target surrounded by three other neighboring tissues such as Rectum, Gluteus Maximus muscle and Medius muscle are placed inside the pelvic domain. As we explained in previous section, the same pelvic shaped finite element mesh of 3220 triangular elements and 1714 nodes was used to make the simulation data for training the second DNN model. Eight Fourier coefficients are required to approximate bladder shaped target, six coefficients for rectum shaped target, ten coefficients for maximus muscle and ten coefficients for medius muscle inside the pelvic shaped mesh. The electrical conductivities of background tissue, bladder rectum, maximus muscle, and medius muscle are considered as 0.0034 S/cm, 0.021 S/cm, 0.0012 S/cm, 0.0056 S/cm, and 0.0056 S/cm respectively. The contact impedance between the skin electrodes and pelvic domain is assumed as  $0.005 \Omega \text{ cm}^2$ . In this study, we have injected electrical currents of 1 mA magnitude through the 16 skin electrodes using an opposite injection approach. To train the model, we perform the training of the 5-layer DNN with the 500 pairs of the boundary voltage measurements of pelvic domain and the corresponding Fourier coefficients of internal bladder boundary. One training input means one set of 128 independent boundary voltage measurements are fed to input layer of 128 neurons and the corresponding 8 Fourier coefficients values to output layer of 8 neurons. The number of training epochs was 500, and the batch size was eight and training rate was 0.001 used in the training stage of the model.

Three simulations cases of bladder such as fully-filled (full size), half-filled (medium size) and almost empty (small size) were considered. In each simulation case, pelvic domain contains bladder shaped target and along with neighboring tissue shaped targets as shown in figures (5.10~5.12). Reconstructed results of mNR, RBF and DNN algorithm are displayed in the figures (5.10~5.12). We have noticed that DNN algorithm gives better estimation of bladder size and shape, when compared to mNR and RBF. Furthermore, the proposed DNN algorithm has better estimation even though bladder is surrounded by neighboring tissues.

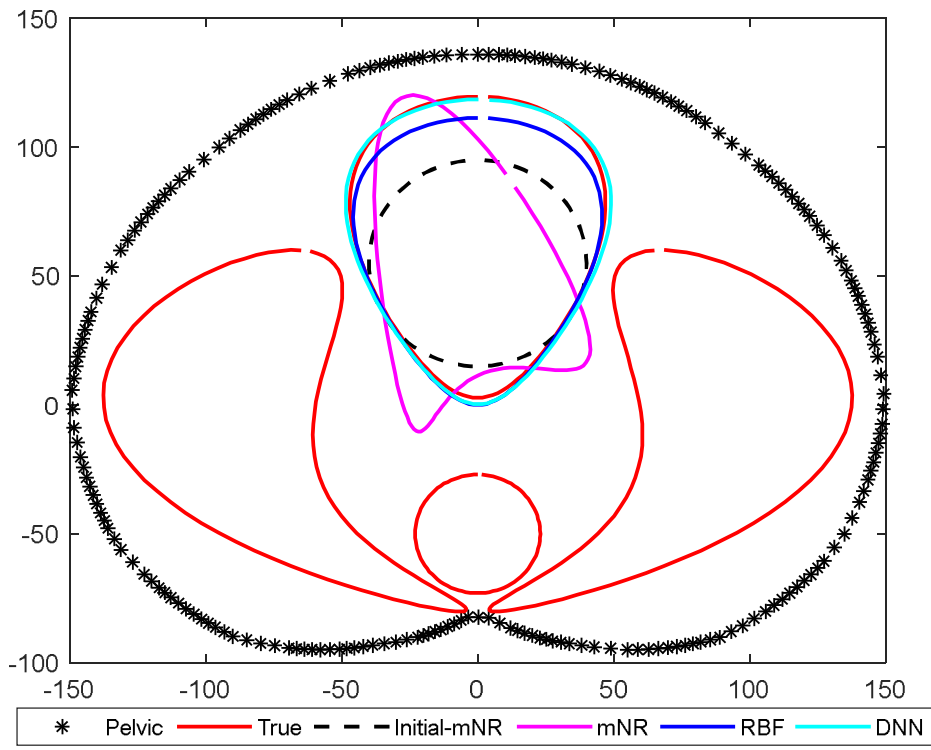


**Figure 5.10. Reconstructed image for full size bladder with neighboring tissue case. Asterisk marked line represents pelvic domain boundary, and the red line is true bladder boundary and neighboring tissues, the dashed line is initial guess of mNR, Magenta line is with mNR method, blue line is with RBF method, and cyan line is using DNN method.**

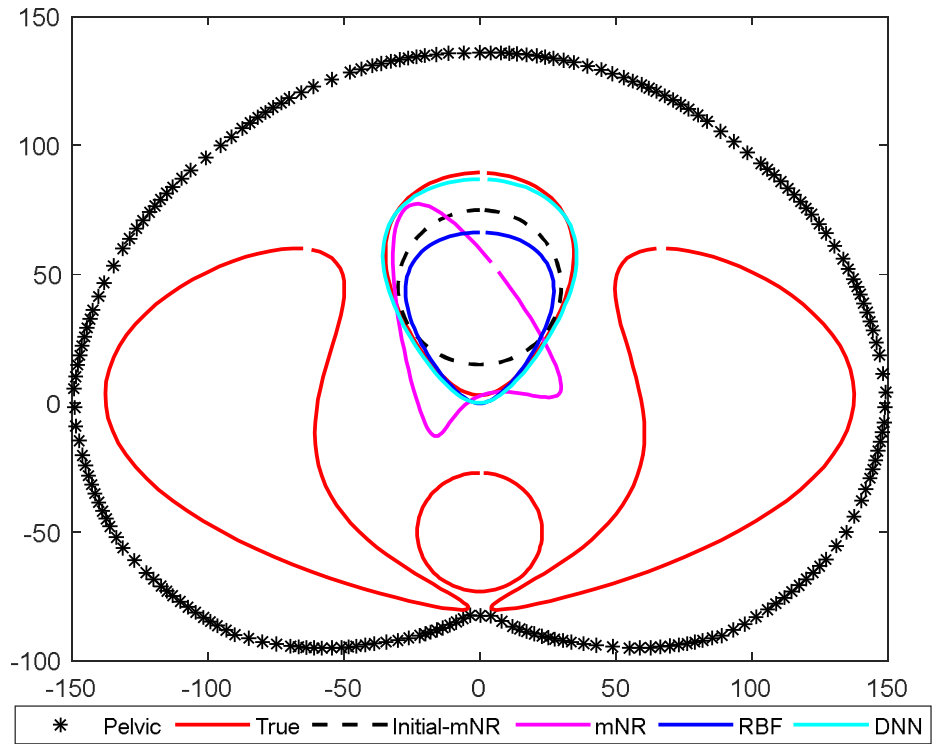


**Figure 5.11. Reconstructed image for medium size bladder with neighboring tissue. Asterisk marked line represents pelvic domain boundary, and the red line is true bladder boundary and neighboring tissues, the dashed line is initial guess of mNR, Magenta line is with mNR method, blue line is with RBF method, and cyan line is using DNN method.**

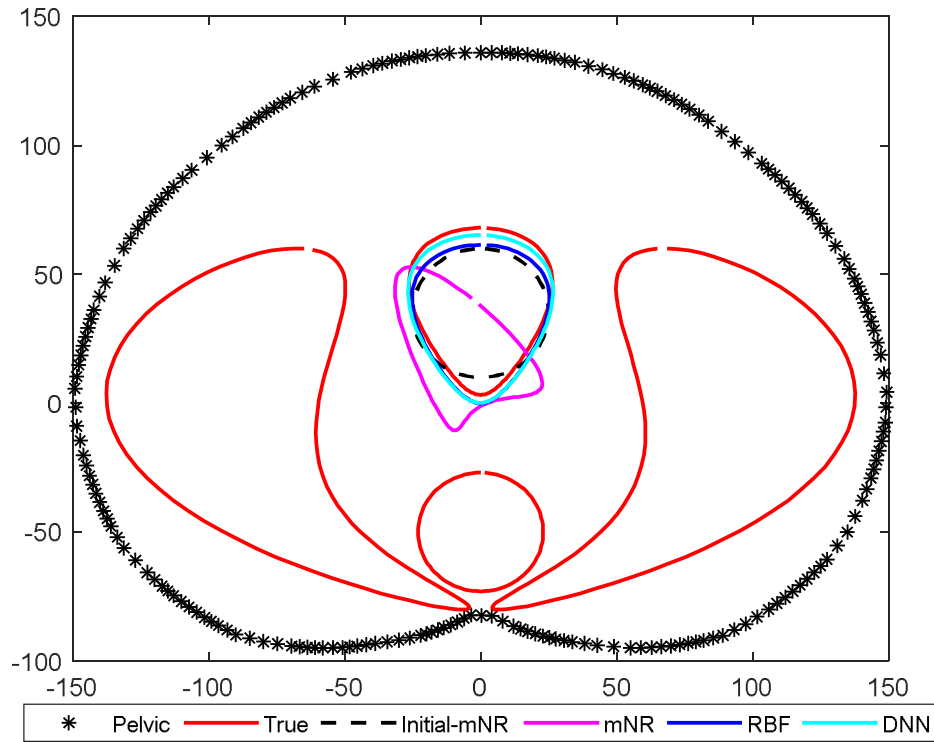


**Figure 5.12. Reconstructed image for small size bladder with neighboring tissue. Asterisk marked line represents pelvic domain boundary, and the red line is true bladder boundary and neighboring tissues, the dashed line is initial guess of mNR, Magenta line is with mNR method, blue line is with RBF method, and cyan line is using DNN method.**

To evaluate the stability and accuracy of proposed algorithms, we have computed RMSE for bladder boundary coefficients and estimated area of the bladder, as shown in the below tables (5.5 ~ 5.6). The better estimation performance of the DNN algorithm can be noticed in the RMSE for bladder boundary coefficients and estimated area where DNN is found to have less RMSE values for bladder boundary values than mNR and RBF.

**Table 5.5. RMSE for estimated bladder boundary coefficients for three simulation test cases**

Algorithm	Full size bladder	Medium size bladder	Small size bladder
mNR	0.4464	0.6218	0.8707
RBF	0.0642	0.0617	0.1720
DNN	0.0304	0.0481	0.0566

**Table 5.6. True and estimated area of bladder boundary for three simulation test cases**

Algorithm	Full size bladder	Medium size bladder	Small size bladder
True area	81.6432	44.9209	24.7676
mNR	72.2449	36.7392	5.7061
RBF	75.3398	43.0286	18.9175
DNN	83.3456	45.2097	25.9614

Besides, 2% relative noise is added to the boundary voltage measurements to depict practical conditions. Reconstructed results of bladder boundary surrounded by neighboring tissues with 2% noise using mNR, RBF and DNN algorithm are shown below in Figure (5.13~5.15). RMSE for bladder boundary coefficients and estimated area of the bladder, are shown below in tables (5.7 ~ 5.8). From Figure (5.13~5.15), we can clearly say that DNN algorithm demonstrates better estimation of the bladder boundary compared to mNR and RBF. Table (5.7 and 5.8) shows that lower RMSE bladder boundary coefficients and better estimation of size are recorded for DNN and as compared to mNR and RBF.

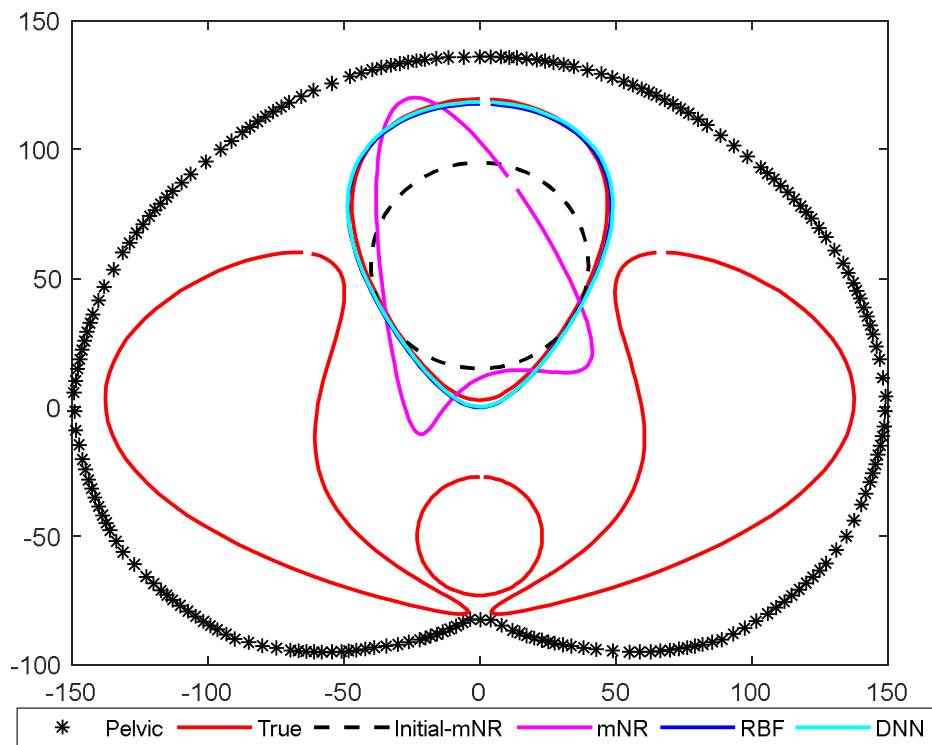


**Figure 5.13. Reconstructed image for full size bladder with neighboring tissue of 2% noise case. Asterisk marked line represents pelvic domain boundary, and the red line is true bladder boundary and adjacent tissues, the dashed line is initial guess of mNR, Magenta line is with mNR method, blue line is with RBF method, and cyan line is using DNN method.**

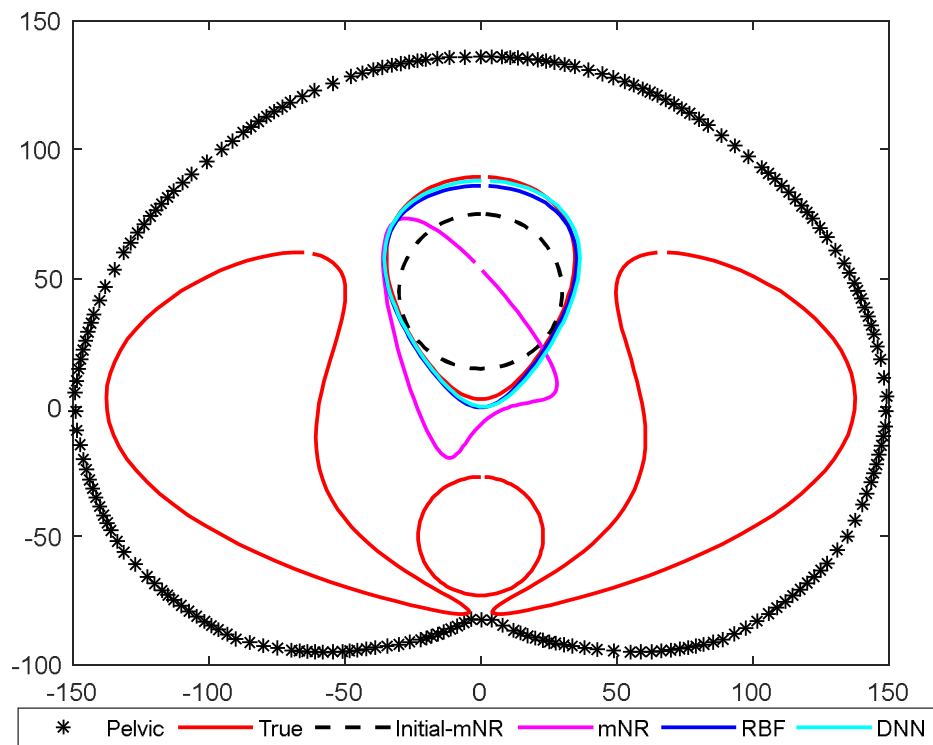


**Figure 5.14. Reconstructed image for medium size bladder with neighboring tissue of 2% noise case. Asterisk marked line represents pelvic domain boundary, and the red line is true bladder boundary and neighboring tissues, the dashed line is initial guess of mNR, Magenta line is with mNR method, blue line is with RBF method, and cyan is using DNN method.**

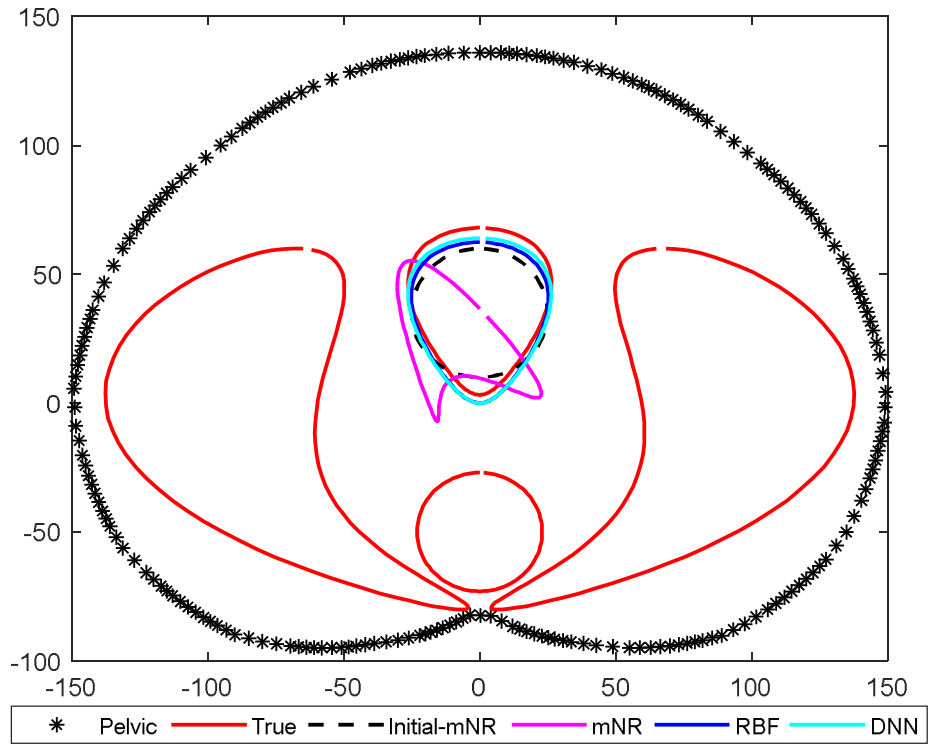


**Figure 5.15. Reconstructed image for small size bladder with neighboring tissue of 2% noise case. Asterisk marked line represents pelvic domain boundary, and the red line is true bladder boundary and neighboring tissues, the dashed line is initial guess of mNR, Magenta line is with mNR method, blue line is with RBF method, and cyan line is using DNN method.**

**Table 5.7. RMSE for estimated bladder boundary coefficients for three simulation test cases with 2% relative noise.**

Algorithm	Full size bladder	Medium size bladder	Small size bladder
mNR	0.3852	0.8927	0.8132
RBF	0.0682	0.0871	0.1604
DNN	0.0292	0.0502	0.0620

**Table 5.8. True and estimated area of bladder boundary for three simulation test cases with 2% relative noise.**

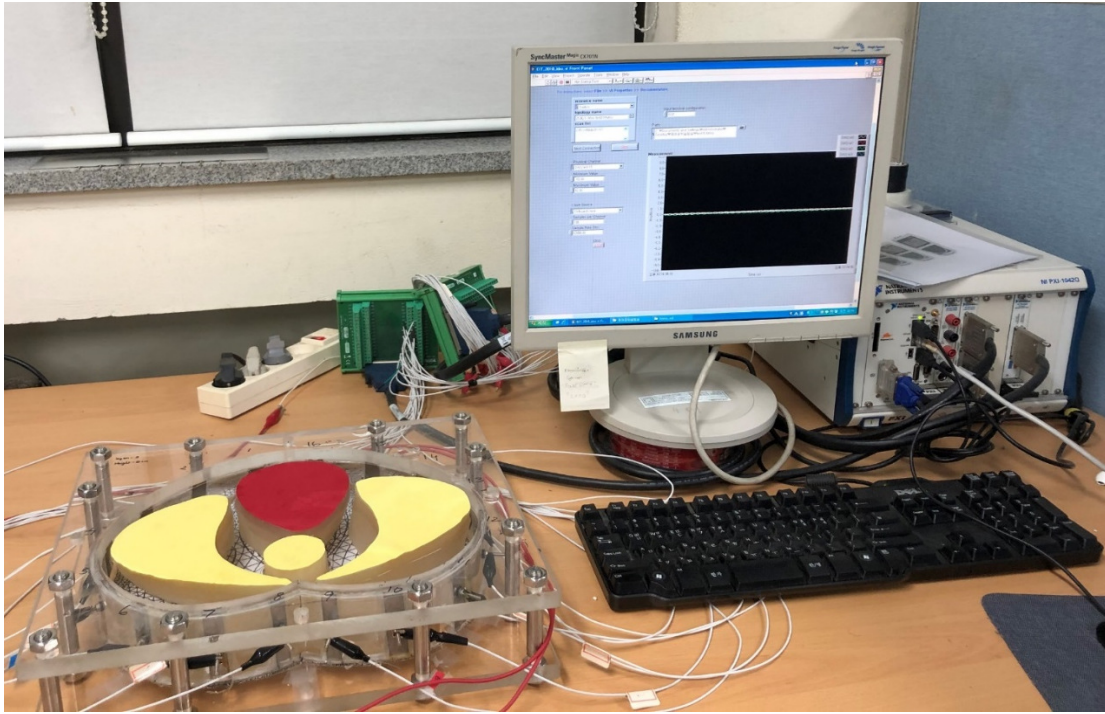
Algorithm	Full size bladder	Medium size bladder	Small size bladder
True area	81.6432	44.9209	24.7676
mNR	75.1024	12.5029	26.4608
RBF	74.6229	40.3103	19.4757
DNN	84.7118	44.8119	26.3699

### 5.3.2 Experimental studies with Pelvic shaped phantom

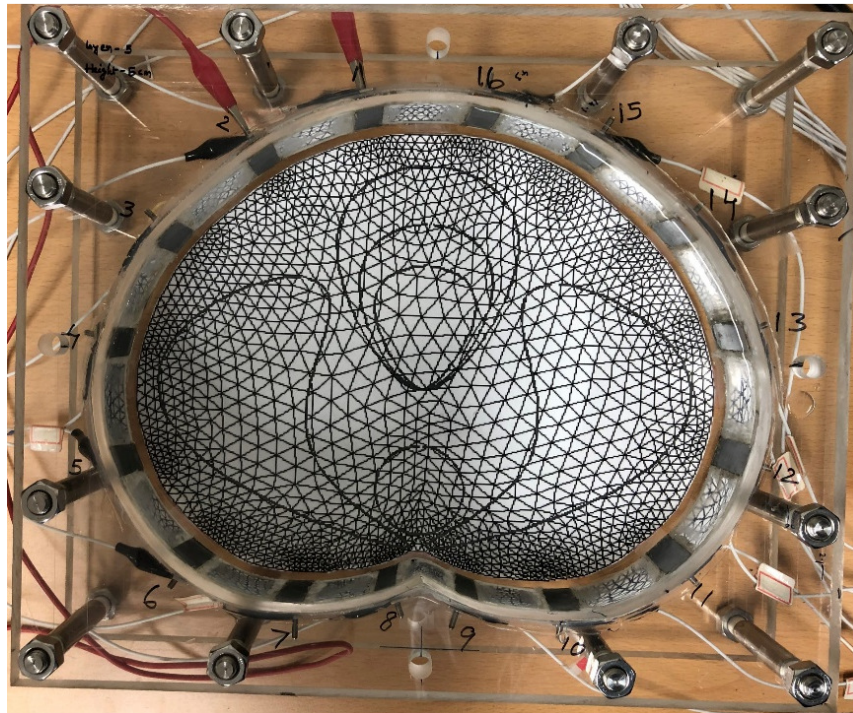
This section presents the visualization of bladder boundary estimation using the experimental pelvic phantom setup as shown in Figure 5.16. We have used same DNN simulation models, which were trained by 500 pairs simulation data of the boundary voltage measurements as input data and the corresponding Fourier coefficients of internal bladder boundary as output data, described in section 5.3.1.1 and 5.3.1.2.

To the evaluate the trained model with experimental test data, we employed EIT experimental system that consists of PC, an electrode switching module, a data acquisition system, an LCR meter, national instrument system (NI PXI-1042Q) and a pelvic shaped phantom of height (5cm) with 16 electrodes. We have performed two pelvic phantom experimental scenarios with three different sizes of bladder shaped targets, which were the same as the numerical simulation cases.

The first scenario was a pelvic phantom that contains only a bladder shaped target. Whereas another one was pelvic phantom of bladder shaped target surrounded by three neighboring tissue such are rectum, gluteus maximus muscle, and medius muscle.



(a)



(b)

**Figure 5.16. EIT experimental system used for visualization of bladder boundary (a) experimental setup (b) pelvic shaped phantom used for experiments.**

### 5.3.2.1 EIT experiment with pelvic phantom of single bladder shaped target

The pelvic shaped phantom is filled with a saline solution having conductivity of approximately (0.0025 S/cm) up to the electrode height, therefore the generated imaging results can be considered as a two-dimensional imaging system. Three different sizes of bladder shaped targets are prepared with tissue mimicking materials such as gelatine solution having conductivity of approximately (0.020 S/cm). In each experimental case, the bladder shaped target is placed in different locations of pelvic phantom. Opposite current patterns were employed as current injection method, and the currents with magnitude 1 mA are injected through the 16 skin electrodes.

To generate the test data, fully-filled, half-filled and empty bladder experimental cases were carried out. Therefore, pelvic shaped phantom contains a bladder shaped target in each case, as shown in Figure (5.17~5.19).

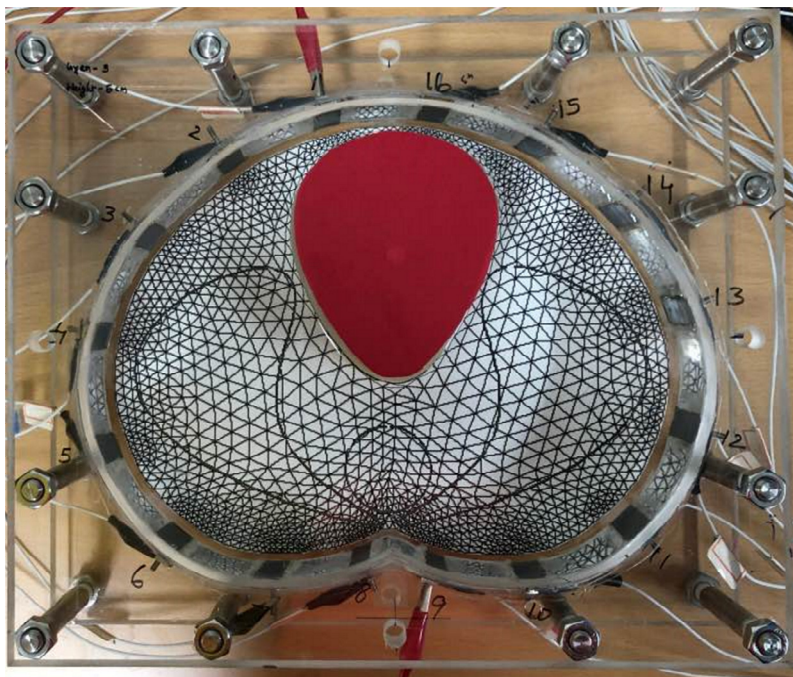
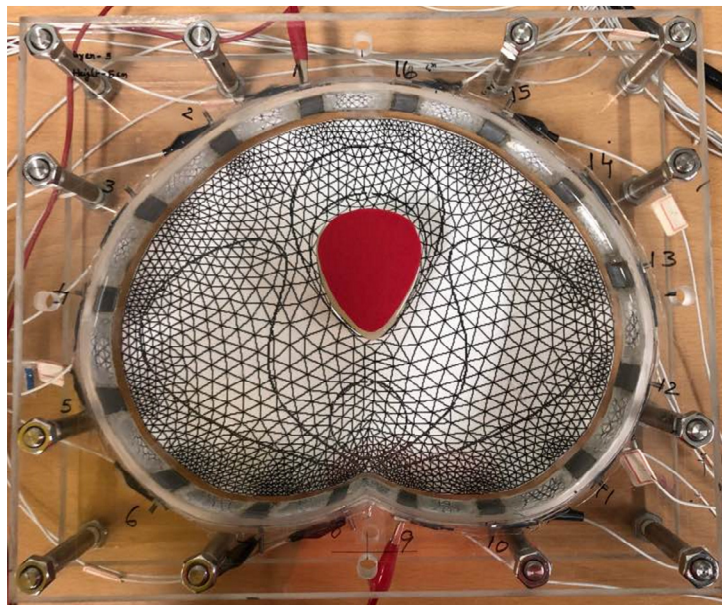


Figure 5.17. EIT experimental system of pelvic domain with full size bladder case.



**Figure 5.18. EIT experimental system of pelvic domain with medium size bladder case.**



**Figure 5.19. EIT experimental system of pelvic domain with small size bladder case.**

The reconstructed results of the bladder boundary with experimental data are shown in Figure 5.20~ 5.22. The reconstructed results illustrate that a simulated trained DNN model can obtain

good bladder boundary estimation with phantom experimental data. Besides, we can notice that DNN algorithm gives better estimation of bladder size and shape when compared to mNR and RBF.

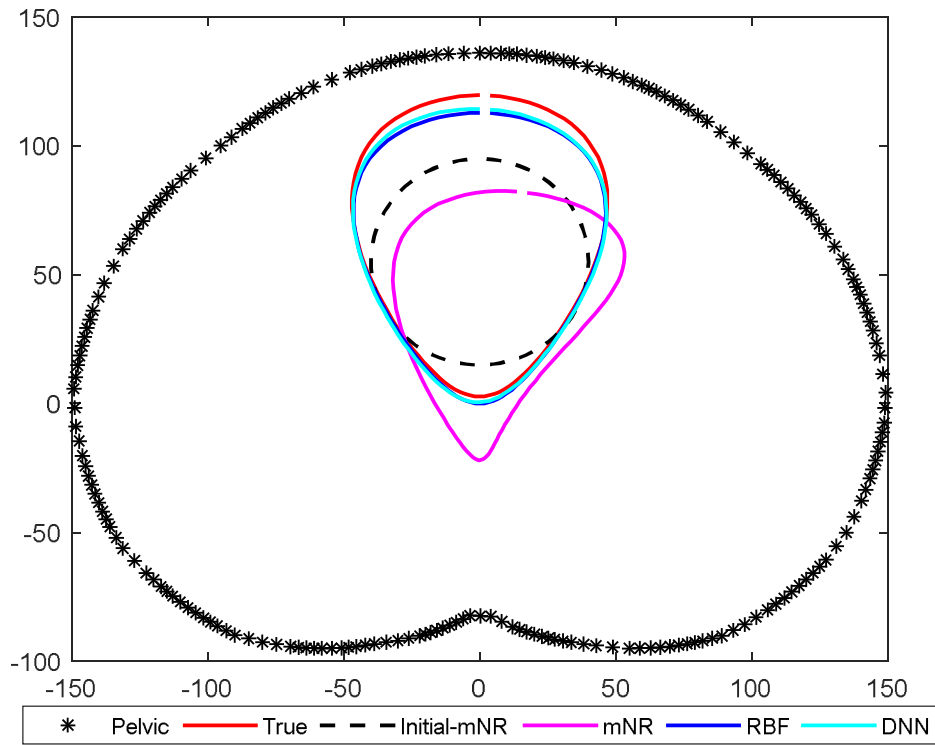


**Figure 5.20. Bladder boundary estimation results for a full size bladder experimental case. Asterisk marked line represents pelvic domain boundary, the red line is true bladder boundary and neighboring tissues, dashed line is initial guess of mNR, Magenta line is with mNR method, blue line is with RBF method, and cyan line is using DNN method.**

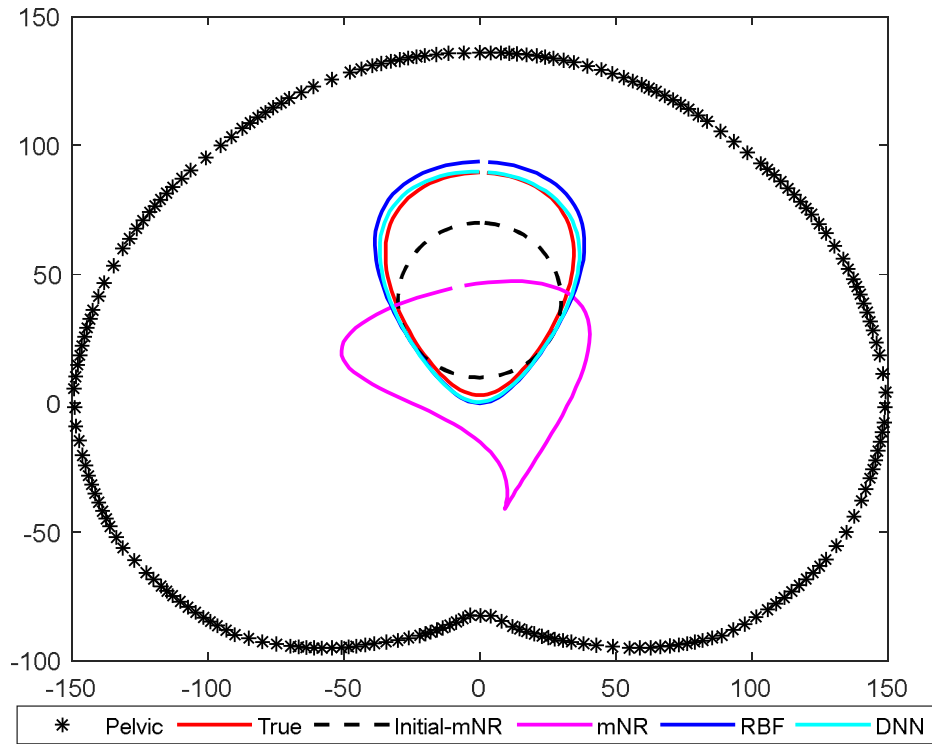


**Figure 5.21. Bladder boundary estimation results for medium size bladder experimental case. Asterisk marked line represents pelvic domain boundary, the red line is true bladder boundary and neighboring tissues, the dashed line is initial guess of mNR, Magenta line is with mNR method, blue line is with RBF method, and cyan line is using DNN method.**

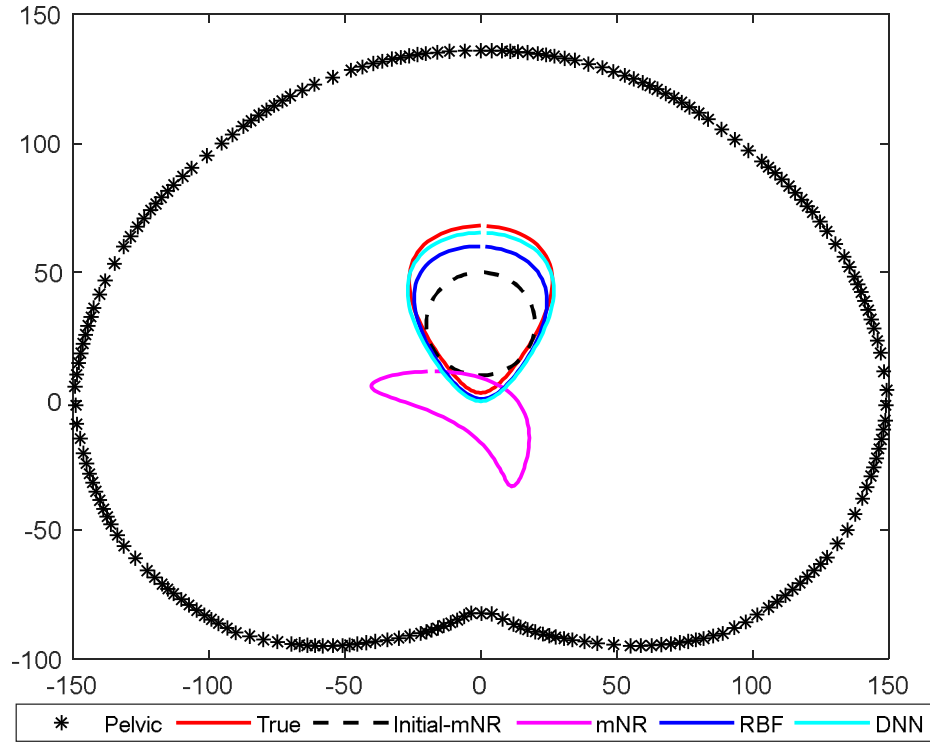


**Figure 5.22. Bladder boundary estimation results for small size bladder experimental case. Asterisk marked line represents pelvic domain boundary, the red line is true bladder boundary and neighboring tissues, the dashed line is initial guess of mNR, Magenta line is with mNR method, blue line is with RBF method, and cyan line is using DNN method.**

RMSE for bladder boundary coefficients and estimated area of the bladder by the mNR, RBF and DNN algorithms, as displayed in table (5.9 and 5.10). The results in the table (5.9 and 5.10) demonstrates that the DNN algorithm gives the best estimation results. A comparison of the simulated and experimental voltage measurements is shown in figure (5.23~5.25) and calculated RMSE ( $RMSE_{Voltage}$ ) for voltage measurements are shown in table 5.11 and formulated as

$$\begin{aligned}
 RMSE_{Voltage} &= \sqrt{\frac{(V_{calculated} - V_{measured})^T (V_{calculated} - V_{measured})}{V_{calculated} \cdot V_{calculated}}} \\
 &= \sqrt{\frac{[V(\gamma) - U]^T [V(\gamma) - U]}{[V(\gamma) \cdot U]}}
 \end{aligned}$$

**Table 5.9. RMSE for estimated bladder boundary coefficients of three experimental cases using mNR, RBF and DNN.**

Case	RMSE for estimated Fourier coefficients		
	mNR	RBF	DNN
Experimental case1 (full size)	0.4049	0.0516	0.0353
Experimental case2 (medium size)	0.7623	0.1286	0.0789
Experimental case3 (small size)	0.7680	0.1397	0.1039

**Table 5.10. True and estimated area of bladder boundary for three experimental cases using mNR, RBF and DNN.**

Case	True and estimated bladder area (square cm)			
	True	mNR	RBF	DNN
Experimental case1 (full size)	81.6432	73.4400	77.6442	79.6196
Experimental case2 (medium size)	44.9209	50.1346	36.4769	40.6677
Experimental case3 (small size)	24.7676	17.6221	20.5023	21.9564

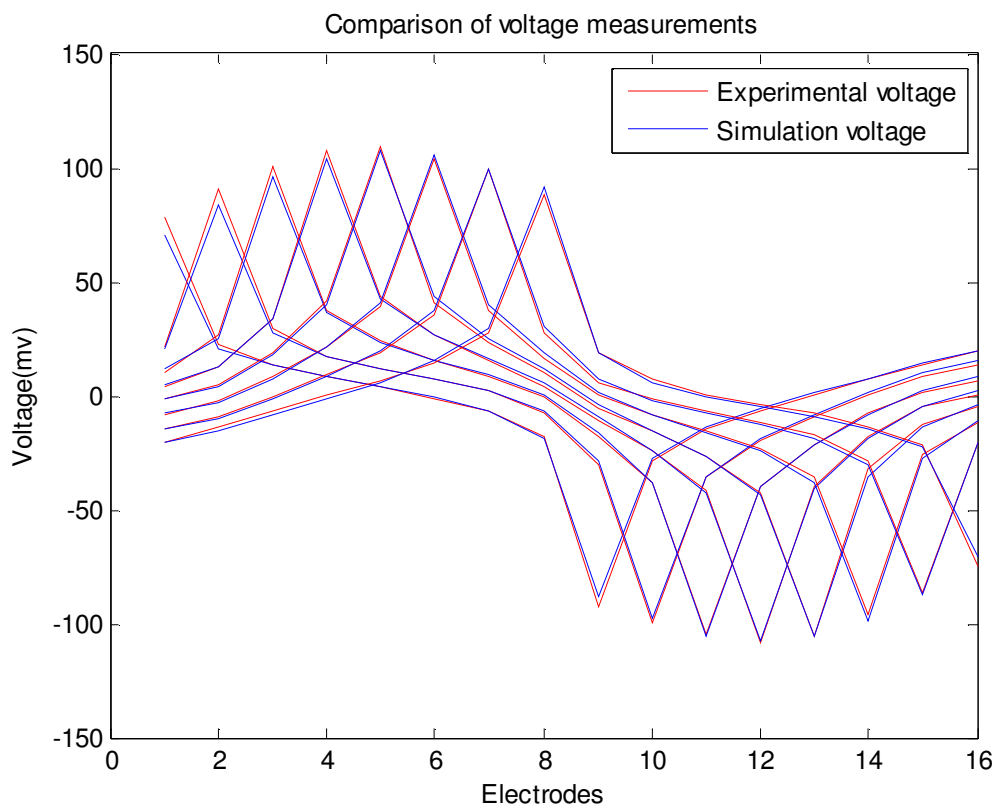


**Figure 5.23. Comparison of the simulated and experimental voltage measurements for full size bladder inside the pelvic domain (case 1).**

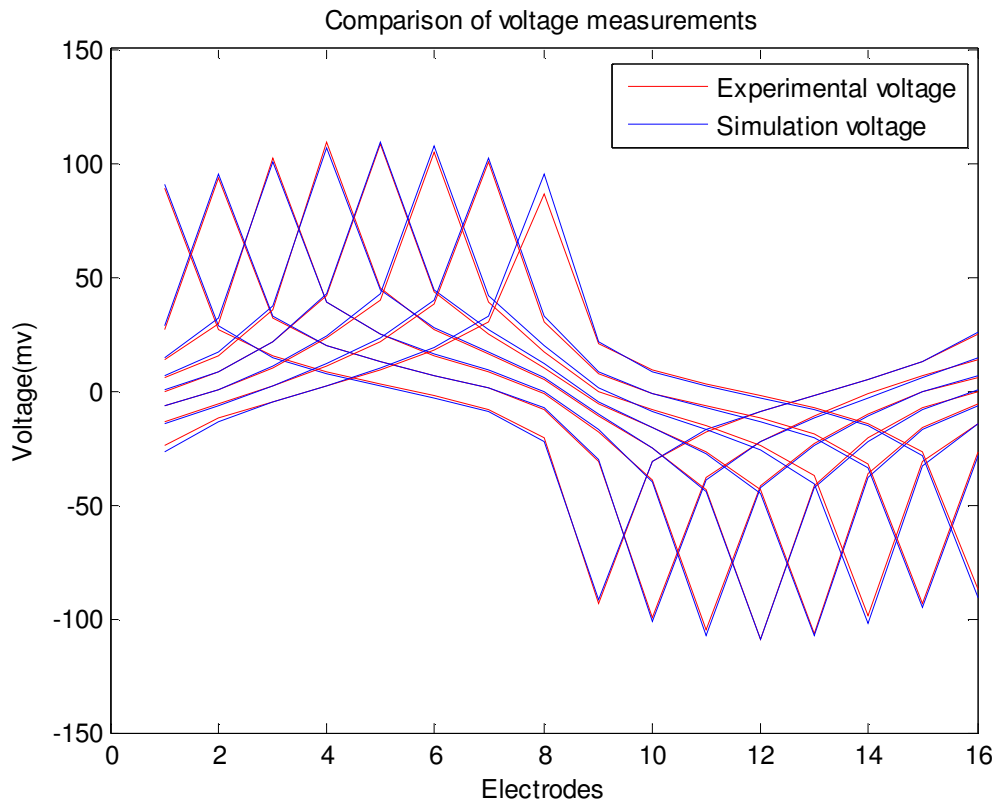


**Figure 5.24. Comparison of the simulated and experimental voltage measurements for medium size bladder inside the pelvic domain (case 2).**

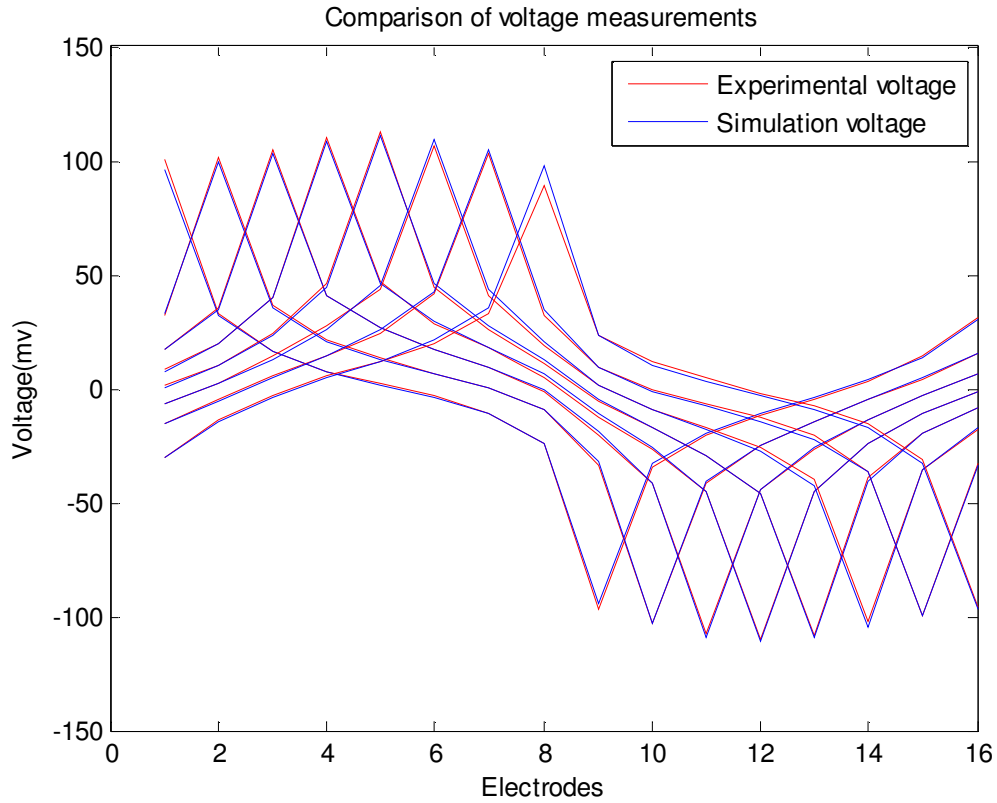


**Figure 5.25. Comparison of the simulated and experimental voltage measurements for small size bladder inside the pelvic domain (case 3).**

**Table 5.11. RMSE of voltage measurements for three experimental cases**

Case	RMSE for voltage measurements
Experimental case1 (full size)	0.0576
Experimental case2 (medium size)	0.0817
Experimental case3 (small size)	0.0658

### **5.3.2.2 EIT experimental results for bladder size estimation with pelvic phantom consisting of bladder surrounded by three neighboring tissues.**

This section demonstrated a second experimental scenario with pelvic phantom of bladder shaped target surrounded by three neighboring tissue shaped targets such are rectum, gluteus maximus muscle, and medius muscle. The pelvic shaped phantom is filled with a saline solution having conductivity of approximately (0.0034 S/cm) up to the electrode height. Bladder shaped target and neighboring tissue shaped targets are prepared with gelatine solution having conductivity of about 0.021 S/cm, 0.0012 S/cm, 0.0056 S/cm, and 0.0056 S/cm, respectively.

To generate the test data, we carried out three experimental cases that are fully-filled, half-filled, and empty bladder. Therefore, pelvic shaped phantom contains bladder shaped target and surrounded by three neighboring tissue shaped targets in each case, as shown in Figure (5.26~5.28).

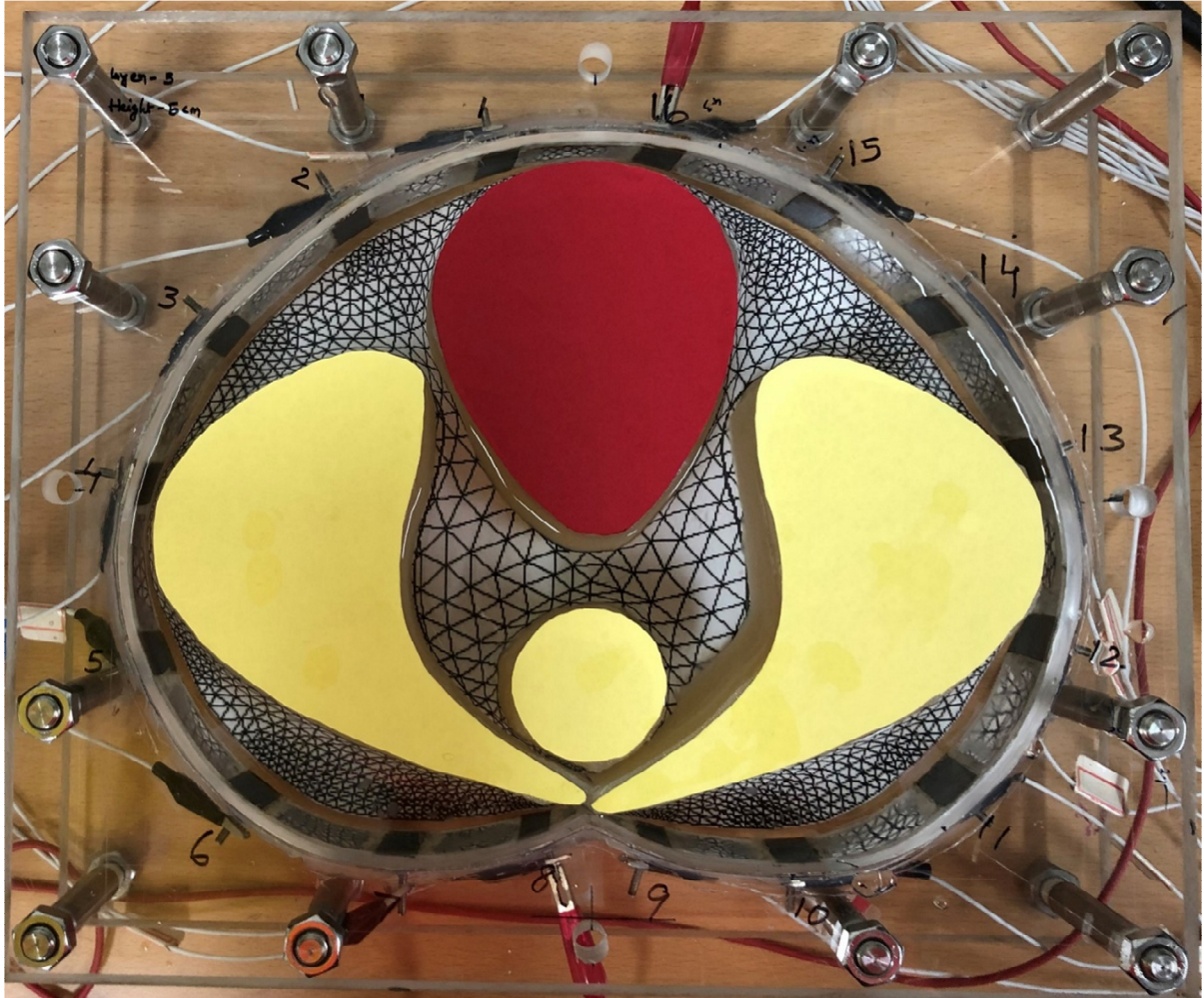


**Figure 5.26. EIT experimental system of pelvic domain with full size bladder (surrounded by three neighboring tissue shaped targets) case.**

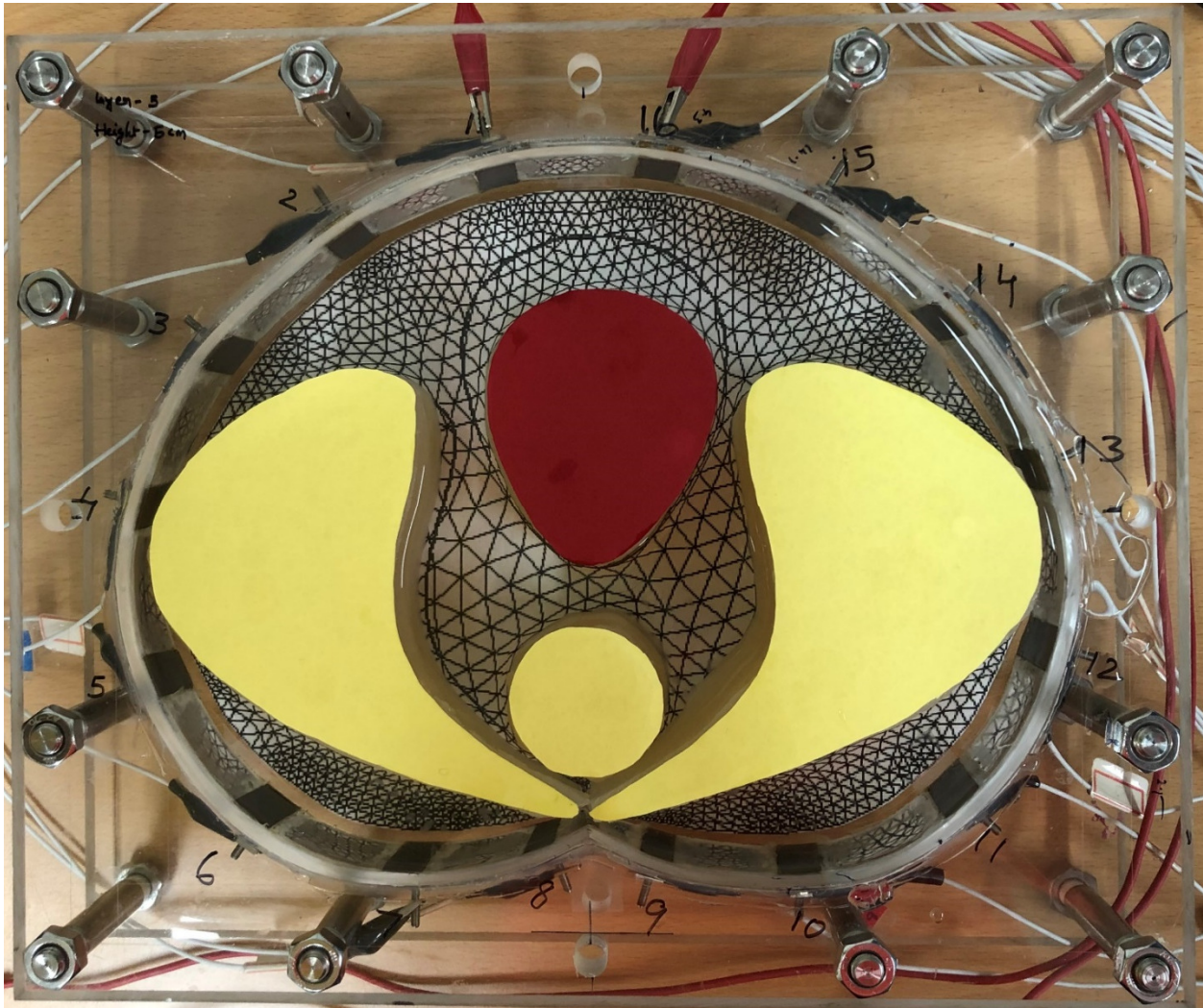


**Figure 5.27. EIT experimental system of pelvic domain with medium size bladder (surrounded by three neighboring tissue shaped targets) case.**

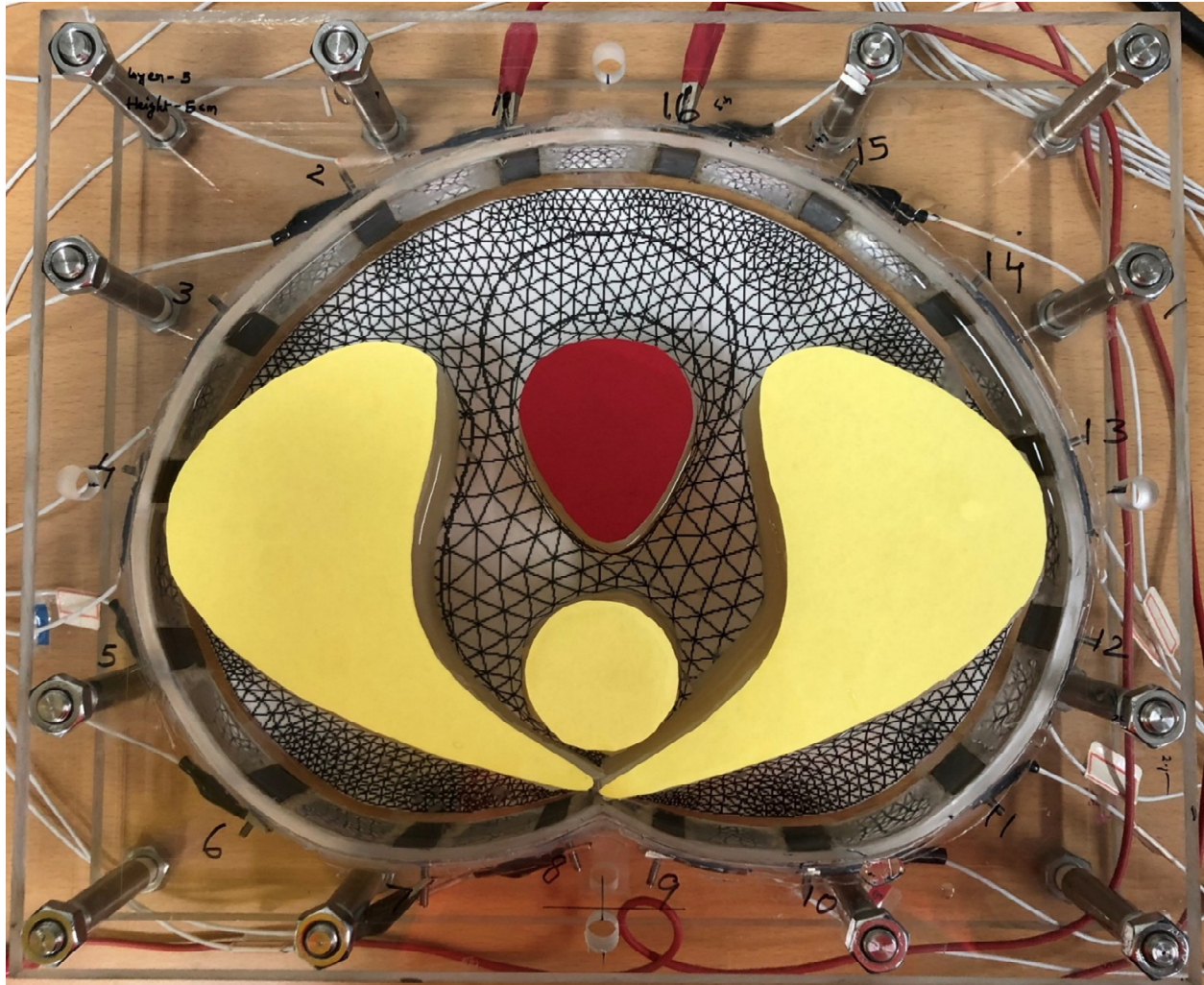


**Figure 5.28. EIT experimental system of pelvic domain with small size bladder (surrounded by three neighboring tissue shaped targets) case.**

The reconstructed results of the bladder boundary with experimental data are shown in Figure 5.29~ 5.31 and reconstructed results illustrate that the simulated trained DNN model can obtain good bladder boundary estimation with phantom experimental data. Besides, we can notice that DNN algorithm has better estimation of bladder size and shape when compared to mNR and RBF. RMSE for bladder boundary coefficients and estimated area of the bladder by the mNR, RBF and DNN algorithms, is displayed in table (5.12 and 5.13). From the table (5.12 and 5.13), the results demonstrate that the DNN algorithm has best estimation performance for bladder size and shape estimation. A comparison of the simulated and experimental voltage measurements are shown in

figure (5.32 ~5.34) and computed RMSE for voltage measurement values are reported in table (5.14).

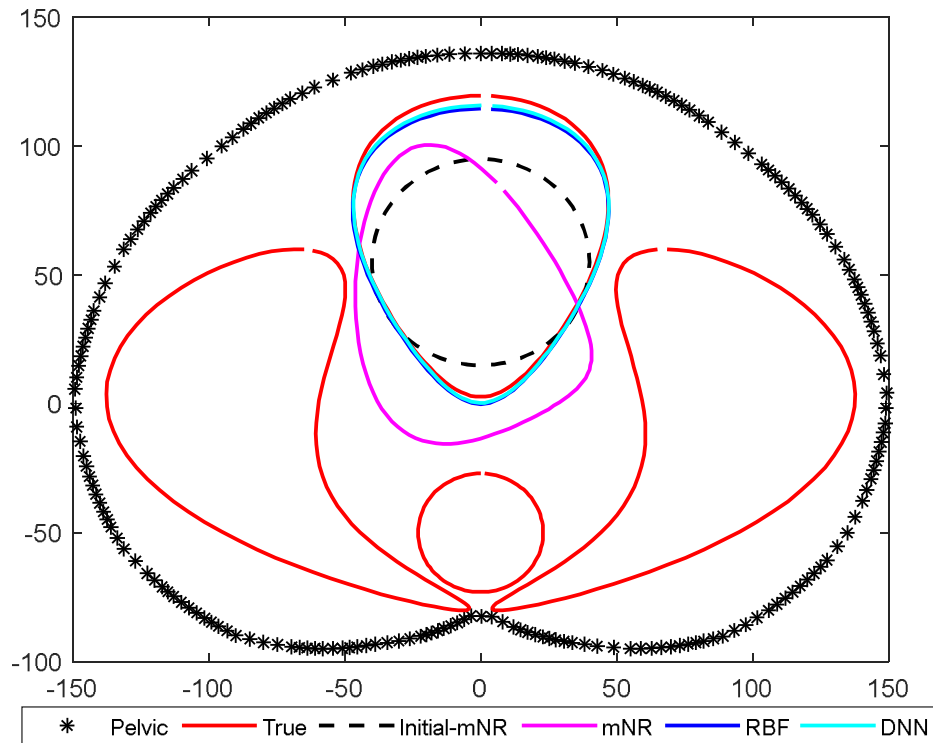


**Figure 5.29. Bladder boundary estimation results for full size bladder (surrounded by three neighboring tissue shaped targets) experimental case. Asterisk marked line represents pelvic domain boundary, the red line is true bladder boundary and neighboring tissues, the dashed line is initial guess of mNR, Magenta line is with mNR method, blue line is with RBF method, and cyan line is using DNN method.**

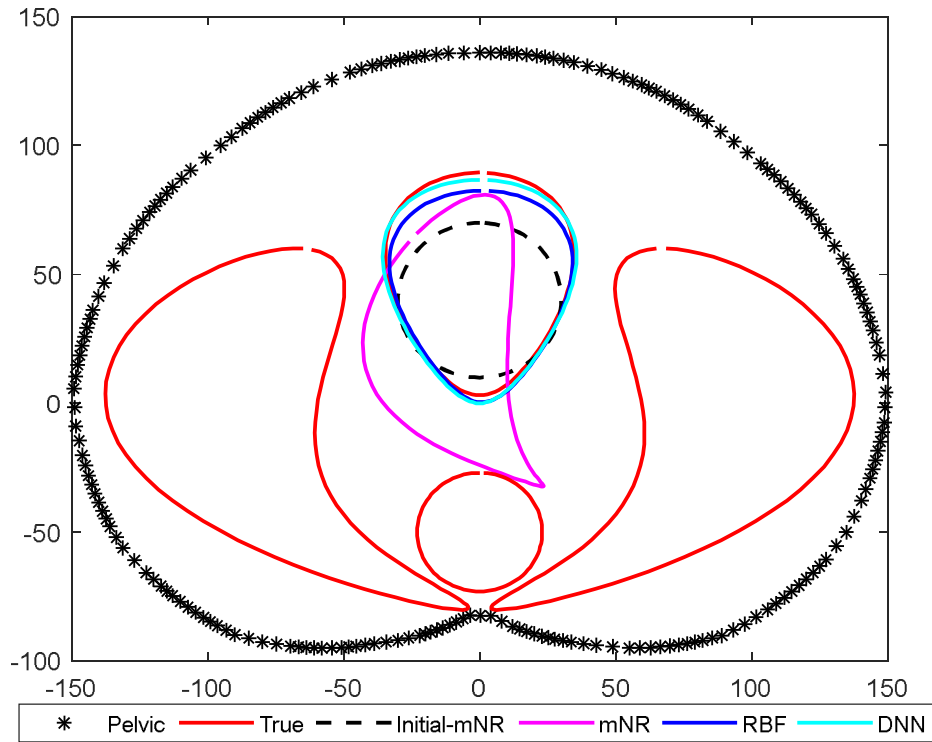


**Figure 5.30. Bladder boundary estimation results for medium size bladder (surrounded by three neighboring tissue shaped targets) experimental case. Asterisk marked line represents pelvic domain boundary, the red line is true bladder boundary and neighboring tissues, the dashed line is initial guess of mNR, Magenta line is with mNR method, blue line is with RBF method, and cyan line is using DNN method.**

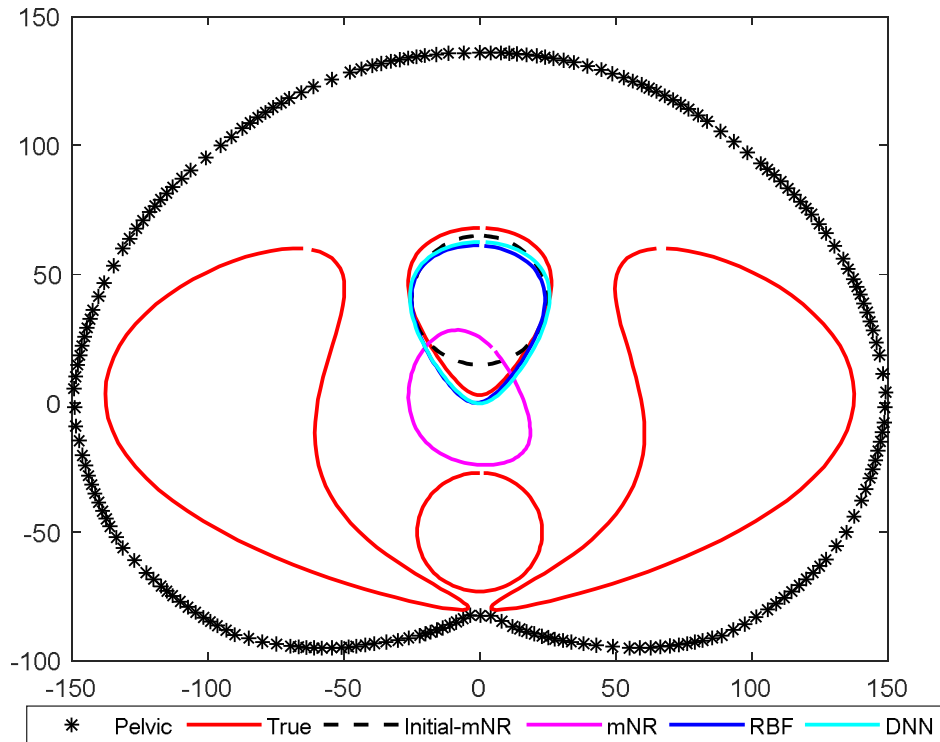


**Figure 5.31. Bladder boundary estimation results for small size bladder (surrounded by three neighboring tissue shaped targets) experimental case. Asterisk marked line represents pelvic domain boundary, and the red line is true bladder boundary and neighboring tissues, the dashed line is initial guess of mNR, Magenta line is with mNR method, blue line is with RBF method, and cyan is using DNN method.**

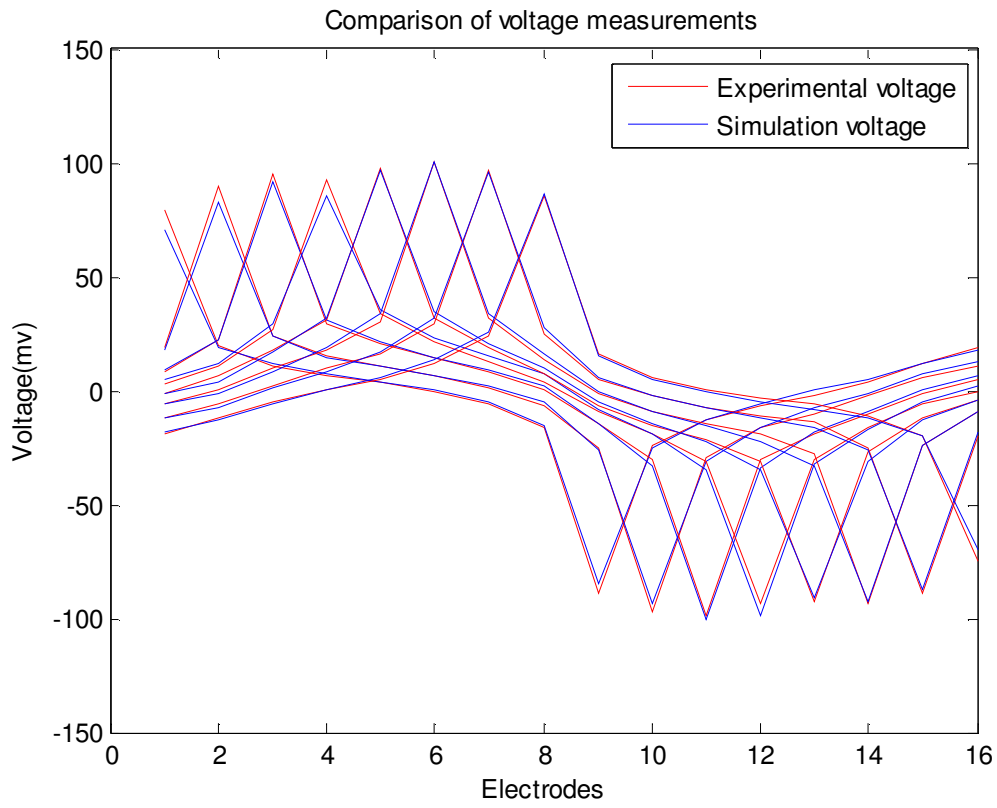


**Figure 5.32. Comparison of the simulated and experimental voltage measurements for full size bladder (case 1).**

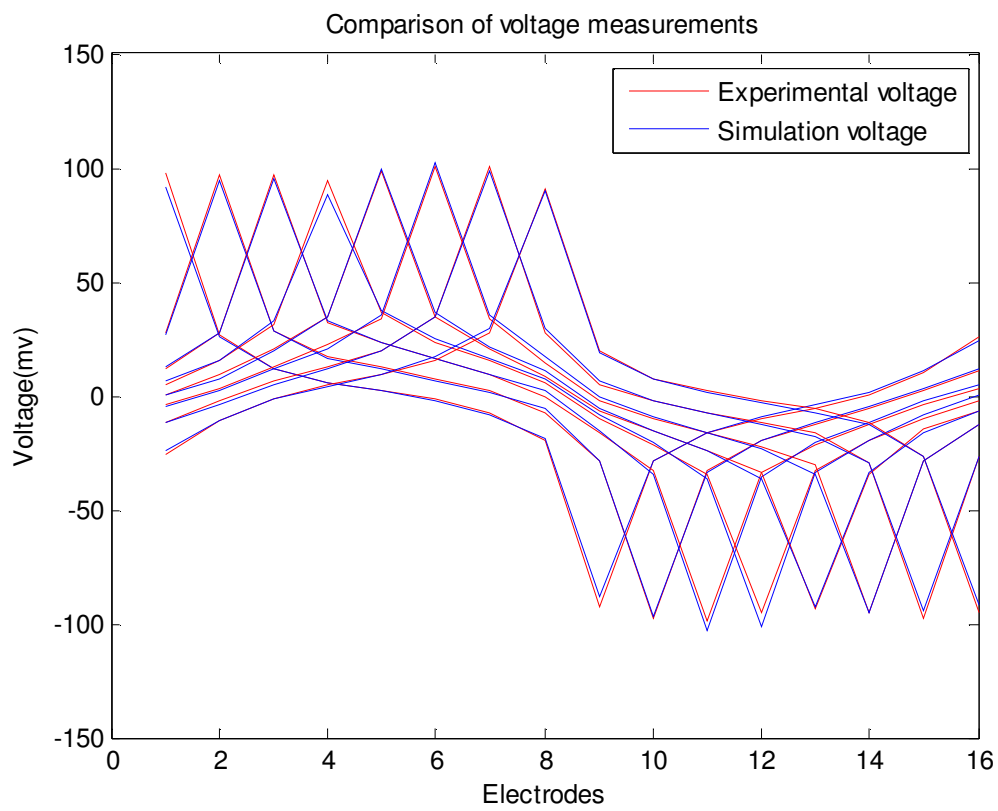


**Figure 5.33. Comparison of the simulated and experimental voltage measurements for medium size bladder (case 2).**

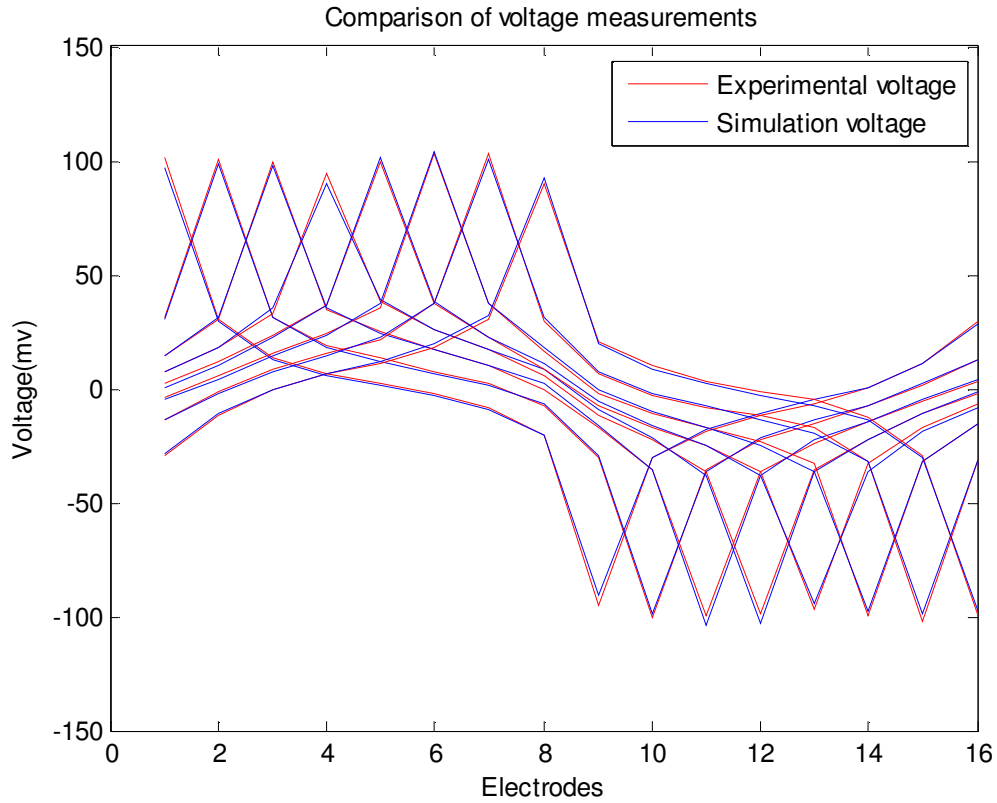


**Figure 5.34. Comparison of the simulated and experimental voltage measurements for small size bladder (case 3).**

**Table 5.12. RMSE for estimated bladder boundary coefficients of three experimental cases using mNR, RBF and DNN.**

Case	RMSE values of estimated Fourier coefficients		
	mNR	RBF	DNN
Experimental case1 (full size)	0.3616	0.0492	0.0433
Experimental case2 (medium size)	0.6515	0.2399	0.0378
Experimental case3 (small size)	0.8993	0.1485	0.1139

**Table 5.13. True and estimated area of bladder boundary for three experimental cases using mNR, RBF and DNN.**

Case	True and estimated bladder area (square cm)			
	True	mNR	RBF	DNN
Experimental case1 (full size)	81.6432	57.7256	78.1179	78.6101
Experimental case2 (medium size)	44.9209	49.1852	72.3841	48.6707
Experimental case3 (small size)	24.7676	13.8480	20.0607	21.3847

**Table 5.14. RMSE of voltage measurements for three experimental cases.**

Case	RMSE for voltage measurements
Experimental case1 (full size)	0.0536
Experimental case2 (medium size)	0.0360
Experimental case3 (small size)	0.0360

## 5.4 Discussion

This chapter analyses the application of the DNN algorithm to EIT in estimating the urinary bladder shape, size, and location inside the pelvic domain. Numerical simulations are carried out with and without noise and we observed that DNN was able to reconstruct the bladder boundary even in the presence of noise cases. Pelvic phantom experiments with single and multi-targets have been performed to verify the applicability and robustness of proposed algorithm.

Moreover, Numerical simulation and pelvic phantom experimental reconstruction results have shown that proposed deep neural network algorithm of a trained model with simulation dataset not only used for reconstruction of numerical simulation data but also can be employed to get reconstruction results of pelvic phantom experimental data and it has potential to offer accurate bladder boundary estimation.

## 6 . Conclusions

EIT image has a lower spatial resolution due to ill-posedness and makes it difficult to reconstruct the boundaries of regions inside the object. In the clinical applications, boundary estimation of the organ can provide additional clinical information to diagnosis human health. As a result, here we show interest in the boundary estimation of the organ rather than the inner conductivity distribution of the human body. However, the performance of the conventional inverse algorithms for estimation of organ boundaries using EIT is often sub-optimal. Several factors contribute to this poor performance including high sensitivity of EIT to the measurement noise, the rounding-off errors, the inherent ill-posed nature of the problem. Moreover, the performance of many of these boundary estimation techniques heavily depends on the selection of initial guess as well as the accurate computation of a Jacobian matrix. Therefore, all these conventional methods often fail to provide significant results in clinical environments. Considering these facts, the most critical aspect of introducing the inverse algorithm is the improvement in the accuracy of region boundaries. A novel, efficient inverse algorithm is required to solve the above mentioned challenges.

This study describes a deep neural network frame work to estimate urinary bladder boundary inside the pelvic domain using EIT. The urinary bladder and neighboring tissue boundaries inside the pelvic region are approximated by the truncated Fourier series approach. Since the electrical conductivity values of background tissue, bladder, and adjacent tissues inside the pelvic domain are known a priori. In this thesis, two deep neural network models were designed to estimate the bladder boundary. Firstly, a 5-layer DNN model is intended to estimate the boundary of a single bladder shaped target inside the pelvic domain and trained with pairs of the boundary voltage measurements of pelvic area as input data and the corresponding Fourier coefficients of internal bladder boundary as output data. Whereas the second 5-layer DNN model is designed to estimate boundary of bladder shaped targets surrounded by three other neighboring tissues placed inside the pelvic domain. We have evaluated proposed the DNN model with simulated test data, with 2 % measurement noise and also with experimental test data. The results demonstrate that DNN algorithm has significantly better estimation performance as compared to the traditional algorithms, in the both cases such as bladder shaped target inside the pelvic domain and bladder shaped targets

surrounded by three other neighboring tissues. A statistical analysis of the estimated Fourier coefficients and area of bladder using DNN algorithm has been presented and performance of DNN is compared with modified Newton-Raphson and RBF-NN. It can be noticed that proposed DNN algorithm is accurate in estimating the bladder boundary and has very low RMSE for bladder boundary coefficients values and estimated areas close to true area as compared to mNR, RBF network.

The proposed DNN algorithm has advantages that, it is simple to implement, better accuracy and fast estimation. Furthermore, DNN technique does not require any initial guess and Jacobian matrix computations.

## Summary

Electrical Impedance Tomography (EIT) is a noninvasive imaging technology that aims to reconstruct the cross sectional image of internal conductivity distribution of electrically conducting objects such as human body or any domain. In the working principle of EIT, an array of electrodes are attached on the surface of the human body or object domain to inject an alternating current (AC) and measure the induced voltages on the electrodes, and the corresponding electrical conductivity information is estimated according to Ohm's law.

Reconstruction of the internal resistivity distribution using EIT is an ill-posed problem and highly non-linear. EIT image has a lower spatial resolution due to ill-posedness and makes it difficult to reconstruct the boundaries of regions inside the object. If the internal resistivity distribution values of the object can be known a priori, then the inverse problem in EIT becomes estimating the boundary, size, position of the regions inside the object. The approach to estimate region boundaries rather than internal resistivity distributions is known as boundary estimation in EIT. In the clinical applications, boundary estimation of the organ can provide additional clinical information to diagnosis human health. As a result, here we show interest in the boundary estimation of the organ rather than the inner conductivity distribution of the human body. However, the performance of the conventional inverse algorithms for estimation of organ boundaries using EIT is often sub-optimal.

To overcome this problem, a deep neural network algorithm is proposed to estimate urinary bladder boundary inside the pelvic domain using EIT. Two deep neural network models were considered and trained the model with pairs of the boundary voltage measurements of pelvic area as input data and the corresponding Fourier coefficients of internal bladder boundary as output data. First 5-layer DNN model is intended to estimate the boundary of a bladder shaped target inside the pelvic domain and trained with pairs of the boundary voltage measurements of pelvic area as input data and the corresponding Fourier coefficients of internal bladder boundary as output data. Whereas the second 5-layer DNN model is designed to estimate boundary of bladder shaped targets surrounded by three other neighboring tissue shaped targets placed inside the pelvic domain. The estimated results of simulations and phantom experiments show that DNN algorithm has significantly better estimation performance as compared to the traditional algorithms.

## References

- Anderson K D, Targeting recovery: priorities of the spinal cord-injured population. *J Neurotraum.* 21, 1371–83, 2004.
- Barber D C and Brown B H, Applied potential tomography *J Phys. E: Sci Instrum* 17, 723-733, 1984.
- Brenner S and Scott R, The Mathematical Theory of Finite Element Methods, *Springer-Verlag* New York, 1994.
- Brown B H, Barber D C, Morica A H and Leathard A D, Cardiac and respiratory related electric impedance changes in the human thorax, *IEEE Trans. Biomed. Eng.* 41 729-723, 1994.
- Cartwright D J, Underlying Principles of the Boundary Element Method, *Billerica, MA: Computational Mechanics*, 2001.
- Cheney M, Isaacson D and Newell J C, Electrical Impedance Tomography. *SIAM Review*, 41, 85-101, 1999.
- Chun K, Kim SJ, Cho ST, Noninvasive medical tools for evaluating voiding pattern in real life. *Int Neurourol J.* 21: S10–6, 2017.
- Coombes G M, Millard R J, The accuracy of portable ultrasound scanning in the measurement of residual urine volume. *J Urol.*; 152, 2083–5, 1994.
- David E R, Geoffrey E H & Ronald W, Learning representations by back-propagating errors. *Nature*, 323, 533–536, 1986.
- Dicuio M, Pomara G, Menchini Fabris F, *et al*, Measurements of urinary bladder volume: comparison of five ultrasound calculation methods in volunteers. *Arch Ital Urol Androl.* 77(1), 60-2, 2005.
- Chan E, Smith K, Mohamoud G, *et al*, Tri-Axial Ellipsoid Volume Calculation: A Method for Bladder Volume Estimation, *Journal of medical imaging and radiation sciences research informing practice*, 44 (1), 46–47, 2013.

- Franco I, New ideas in the cause of bladder dysfunction in children, *Current Opinion on Urology*. 21(4), 334-8, 2011.
- Gümbel D, Schneidler F, Frank M, Bockholdt B *et al*, Urinary bladder volume measured in whole-body CT scans is a useful marker for alcohol intoxication, *Alcohol*. 65:45-50, 2017.
- Haijun N, Songyan Y, Design of an Ultrasound Bladder Volume Measurement and Alarm System, *5<sup>th</sup> International Conference on Bioinformatics and Biomedical Engineering*, Wuhan, China 10-12 May, 2011.
- Han D K and Prosperetti A, Shape decomposition technique in electrical impedance tomography, *J. Comput. Phys.* 155, 75-95, 1999.
- Harris N D, Applications of electrical impedance tomography in respiratory medicine, PhD Thesis Univ. of Sheffield, 1991.
- Henderson R P, Webster J G, An impedance camera for spatially specific measurements of the thorax. *IEEE Transactions on Biomedical Engineering*. BME-25(3), 250-254, 1978.
- Hentzen C, Haddad R, Ismael S S, Peyronnet B, *et al*, Intermittent self-catheterization in older adults: predictors of success for technique learning. *Int Neurol J.* 22:65–71, 2018.
- Hyo Jeong Song, Mi Ah Han *et al*, Impact of Lower Urinary Tract Symptoms and Depression on Health-Related Quality of Life in Older Adults, *International Neurology Journal*. 16(3), 132–138, 2012.
- Isaacson D and Cheney M, Current problems in impedance imaging, In *Inverse problems in partial differential equations*, *SIAM Philadelphia*, chapter 9 pages 141-149, 1990.
- Jain H, Isaacson D, Edic P M and Newell J C, Electrical impedance tomography of complex conductivity distributions with noncircular boundary, *IEEE Trans. Biomed. Eng.* 44 1051-1060, 1997.
- Jianhuo W, Chunlin H, *et al*, Design and Evaluation of a New Bladder Volume Monitor, *Archives of Physical Medicine and Rehabilitation*, 90(11),1944-1947, 2009.

Jianwei L, Yang Y, Wang R, An Image Reconstruction Algorithm Based On RBF Neural Network for Electrical Capacitance Tomography, *Electromagnetic Field Problems and Applications (ICEF), Sixth International Conference*, 2012.

Kalbinder P, Duncan R *etc al* “Hardiness and Outcome of Self-catheterisation Training (HOST): protocol for an observational study exploring the effects of personality traits in women on ability to learn clean intermittent self-catheterisation, *BMJ journal*, 4(1), 2014.

Khambampati A K, Rashid A, Kim B S, Liu Dong, Kim S and Kim K Y, EM algorithm applied for estimating non-stationary region boundaries using electrical impedance tomography *J.Phys.: Conf. Ser.* 224 012044, 2010.

Kim C T, Linsenmeyer T A, Kim H, Yoon H, Bladder volume measurement with electrical impedance analysis in spinal cord-injured patients. *Am J Phys Med Rehabil.* 77(6), 498-502, 1998.

Kingma D P and Ba J, Adam: A method for stochastic optimization, *Proceedings of the 3rd International Conference on Learning Representations (ICLR)*, 2014.

Knight R A and R T Lipczynski, The use of EIT Techniques to measure interface pressure. *In Engineering in Medicine and Biology Society, International Conference of the IEEE.* 1990.

Kolehmainen V, Arridge S R, Lionheart W R B, Vauhkonen M and Kaipio J P, Recovery of region boundaries of piecewise constant coefficients of elliptic PDE from boundary data, *Inverse Problems.* 15 1375-1391, 1999.

Landau T P, Thiagarajan T R, Ledley RS. Cost containment in the concentrated care center—a study of nursing, bed and patient assignment policies. *Comput Biol Med.* 13:205–38, 1983.

Leippold T, Reitz A, Schurch B, Botulinum toxin as a new therapy option for voiding disorders: current state of the art, *European Urology.* 44(2):165-74, 2003.

Mann R, Dickin F J, Wang M, Dyakowski T, Williams R A and Edwards R B et al, Application of electrical resistance tomography to interrogate mixing processes at plant scale, *Chem. Eng. Sci.* 52 2087-97, 1997.

Moody J. and Darken C J, Fast learning in networks of locally tuned processing units, *Neural Computation*, 1, 281-294, 1989.

- Niestoruk L. *et al.* A concept for wearable long-term urinary bladder monitoring with ultrasound. Feasibility study. *EDERC Proc. 5th Eur. DSP Educ. Res. Conf.* 134–138 (2012).
- Nolwenn L, Andy A, Dominique G, Florence N, Electrical Impedance Tomography in geophysics, application of EIDORS, *Conf EIT, Bath, UK*, 4–6, 2011.
- Okamura K, Usami T *et al.*, Quality of Life: Assessment of Urination in Elderly Japanese Men and Women with Some Medical Problems Using International Prostate Symptom Score and King's Health Questionnaire, *European Urology*. 41(4):411-9, 2002.
- Osterman K S, Kerner T E, Williams D B, Hartov A, Poplack S P and Paulsen K D Multifrequency electrical impedance imaging: preliminary in vivo experience in breast, *Physiol. Meas.* 21 99–109, 2000.
- Phelan M W, Franks M, Somogyi G T, Yokoyama T, Fraser M O, Lavelle J P, Yoshimura N, Chancellor M B, Botulinum toxin urethral sphincter injection to restore bladder emptying in men and women with voiding dysfunction. *J Urol.* 165:1107–10, 2001.
- Phil kim, MATLAB Deep Learning: With Machine Learning, Neural Networks and Artificial Intelligence, *textbook*, 2017.
- Pinheiro P A T, Loh W W and Dickin F J, Smoothness-constrained inversion for two-dimensional electrical resistance tomography *Meas. Sci. Technol.* 8, 293-302, 1997.
- Plaskowski A, *Imaging Industrial Flows: Applications of Electrical Process Tomography*, Bristol, UK, Philadelphia: Institute of Physics Pub., 1995.
- Rashid A, Khambampati A K, Kim B S, Dong L, Kim S, and Kim K Y, A differential evolution based approach to estimate the shape and size of complex shaped anomalies using EIT measurements GDC/CA, *CCIS, Berlin: Springer*, 121, 206-15, 2010.
- Rashid A, Khambampati A K, Kim B S, Kim S, Kang M J and Kim K Y, An EKF based estimation scheme for sedimentation processes in vessels using EIT-type measurement data, *Flow Meas. Inst.* 21 521-30, 2010.

- Shida K, Yagami S. A non-invasive urination-desire sensing system based on four-electrodes impedance measurement method. In *IECON 32<sup>nd</sup> annual conference on IEEE industrial electronics*. New York, 2975–78, 2006.
- Somersalo E, Isaacson D and Cheney M, A linearized inverse boundary value problem for Maxwell equations, *J comput. Appl. Math.* 42 123-136, 1992
- Thomas Schlebusch, Steffen Leonhardt, Effect of electrode arrangements on bladder volume estimation by electrical impedance tomography, *Journal of Physics: Conference Series* 434, 012080, 2013.
- Vauhkonen M, Electrical impedance tomography and prior information, PhD Thesis, *University of Kuopio, Finland*, 1997.
- Vauhkonen M, Karjalainen P A and Kaipio J P, A Kalman filter approach applied to the tracking of fast organ boundaries Proc. *20th Annual Int. Conf. of the IEEE Engineering in Medicine and Biology Society* 20 1048, 1998.
- Warren J W, Catheter-associated urinary tract infections. *Infect Dis Clin N Am*, 11:609, 1997.
- Wen-Chien Liao and Fu-Shan Jaw, Noninvasive electrical impedance analysis to measure human urinary bladder volume, *J. Obstet. Gynaecol. Res.* 37, 8: 1071–1075, 2011.
- Widrow B and Hoff M E, Adaptive Switching Circuits, *Ire Wescon Convention Record*, 4:96-104, August 1960.
- Won Sik Jeong, Hong Yong Choi *et al*, Men with Severe Lower Urinary Tract Symptoms Are at Increased Risk of Depression, *International Neuourology Journal*. 19(4): 286–292, 2015.
- Yaning Li, Yinglin Peng, Xin Yang, Shipei Lu, et al Analysis of measurement electrode location in bladder urine monitoring using electrical impedance, *BioMed Eng OnLine* (2019) 18: 34.
- Zhang H W, *et al*, An Influence of the Noise on the Imaging Algorithm sin the Electrical Impedance Tomography. *Open J. Biophys*, 3, 2013.